
UNIVERSIDAD
DE GRANADA

# SEASONAL RIVER MOUTH HYDRODYNAMICS AND MORPHODYNAMICS DURING EXTREME-FLOOD CONDITIONS

Doctoral Thesis

Antonio Ruiz Reina

*Advisor*: Alejandro López Ruiz

Instituto Interuniversitario de Investigación del
Sistema Tierra en Andalucía (IISTA)

Programa de Doctorado de Dinámica de Flujos
Biogeoquímicos y sus Aplicaciones

February 2024

Editor: Universidad de Granada. Tesis Doctorales
Autor: Antonio Ruiz Reina
ISBN: 978-84-1195-287-3
URI: https://hdl.handle.net/10481/91110

El doctorando **Antonio Ruiz Reina** y el director de la tesis **Alejandro López Ruiz** garantizamos, al firmar esta tesis doctoral, que el trabajo ha sido realizado por el doctorando bajo la dirección del director de la tesis y hasta donde nuestro conocimiento alcanza, en la realización del trabajo, se han respetado los derechos de otros autores a ser citados, cuando se han utilizado sus resultados o publicaciones.

Granada, Febrero 2024

Director de la Tesis Doctorando

Fdo.: Alejandro López Ruiz Fdo.: Antonio Ruiz Reina

## Agradecimientos

Me apetece especialmente empezar por quienes, sin duda, han sido los pequeños motores de esta aventura: Vega, Lara y Emma. Sin saberlo, han sido una parte fundamental del trabajo de su padre con sus preguntas y curiosidad. Aunque aún me recriminan por qué tardo tanto en acabar "los deberes". Siguiendo con la rama familiar, he de citar también a mis hermanas, Blanca, Ale y Belén, acompañantes en la distancia. Y por supuesto a mis padres. A Blanca, por saber espolear al burro manchego desde hace muchos años. Y a Antonio, por compartir el interés por este trabajo y por su habilidad para deslizar palabras sensatas en momentos oportunos.

En este punto me gustaría centrar estos agradecimientos en el apoyo que he recibido desde el Programa de Doctorado y sus responsables. No solo se adaptaron a la singularidad de mi situación, sino que me han dado facilidades, recursos e incluso la oportunidad de compartir mis avances. Muy especialmente he de citar a Miguel, mi tutor, que durante estos años ha despejado muchas de las dudas y dificultades que han surgido.

No puedo olvidarme de mis compañeros de Departamento de la Universidad de Sevilla, siempre solícitos a cualquier petición o favor. Con especial cariño aquellos que tengo más cerca, Nicolás, Guille, Pepe; y mi apreciada Camelia, que además añade siempre una nota de cortesía y humor. Mención aparte merece Carmen, que resultó ser un descubrimiento en lo personal y por la estupenda labor académica que realiza.

Es de justicia también citar a mis actuales compañeros del SAIH del Guadalquivir. Porque, aunque ellos no lo saben, nuestro trabajo diario con su buen hacer y el ambiente familiar, ha sido el contexto ideal, motivador, para poder terminar este doctorado. Un lugar donde el tema de esta tesis está continuamente presente y me ha permitido aprender sobre otras muchas cuestiones.

Enumerar a los amigos de la carrera y de profesión que me han acompañado estos años sería un placer, pero también una lista interminable. Porque con sus inquietudes y sus preguntas también han contribuido a su manera, ayudándome a cuestionármelo todo y profundizar en lo que hacía. Algunos más de cerca, como mis queridos Raulillo o Manu. Otros un poco más lejos, como Fidel, Emilio, Jota, Raúl,.... Y algunas, como María, con consejos especialmente útiles sobre este mundo académico.

Llego al punto en que es una alegría detenerme y agradecer, con un cariño especial, la labor de mi Director de Tesis, Álex. Su guía ha sido impecable, sus formas exquisitas, sus aportaciones siempre valiosas y constructivas, todo englobado en una dirección de tesis que surgió casi por azar y en la que he resultado tener mucha suerte. Por estos motivos, y porque ha mostrado una comprensión y cercanía que valoro enormemente. Espero que esto solo sea el principio de muchos años de colaboración.

Y finalmente, mi agradecimiento más profundo y emotivo. Simplemente, hubiera sido imposible sin ti, Mila. El tiempo es finito, y tú me has proporcionado todo el que has podido para que yo pudiera finalizar este proyecto. No había mejor apoyo. Yo firmo este trabajo, pero le llamaremos “nuestra tesis”.

## Abstract

River mouths and deltas are areas of great environmental and socio-economic interest, containing some of the world's most valuable ecosystems and densely populated areas. This has led to the development of important industrial and agricultural areas, often requiring inland waterways along the waterways that feed these mouths. The processes of nutrient, salinity and sediment transport and mixing in these environments are very important for the biogeochemical evolution of many river and marine ecosystems, as well as for the formation of morphologies such as bars and deltas. The development of these morphologies often occurs through sediment deposition from the river channel, littoral drift and the interaction between the two. In addition, both river mouths and deltas are subject to extreme flooding caused by river discharge, storm surge or a combination of both. The management of these extreme events is becoming increasingly difficult due to changes in their frequency and intensity caused by climate change and increased urbanisation pressures. A better understanding of the dynamics of river estuaries is therefore essential for their management from both an environmental and socio-economic perspective.

In this context, the main objective of this dissertation is to analyse the hydrodynamics and morphodynamics of river mouths during extreme discharge events in order to characterise the role played by: (1) the geometry of the channel, outlet and beach profile; (2) the temporal variation of the river discharge conditions; and (3) the temporal variation of the sea level due to the tide. The analysis is carried out using a process-based numerical model (Delft3D) on idealised river mouths whose geometric and physical parameters are based on real river mouths where management problems have been identified during flood events. The results obtained represent an important advance in the knowledge of the hydromorphodynamics of river mouths and deltas and are directly applicable to coastal managers and policy makers involved in coastal flood management.

The analysis begins with a study to characterise the frontier of the zone of influence of marine agents upstream of the outlet, and how the characteristics of the channel and the tides determine the position of this frontier. The results show that this position is closely related to channel slope, channel roughness and tidal conditions. In particular, channel slope is the most important factor in determining the extent of marine influence, with bed roughness (i.e. vegetation, river conservation conditions, etc.) and discharge/tidal conditions being particularly relevant for low values of channel slope.

The next step is to characterise the hydrodynamics of outlets, and in particular the role of outlet geometry and beach profile, as well as non-stationary conditions of discharge and sea level in these hydrodynamics. Simulations for stationary conditions, where outlet geometry and beach profile are varied, show that the shape of the outlet determines the jet structure, with shallower and wider outlets having two velocity peaks at the sides of the jet instead of a single maximum in the centre. Furthermore, the hydrodynamics at the outlet are clearly dominated by friction for horizontal beach profiles, while for sloping profiles inertial and barotropic accelerations significantly increase their role in the vicinity of the outlet.

Regarding the effect of tidal and time-varying river discharges, for which hydrographs with a time scale similar to that of the tides are analysed, the results show that the variability of the jet structure during the tidal cycle is very important, limiting the applicability of the analyses performed for stationary conditions in tidal environments or with a variable hydrological regime.

In addition, the time lag between the peak of the hydrograph and the tidal conditions determines the geometry of the transverse velocity profile. At low tide, the velocity profile tends towards a profile with two lateral velocity peaks. Under high tide conditions, a velocity profile with a single maximum on the axis is observed. Therefore, this time lag can potentially lead to important changes in the morphodynamic evolution of outfalls during extreme discharge events. The changes observed in the jet structure as a function of the time lag between the peak of the hydrograph and the tidal level motivate the next step of the analysis carried out in this thesis, which addresses the role of this time lag in the development of nearshore bars at river mouths during extreme river discharge events. Results from hydro-morphodynamic simulations show that different values of the lag cause significant changes in (1) the time at which peak flows are reached at the outlet, (2) the period during which sediment is mobilised through the outlet, and (3) the maximum sediment transport rates during the events. These changes significantly modify the final characteristics of the bars that develop at the outlet, doubling their final extent and quadrupling the final bar volume for the same river discharge conditions and different lags, also varying their plan shape and the development of lateral bars.

Finally, the advances made above are applied and analysed to assess the flood hazard at river mouths, how this hazard changes depending on the characteristics of the discharge and how the mouth evolves morphodynamically during the extreme flood event. The main factor dominating the delineation of hazard zones is the peak flow. For low flows, the influence of the tide increases and the hazard conditions are higher during periods of high tide. For intermediate flows, there is a combined influence of river discharge and tide, so that the most hazardous conditions occur when peak flow and low tide converge. For high flows, the hazard zones are determined by the discharge hydrograph and the influence of the tide is significantly reduced, with the hazard condition in the mouth area only increasing during the coincidence of low tide and peak flow. The presence of an river mouth bar modifies the classification of the hazard zones around the outlet and slightly reduces the maximum category, especially for the coincidence of peak flow and low tide.

## Resumen

Las desembocaduras de los ríos y los deltas son zonas de gran interés ecológico y socioeconómico, que contienen algunos de los ecosistemas más valiosos del mundo y zonas densamente pobladas. Esto ha propiciado el desarrollo de importantes zonas industriales y agrícolas, que a menudo requieren vías navegables interiores a lo largo de los cursos fluviales que alimentan estas desembocaduras. Los procesos de transporte y mezcla de nutrientes, salinidad y sedimentos en estos entornos son muy importantes para la evolución biogeoquímica de muchos ecosistemas fluviales y marinos, así como para la formación de morfologías como barras y deltas. El desarrollo de estas morfologías suele producirse mediante la deposición del sedimento procedente del cauce fluvial, de la deriva litoral y la interacción entre ellos. Además, tanto las desembocaduras de los ríos como los deltas están sujetos a inundaciones extremas causadas por la descarga del río, marea meteorológica o una combinación de ambas. La gestión de estos fenómenos extremos es cada vez más difícil debido a los cambios en su frecuencia e intensidad provocados por el cambio climático, así como por el incremento de la presión urbanística. Mejorar el conocimiento de la dinámica de las desembocaduras de los ríos es, por tanto, fundamental para su gestión desde una perspectiva tanto medioambiental como socioeconómica.

En este contexto, el objetivo principal de esta tesis es analizar la hidrodinámica y morfodinámica de las desembocaduras de los ríos durante eventos extremos de descarga fluvial con el fin de caracterizar el papel desempeñado por: (1) la geometría del canal, la desembocadura y del perfil de playa; (2) la variación temporal de las condiciones de descarga del río; y (3) la variación temporal del nivel del mar debido al efecto marea. El análisis se lleva a cabo utilizando un modelo numérico basado en procesos (Delft3D) sobre desembocaduras idealizadas cuyos parámetros geométricos y físicos se basan en desembocaduras reales donde se han identificado problemas de gestión durante eventos de inundación. Los resultados obtenidos suponen un importante avance en el conocimiento de la hidromorfodinámica de desembocaduras y deltas y son directamente aplicables a los gestores costeros y responsables políticos implicados en la gestión de inundaciones costeras.

El análisis comienza con un estudio para caracterizar el límite de la zona de influencia de los agentes marinos aguas arriba de desembocaduras, y cómo las características del cauce y de la marea astronómica condicionan la posición de este límite. Los resultados muestran que esta posición está estrechamente relacionada con la pendiente del río, la rugosidad del río y las condiciones de la marea. En particular, la pendiente del río es el factor más importante para determinar el alcance de la influencia marina, siendo la rugosidad del lecho (es decir, la vegetación, las condiciones de conservación del río, etc.) y las condiciones de descarga/marea especialmente relevantes para valores bajos de la pendiente del río.

El siguiente paso es la caracterización de la hidrodinámica de desembocaduras, y en particular del papel de la geometría de la desembocadura y el perfil de playa, así como de condiciones no estacionarias de descarga y nivel del mar ven dicha hidrodinámica. Las simulaciones para condiciones estacionarias en las que se varía la geometría de de la desembocadura y del perfil de playa muestran que la forma de la salida determina la estructura del chorro, ya que aquellas menos profundas y más anchas presentan dos picos de velocidad a los lados del chorro en lugar de un único máximo en el centro. Además, la hidrodinámica en la desembocadura está claramente dominada por la fricción para perfiles de playa horizontales, mientras que para

perfiles inclinados las aceleraciones inerciales y barotrópicas aumentan significativamente su papel en las proximidades de la desembocadura.

En cuanto al efecto de la marea y de las descargas fluviales variables en el tiempo, para las que se analizan hidrogramas con una escala temporal similar a la de la marea astrónomica, los resultados muestran que la variabilidad de la estructura del chorro durante el ciclo de marea es muy importante, limitando la aplicabilidad de los análisis realizados para condiciones estacionarias en entornos mareales o con un régimen hidrológico variable. Además, el desfase temporal entre el pico del hidrograma y las condiciones de marea determina la geometría del perfil de velocidad transversal. En condiciones de marea baja, el perfil de velocidad tiende a un perfil con dos picos laterales de velocidad. En condiciones de marea alta, se observa un perfil de velocidad con un único máximo en el eje. Por tanto, este desfase puede, potencialmente, provocar importantes cambios en la evolución morfodinámica de desembocaduras durante eventos extremos de descarga.

Los cambios observados en la estructura del chorro en función del desfase entre el pico del hidrograma y el nivel de marea motivan el siguiente paso del análisis realizado en esta Tesis Doctoral, que aborda el papel de este desfase en el desarrollo de barras cercanas a la costa en las desembocaduras de los ríos durante eventos extremos de descarga fluvial. Los resultados obtenidos mediante simulaciones hidro-morfodinámicas muestran que diferentes valores del desfase provocan cambios significativos en (1) el instante en el que se alcanzan las corrientes máximas en la salida, (2) el periodo durante el cual el sedimento se moviliza a través de la salida, y (3) las tasas máximas de transporte de sedimentos durante los eventos. Estos cambios modifican significativamente las características finales de las barras que se desarrollan en la desembocadura, duplicando su extensión final y cuadruplicando el volumen final de la barra para las mismas condiciones de descarga del río y diferente desfase, variando también su forma en planta y el desarrollo de barras laterales.

Por último, los avances obtenidos anteriormente son aplicados y analizados al cálculo de la peligrosidad de inundación en desembocaduras, analizando cómo cambia dicha peligrosidad en función de las características de la descarga y de cómo va evolucionando morfodinámicamente la desembocadura durante el evento extremo de inundación. El principal factor que domina la delimitación de las zonas de peligro es el caudal punta. Para caudales bajos, aumenta la influencia de la marea y las condiciones de peligro son mayores durante los periodos de marea alta. Para caudales intermedios, existe una influencia combinada de la descarga del río y la marea, de modo que las condiciones más peligrosas se producen cuando convergen el caudal punta y la marea baja. En los casos de caudales altos, las zonas de peligro vienen determinadas por el hidrograma del río y la influencia de la marea se reduce significativamente, limitándose a aumentar la condición de peligro en la zona de la desembocadura durante las coincidencias de la marea baja y el caudal punta. La presencia de una barra de desembocadura modifica la clasificación de las zonas de peligro alrededor de la desembocadura y reduce ligeramente la categoría máxima, especialmente para los casos con coincidencia de caudal punta y marea baja.

# CONTENTS

# List of Figures

# List of Tables

CHAPTER 1

# INTRODUCTION

## 1.1 River mouth dynamics

Coastal zones are habitats of high socio-economic value, characterised by increasing population densities and hosting important economic activities (Del-Rosal-Salido et al., 2019). More than 60% of the world's population lives in contiguous and hydrologically connected coastal zones below 10 m above mean sea level, which can be affected by coastal and/or riverine flooding (Lichter et al., 2011). Among these coastal areas, transitional environments exhibit a high and complex spatio-temporal variability of their hydrodynamics due to the superposition and interaction of multiple processes induced by concomitant (compatible and simultaneous) maritime, fluvial and atmospheric agents (Lamb et al., 2012; Leonardi, Kolker, and Fagherazzi, 2015; Del-Rosal-Salido et al., 2019). Consequently, the management of these environments requires a good understanding of both normal and extreme conditions in order to properly assess the associated flood risks.

Among these transitional environments, river mouths and deltas stand out as areas of great ecological and socio-economic interest, containing some of the world's most valuable ecosystems and densely populated areas (Lamb et al., 2012). This has led to the development of important industrial and agricultural areas, which often require inland waterways along the river courses that feed these mouths. The processes of transport and mixing of nutrients, salinity and sediments in these environments are very important for the biogeochemical evolution of many riverine and marine ecosystems, as well as for the formation of morphologies such as bars and deltas. The development of these features generally follows sediment deposition, which can occur through natural levee growth and channel elongation, or through deposition and vertical aggradation of estuarine bars (Fagherazzi et al., 2015). In addition, both river mouths and deltas are subject to extreme flooding events caused by river discharge, storm surge or a combination of both. The management of these extreme events is becoming increasingly challenging due to changes in their frequency and intensity caused by climate change (Fernandino, Elliff, and Silva, 2018). Improving knowledge of the dynamics of river mouths is therefore fundamental to their fate, both from an environmental and socio-economic perspective.

## 1.2 Extreme events

One of the main problems faced by river mouths and deltas in recent years has been flooding caused by the combined effect of river discharge, tides and storm surge. Numerous Spanish examples over the last decade have highlighted the increased risk in these areas of great social, environmental and economic value, including flooding at the river mouths of the rivers Antas (2012), Andarax (2015), Guadalfeo (2018) and all the mouths of the Andalusian Atlantic coast in the winter of 2018 following the passage of hurricanes Emma and Hugo. These floods in areas close to mouths will become more frequent and important in the coming years, not only due to the occupation of adjacent areas, but also because climate change is raising sea levels and modifying the frequency and magnitude of medium/high return period flood events (Del-Rosal-Salido et al., 2019; Del-Rosal-Salido et al., 2021).

These events are already a major management problem, causing severe economic, social and environmental damage. One of the most recent examples is the passage of the storm "Gloria" along the Spanish Mediterranean coast in January 2020 (Amores et al., 2020), whose impact, according to a first estimate by the Consorcio de Compensación de Seguros, is estimated at 71 million euros, with a number of more than 10,000 claims, among which those caused by flooding in the Ebro Delta are particularly relevant. In addition, there is a greater sensitivity to damage caused by natural disasters, among which floods occupy a predominant place due to their increased frequency and intensity. This problem is being tackled by the various administrations through various forecasting and management programmes.

Furthermore, in recent years, the identification of critical areas specially threatened by the impact of extreme events in form of coastal and fluvial flooding is becoming extremely urgent for managers as a key element of risk assessments. This is intensified by (1) the increase of human pressure on areas close to river mouths; (2) the sea level rise, which is expected to aggravate storm surge-related risks to coastal and riverine communities; and (3) the increase in the frequency and extent of storm surges and river discharges due to the ongoing reduction of return periods.

## 1.3 The management perspective. Motivation

The occurrence of flood extreme events on areas with the complexity of river mouths and delta is a major challenge for managers. The European Union, its Floods Directive stipulates that Member States must design and implement risk-based flood management practices aimed at minimising the negative consequences of these events. In the case of Andalusia, the draft ”Ley de Medidas para Combatir el Cambio Climático”, promoted by the Andalusian regional government and awaiting approval, aims to provide the regional administration with an instrument for preventing and correcting the adverse effects of this global phenomenon and its application to the plan for the prevention of floods and flooding in Andalusian urban watercourses. However, these prevention plans do not yet have a unified and rigorous methodology for assessing the risks associated with flooding and the effects of climate change, because the current state of knowledge has limitations for quantifying and assessing the risks derived from flooding in a rigorous manner.

Both the managers experience and the literature review suggests that the interactions between fluvial discharge and marine agents are very complex, although they are crucial for the

management of river mouths and deltas. Furthermore, despite all the recent advances described in the following chapters, there are still important aspects to be analysed in order to describe the hydrodynamics and morphodynamics of these dynamic environments both a mean and extreme conditions. Filling this gap in the main motivation of this Thesis. In particular, this Thesis is focused on the hydrodynamics resulting from the interaction between river discharge and tidal variations in sea level in more realistic environments than those analysed in the literature, which have mainly focused on very simplistic scenarios in which the effect of the tide has been neglected or excessively simple geometries have been considered. The results of this work are expected to represent an important step forward in the management of the coast in general, and the flooding of areas adjacent to river mouths in particular, contributing to the development and application of new legislation that responds to these challenges.

## 1.4 Objectives

### Main objective

The main objective of this thesis is to analyse the hydrodynamics and morphodynamics of river mouths during extreme river discharge events in order to characterise the role played by: (1) the geometry of the channel, outlet and nearshore; (2) the temporal variation of the river discharge conditions; and (3) the temporal variation of the sea level due to the tidal effect. The analysis is carried out using a process-based numerical model (Delft3D) on idealised outlets whose geometric and physical parameters are based on those of the Andalusian Mediterranean coast, where management problems have been identified during flood events. The results obtained represent an important step forward in the knowledge of the hydro-morphodynamics of river mouths and deltas and are directly applicable to coastal managers and policy makers involved in coastal flood management.

### Specific objetives

In order to achieve the general objective, the following specific objectives are defined:

1. To precisely define the area in which both fluvial and marine agents determine the hydrodynamics of outlets, and therefore the area in which it is necessary to analyse their joint effect for flood management.
2. To study, by means of numerical modelling, how the outlet and nearshore geometries may determine the hydrodynamics of the river mouths and, in particular, the jet structure.
3. Extend the previous analysis to analyse the role of extreme river discharge events and the tide in the hydrodynamics, especially for basins where the discharge hydrograph has a time scale of the same order as the tidal period.
4. Analyse the morphodynamic evolution of river mouths during extreme events such as those described in the previous section, for which the time lag between the peak of the hydrograph and the tidal level can potentially play a very important role.
5. Following on from the previous points, which present a more theoretical approach, transfer the knowledge acquired to assess the impact of identified key parameters on flood hazard mapping and associated categories.

## 1.5 Outline of the Thesis

In addition to the introduction (Chapter 1) and the conclusions and future work (Chapter 7), this thesis is divided into 5 chapters, each corresponding to one of the specific objectives listed above.

In Chapter 2, the interplay between river discharge and astronomical tides is analysed in order to identify the marine-fluvial boundary during extreme river floods at river mouths. This boundary is evaluated in terms of distance from the river mouth using the results of the process-based numerical model.

Chapter 3 is devoted to the analysis of the jet theory and its limitations when considering realistic geometries. The analysis is carried out using a numerical model implemented in different idealised river mouths where the main geometric characteristics are varied.

Chapter 4 extends the analysis of Chapter 3 for time-varying conditions of river discharge and water level. The focus is on how these transient conditions determine the shape of the jet and the potential morphodynamic implications.

Chapter 5 analyses the morphodynamics of short-term extreme discharge events, in particular the intratidal effects of the phase difference between peak discharge and tidal levels on the development and final characteristics of river mouth bars formed after extreme river floods.

Finally, Chapter 6 presents a flood hazard analysis based on the hydrodynamic and morphodynamic results obtained in the previous chapters. The hazard is quantified in terms of a combination of water depths and velocities and a simple flood hazard classification is presented.

## 1.6 Publications derived from this Thesis

**Refereed Journal Papers**

- **Ruiz-Reina, A.**, and López-Ruiz, A. (2024). River mouth hydrodynamics: the role of the outlet geometry and transient tidal and river discharge conditions on the jet structure. *Journal of Geophysical Research: Oceans. To be submitted*
- **Ruiz-Reina, A.**, and López-Ruiz, A. (2021). Short-term river mouth bar development during extreme river discharge events: The role of the phase difference between the peak discharge and the tidal level. *Coastal Engineering*, 170(August), 103982.
- **Ruiz-Reina, A.**, Zarzuelo, C., López-Herrera, J. M., and López-Ruiz, A. (2020). The Marine-fluvial Frontier at River Mouths during Extreme Events: A Hydrodynamic Approach. *Journal of Coastal Research*, 95(sp1), 1525 – 1530.

**International Peer-Reviewed Conferences**

- **Ruiz-Reina, A.**, Zarzuelo, C., and López-Ruiz, A. (2022). Flood hazard mapping in river mouths: the effect of river bar formation and the phase lag between tides and river discharge. In: River Flow (Eleventh International Conference on Fluvial Hydraulics) 2022. Kingston and Ottawa (Canada).

- **Ruiz-Reina, A.**, Zarzuelo, C., López-Herrera, J. M., and López-Ruiz, A. (2020). The Marine-fluvial Frontier at River Mouths during Extreme Events: A Hydrodynamic Approach. In: International Coastal Symposium (ICS) 2020. Sevilla (Spain).

**National Peer-Reviewed Conferences**

- **Ruiz-Reina, A.**, Zarzuelo, C., López-Herrera, J. M., and López-Ruiz, A. (2018). Estudio de la influencia marina en desembocaduras de ríos andaluces durante episodios de inundaciones para la determinación de áreas de peligrosidad. In: X Simposio del Agua en Andalucía, 2018. Huelva (Spain).

CHAPTER 2

# THE MARINE-FLUVIAL FRONTIER AT RIVER MOUTHS DURING EXTREME EVENTS: A HYDRODYNAMIC APPROACH

This chapter analyses the interplay between river discharge and astronomical tides to identify the marine-fluvial boundary during extreme river floods at river mouths. The main variables controlling the position of this boundary are identified and their influence is quantified in terms of the distance upstream of the river mouth for which tides modify water levels. The analysis is carried out using numerical modelling on synthetic scenarios, thus broadening the applicability of the results. The results show that the location of the boundary is closely related to both the gradient of the river and the relationship between water depths along the river and at the mouth. These water depths are related to river roughness and tidal conditions respectively. This detailed analysis of the location of the marine-fluvial boundary contributes to (1) a deeper knowledge of the dynamics of river mouths, which is used in the following chapters to characterise the hydro-morphodynamics of extreme river discharge events at river mouths; and (2) the application of risk assessment procedures based on the determination of hazard areas classified by threshold values of water depth and velocity, as shown in Chapter 6. The main results of this chapter have been published in (Ruiz-Reina et al., 2020).

## 2.1 Introduction

This chapter aims to analyse the interaction between fluvial and maritime processes and the location of the marine-fluvial frontier during extreme events at river mouths using a hydrodynamic approach. In particular, the combined effects of high river discharges and astronomical tides within a complete tidal cycle is studied, being this frontier (i.e., tidal intrusion) the result of the dynamic balance of marine and fluvial forcing agents. In this work, the frontier is characterized through water elevation of the flow along the lower part of a river in a stretch of variable extent upstream of the river mouth.

In the last few years, the importance of the interaction between fluvial and marine processes was addressed by many researchers. Herdman, Erikson, and Barnard (2018) and Lee et al. (2019)

used numerical modelling to analyze the interactions between tides, river discharge and storm surge at estuaries in USA and Korea, respectively. Both works highlight that these interactions are not simple. This issue was analysed with more detail by Del-Rosal-Salido et al. (2019), who developed an integrated method for characterizing the spatiotemporal variability and distribution function of extreme total water level events in a transitional coastal area in Southern Spain. Their results highlight the non-linearities of the interactions between fluvial and marine processes.

Despite these recent works on river mouth hydrodynamics and the upstream propagation of tides and surges, the influence of the stream slope, stream roughness, tidal range and timing of the arrival of the peak of the storm hydrograph to the coastal region respect the tidal level on the position of the marine-fluvial frontier has not been described in detail.

The main objective of this chapter is to analyse the position of the marine-fluvial frontier or tidal intrusion for different stream characteristics and tidal conditions. After the analysis of the results, the main variables controlling the position of this frontier are obtained, as well as a simple method to calculate the extension of the marine influence during river flooding for several combinations of river and tidal characteristics.

## 2.2 River mouths database

Numerical simulations performed with a process-based model (Delft3D) on idealized physical scenarios will be used as the main tool throughout this Doctoral Thesis. The use of this type of scenarios has the following advantages:

- The results are more easily extrapolated to other study areas with similar characteristics, either through the use of dimensional or dimensionless variables.
- The isolated effect of geometric features such as channel slope or outlet dimensions, as well as forcing agents such as river discharge or astronomical tide, can be more easily characterized.
- Local effects of specific geometric features, such as the presence of shoals or bars, which can make the analysis of the results more complex, are not taken into account.

However, the use of idealised scenarios poses a problem mainly related to the ability of the results to be representative of situations observed in nature. In order to ensure the representativeness of the results, the numerically modelled physical scenarios have been defined on the basis of the average characteristics and geometry of a database obtained from the analysis of 16 ephemeral outlets located on the Mediterranean coast of Andalusia. The database, available in Ruiz-Reina (2021), contains geometric, hydrological and meteorological data that will be used to define not only the geometric characteristics of the idealised scenarios, but also the main forcing agents. The choice of this type of river mouth, in which the river discharge has a high temporal variability and whose extreme events are related to the passage of DANAs, is justified by the identification of management problems derived from episodes of river and coastal flooding in recent decades. The main characteristic of this type of basin is that it has a relatively limited surface area, which determines the duration of the discharge pulses, which in most cases have

a duration similar to that of the astronomical tides. As will be seen in the following chapters, the fact that the fluvial discharge episodes and the astronomical tide have similar characteristic periods means that the time lag between them emerges as a new variable to be analysed, despite the fact that there has been little previous work analysing its importance.

## 2.3 Regional setting

The numerical simulations were performed on a synthetic study site for which different hydrodynamic conditions and stream bed slopes were tested. Based on the analysis of the river mouths database in Ruiz-Reina (2021), the domain is formed by a straight 2500 m long stream with constant slope flowing into the coastal platform. The shoreline is also straight and orthogonal to the stream longitudinal axis, and the nearshore was simplified with parabolic equilibrium beach profiles (Dean and Dalrymple, 2004) extending up to 30 m depth (5000 m offshore). The alongshore width of the platform is 5000 m and with the stream axis in its centre.

The analysis of the database reveals that the morphology of the last reach of these streams has braided patterns with low sinuosity and high width/depth ratio. The average depth does not exceed 3.0 m in most of them, which leads to a stream width of 150 m. Observed stream slopes are limited to values in an interval between 0.2 and 0.7%. The stream geometry was defined to limit the overflowing at the riverbanks to fairly compare the water elevation of the studied cases regardless the topography of the area. Considering the basin areas and the stream geometry adopted, a range of river discharges between 100 $m^3/s$ and 1,000 $m^3/s$ is adopted, corresponding typically to approximately 10 and 50-year return period discharges in the area, respectively.

Tides in the area are semidiurnal and oscillate between microtidal and mesotidal conditions, with tidal ranges between 0.5 and 2 m. Hence, the selected amplitude of the semidiurnal tidal waves tested were 0.5 and 1 m. In order to isolate the role of astronomical tides on tidal intrusion and the river mouth hydrodynamics, the effects of wind waves were neglected, as well as those due to storm surges triggered by wind and atmospheric pressure gradients.

For the bottom roughness, a unique value of the Manning's roughness coefficient was defined in the nearshore area ($n = 0.020$). However, different values were adopted along the stream ranging between $n = 0.020$ and $n = 0.070$. These extreme values are representative of clean and vegetated streams, respectively.

According to the parameters defined above, which are based on the analysis of the regional dataset, 72 scenarios (simulations) were modelled (see 2.3).

## 2.4 Numerical model

### Model description

The numerical model implemented to solve the hydrodynamics of the jet is Delft3D (Lesser et al., 2004), which is widely used to analyse the hydrodynamics of river mouths (Edmonds and Slingerland, 2007; Nardin and Fagherazzi, 2012; Nardin et al., 2013; Nienhuis et al., 2016; Boudet, Sabatier, and Radakovitch, 2017; Lageweg and Feldman, 2018; Gao et al., 2019). This model is capable of solving transient flows using the shallow water equations. In this case,

| Id | Tide amplitude (m) | Stream slope (%) | Stream roughness (n) | Discharge ($m^3/s$) |
|---|---|---|---|---|
| 111-a/b/c | 1.0 | 0.20 | 0.020 | 250/500/1000 |
| 112-a/b/c | 1.0 | 0.20 | 0.040 | 250/500/1000 |
| 113-a/b/c | 1.0 | 0.20 | 0.070 | 250/500/1000 |
| 121-a/b/c | 1.0 | 0.70 | 0.020 | 250/500/1000 |
| 122-a/b/c | 1.0 | 0.70 | 0.040 | 250/500/1000 |
| 123-a/b/c | 1.0 | 0.70 | 0.070 | 250/500/1000 |
| 211-a/b/c | 0.5 | 0.20 | 0.020 | 250/500/1000 |
| 212-a/b/c | 0.5 | 0.20 | 0.040 | 250/500/1000 |
| 213-a/b/c | 0.5 | 0.20 | 0.070 | 250/500/1000 |
| 221-a/b/c | 0.5 | 0.70 | 0.020 | 250/500/1000 |
| 222-a/b/c | 0.5 | 0.70 | 0.040 | 250/500/1000 |
| 223-a/b/c | 0.5 | 0.70 | 0.070 | 250/500/1000 |
| 411-a/b/c | 1.0 | 0.20 | 0.020 | 100/200/300 |
| 412-a/b/c | 1.0 | 0.20 | 0.040 | 100/200/300 |
| 413-a/b/c | 1.0 | 0.20 | 0.070 | 100/200/300 |
| 421-a/b/c | 1.0 | 0.70 | 0.020 | 100/200/300 |
| 422-a/b/c | 1.0 | 0.70 | 0.040 | 100/200/300 |
| 423-a/b/c | 1.0 | 0.70 | 0.070 | 100/200/300 |
| 531-a/b/c | 1.0 | 0.40 | 0.020 | 100/200/300 |
| 532-a/b/c | 1.0 | 0.40 | 0.040 | 100/200/300 |
| 533-a/b/c | 1.0 | 0.40 | 0.070 | 100/200/300 |
| 541-a/b/c | 1.0 | 0.60 | 0.020 | 100/200/300 |
| 542-a/b/c | 1.0 | 0.60 | 0.040 | 100/200/300 |
| 543-a/b/c | 1.0 | 0.60 | 0.070 | 100/200/300 |

Table 2.3.1: Numerical simulations defined

buoyancy, ocean waves, Coriolis and wind effects are neglected using a depth-averaged version of the model in agreement with previous theoretical, experimental and numerical work (Lamb et al., 2012; Jiménez-Robles, Ortega-Sánchez, and Losada, 2016).

The model uses a finite difference scheme to solve the unsteady shallow water equations for unsteady, incompressible, turbulent flow. For depth-averaged simulations such as those performed in this work, the continuity and horizontal momentum equations are (Lesser et al., 2004):

$$\frac{\partial \eta}{\partial t} + \frac{\partial hu}{\partial x} + \frac{\partial hv}{\partial y} = S \tag{2.1}$$

$$\frac{\partial u}{\partial t} + u\frac{\partial u}{\partial x} + v\frac{\partial u}{\partial y} = -g\frac{\partial \eta}{\partial x} + M_x + g\frac{u\sqrt{u^2+v^2}}{C_{z,u}^2 h} + \epsilon_H\left(\frac{\partial^2 u}{\partial x^2} + \frac{\partial^2 u}{\partial y^2}\right) \tag{2.2}$$

$$\frac{\partial v}{\partial t} + u\frac{\partial v}{\partial x} + v\frac{\partial v}{\partial y} = -g\frac{\partial \eta}{\partial y} + M_y + g\frac{v\sqrt{u^2+v^2}}{C_{z,v}^2 h} + \epsilon_H\left(\frac{\partial^2 v}{\partial x^2} + \frac{\partial^2 v}{\partial y^2}\right) \tag{2.3}$$

where $\eta$ is the water level with respect to MSL, $t$ is time, $h$ is water depth, $u$ and $v$ are the flow velocities in the $x$ and $y$ directions, respectively, $S$ represents source/sink of water, and $g$ reads for gravity acceleration. $C_{f,u}$ and $C_{f,y}$ represent the Chézy roughness coefficients in the $x$ and $y$ directions, respectively, and are related with the Manning coefficient $n$ using $C_f = h^{1/6}/n$. $M_x$ and $M_y$ represent the external sources or sink of momentum, whereas the last term in equations 2.2 and 2.3 represents the horizontal Reynold's stresses, in which $\epsilon_H$ is the horizontal eddy viscosity defined by the user. The latter is computed using the Horizontal Large Eddy Simulations (HLES) technique. This closure model includes contributions from horizontal turbulent motions and forces that are not resolved on the original grid by adding a subgrid scale (SGS) horizontal eddy viscosity ($\epsilon_{H,SGS}$) to a constant or space-varying, user-defined background value ($\epsilon_H^{back}$):

$$\epsilon_H = \epsilon_{H,SGS} + \epsilon_H^{back} \tag{2.4}$$

Bed shear stresses are used as seabed boundary conditions for the momentum equations:

$$\vec{\tau}_b = \frac{\rho_w g \vec{U}|\vec{U}|}{C_f^2} \tag{2.5}$$

where $\rho_w$ is the water density, $g$ is the gravity acceleration, $\vec{U}$ is the flow depth-averaged velocity and $C_f$ is the Chézy coefficient, that can be determined also as:

$$C_f = \frac{h^{1/6}}{n} \tag{2.6}$$

where $n$ is the Manning coefficient.

### Model setup

In this case, the model domain was built with a rectangular grid with four open boundaries (Figure 2.4.1): (1) the offshore limit of the coastal platform located 5,000 m away from the river mouth, (2-3) two cross-shore boundaries 2,500 m far from the longitudinal axis of the stream, and (4) the upstream limit of the domain. The mesh elements are rectangular with variable size and maximum resolution of 5x5 m2 at the centre of the domain where the river mouth is located, and along the stream itself. To test the influence of the grid discretization on the results, a sensitivity analysis was performed using different grid sizes with maximum resolutions ranging from 5x5 to 25x25 m2. Although small differences in the detail of model outcomes were detected, the general trend followed by the hydrodynamic results did not show any deviation from a qualitative point of view for the different grid size tested, assuring the accuracy of the model runs. The choice of the discretization used for the scenarios in Table 1 was based on the level of detail necessary to analyse the results.

To meet stability and accuracy requirements of the numerical scheme, the smallest cell size of the grid determined a time step of 0.025 min, which was adopted to comply with the

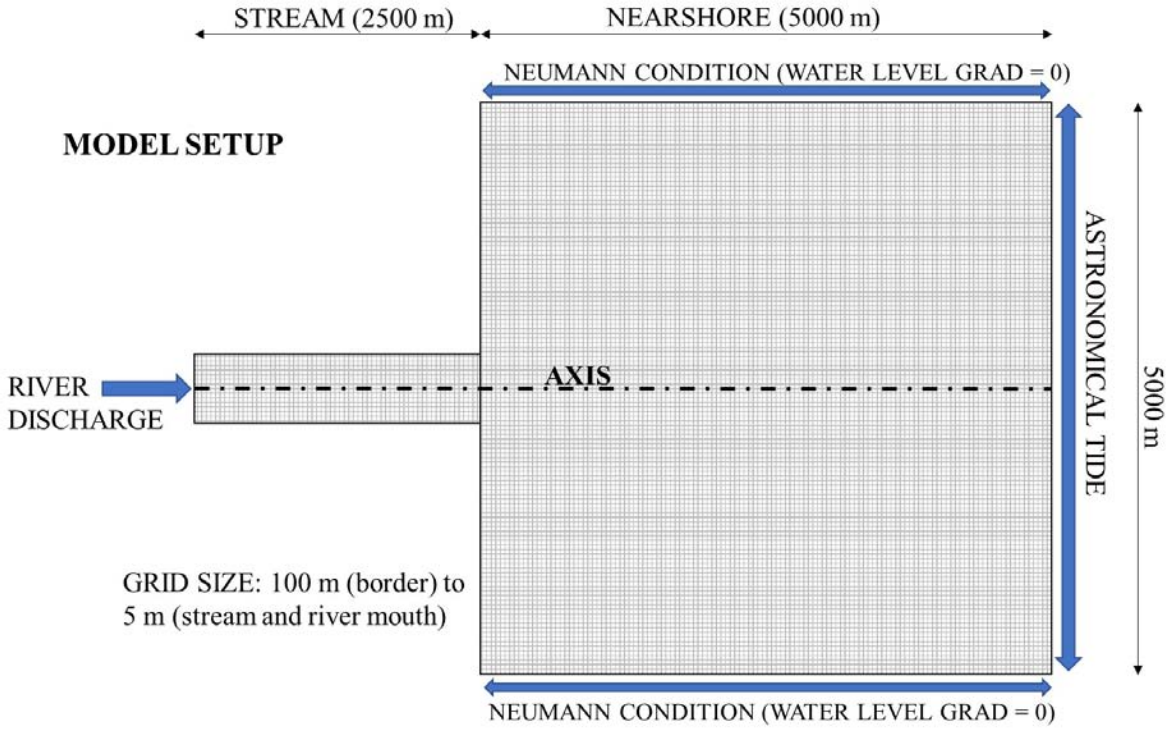


Figure 2.4.1: Numerical model setup. Neumann BC are defined for the water level gradients, not the water levels itself.

Courant-Frederichs-Levy condition (Lesser et al., 2004). The first 24 hours of each experiment were defined as spin-up interval in which fluvial discharge increases from rest conditions to the value defined for the simulation. After this interval, a constant discharge was imposed at the upstream boundary of the river during a tidal cycle, assuming steady conditions during this period for the fluvial discharge. This is used to analyse the effect of the timing of the arrival of the peak of the storm hydrograph respect to the tidal conditions. At the offshore grid limit, the sea level was prescribed as boundary condition using a semidiurnal tidal harmonic during the complete simulation. For the cross-shore boundaries, a Neumann-type boundary condition for water level was defined, prescribing null alongshore gradients for these levels to avoid numerical instabilities and spurious longshore currents.

## 2.5 Characterization of the marine-fluvial frontier

The results of the simulations in table 4.2 were analysed in terms of water levels along the longitudinal river axis during a complete tidal cycle. The framework of the analysis is presented in Figure (2.5.1), showing the main parameters: 1) the normal depth along the axis ($y_n$), corresponding to the uniform flow (UF) conditions of the river flow, 2) the outlet depth ($y_0$), defined as the difference between the instantaneous water level at the coastal platform due to astronomical tide and the bed level at the outlet, 3) the tidal intrusion ($D_0$), defined as the along-axis extent where a gradually varied flow (GVF) develops. It is measured from the river outlet up to the position where the tides modify the UF. To numerically determine $D_0$, a tolerance of 10 cm in

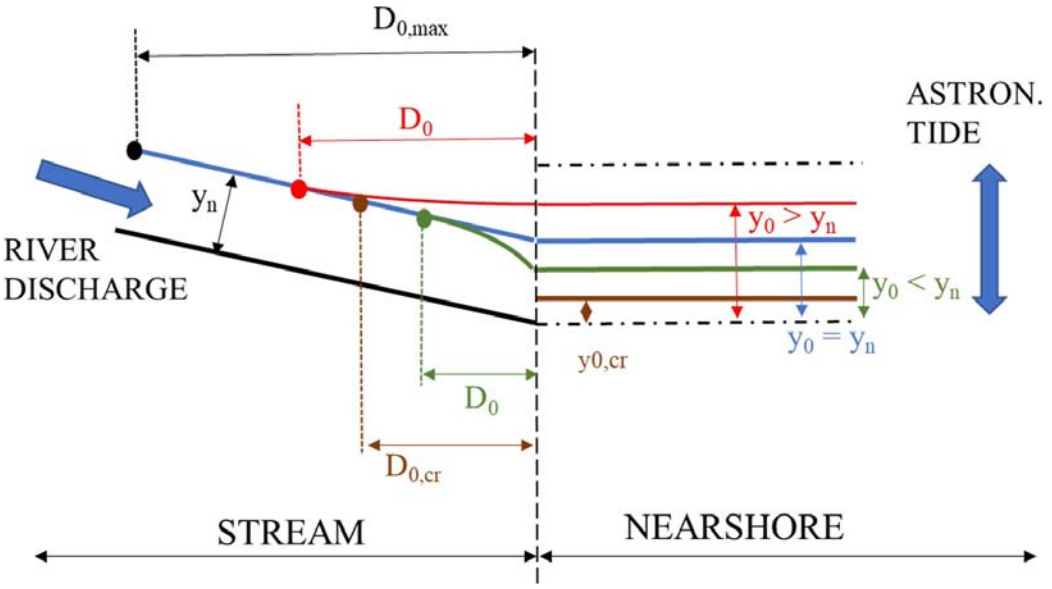


Figure 2.5.1: Longitudinal profile along the axis and the nearshore. The main water depth combinations during a tidal cycle are shown in colours.

water levels was considered, in agreement to the grid size and averaged bed slope employed. Figure (2.5.1) also shows the two main situations of the water levels along the axis for different values of $y_0$ (tidal phase):

- Those cases for instantaneous $y_0$ higher than the normal depth ($y_0$) along the stream are depicted in red lines. The water depth increases as it approaches the mouth. Extreme value for $D_0$ in this situation is denoted by $D_{0,max}$, corresponding to the highest tide.
- For $y_0 < y_n$, the water depth decreases along the axis (green line). Extreme value for $D_0$ in this situation corresponds to a critical flow conditions at the outlet (brown line).

Each $D_0$ value is located within this range of extreme values, depending on the relation between $y_0$ and $y_n$.

To analyse how the tidal intrusion $D_0$ varies during the tidal cycle as $y_0$ oscillates over the mean sea level, water levels and along-axis distances were non-dimensionalized with $y_n$ as $y_0^* = y_0/y_n$ and $D_0^* = D_0/y_n$. Figure (2.5.2) depicts the theoretical behaviour of the water profile along the river during a tidal cycle; in the plot, $y_0^* = 1$ splits the general curve that $D_0^*$ describes during a complete tidal cycle in three main regions:

- Region 1 ($y_0^* > 1$):during high tides, sea level rises over the mean sea level at the outlet and a GVF curve (M1) develops along the stream with an extent controlled by the relation between $y_0$ and $y_n$. This latter depth is determined by the river discharge ($Q$), stream roughness (represented as Manning coefficient, $n$) and stream slope ($S$) combination. The

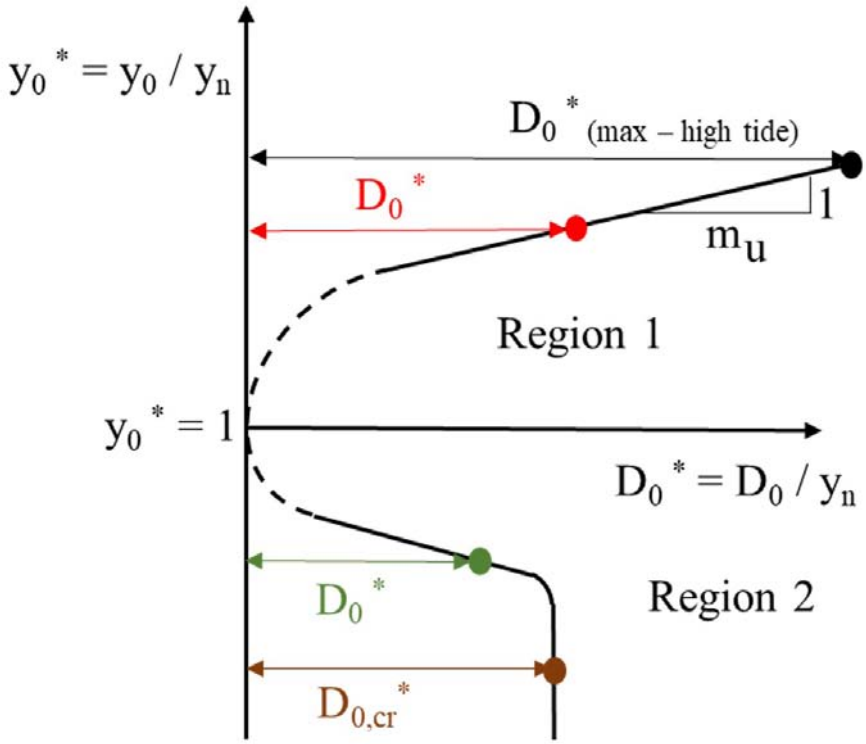


Figure 2.5.2: Theoretical behaviour of water profiles along the stream axis during a tidal cycle. Region 1 and 2 are split by $y_0^* = 1$ ($y_0 = y_n$), which corresponds to the transition region (dashed line).

highest tide leads to the maximum marine influence distance ($D_0^*$). A representative parameter ($m_u$) for this region is obtained as the slope of the curve $m_u = (D_0^*)/(y_0^*) = D_0/y_0$.

- Region 2 ($y_0^* < 1$):during low tides, sea level decreases below $y_n$ at the outlet. Similar to previous region, a GVF curve (M2) is extended along the stream depending on $y_0$ and $y_n$. The maximum distance ($D_{0,cr}$) corresponds to critical flow conditions (the Froude number is 1) at the outlet and remains constant for lower sea levels as the perturbation does not propagate upstream. This region is represented by $D_{0,cr}$.
- A transition region ($y_0^* \simeq 1$) can be observed when $y_n$ is similar to $y_0$ and no marine influence is obtained along the river.

Results show that those cases corresponding to low tide amplitudes, high discharges, steep slopes and/or low roughness tends to $y_0^* < 1$ during the entire tidal cycle, and only Region 2 is developed. Indeed, those cases with $y_0^* < 0.5$ during the entire tidal cycle, marine influence is limited to a constant $D_{0,cr}$. Figure (2.5.3) depicts the results for 6 representative cases with different input parameters that fit properly to the general behaviour described in Figure (2.5.2). For Region 1 ($y_0^* > 1$), those cases with different tide amplitude show the same $m_u$ value. Main changes are observed for those simulations with increasing stream slope. Regarding Region 2,

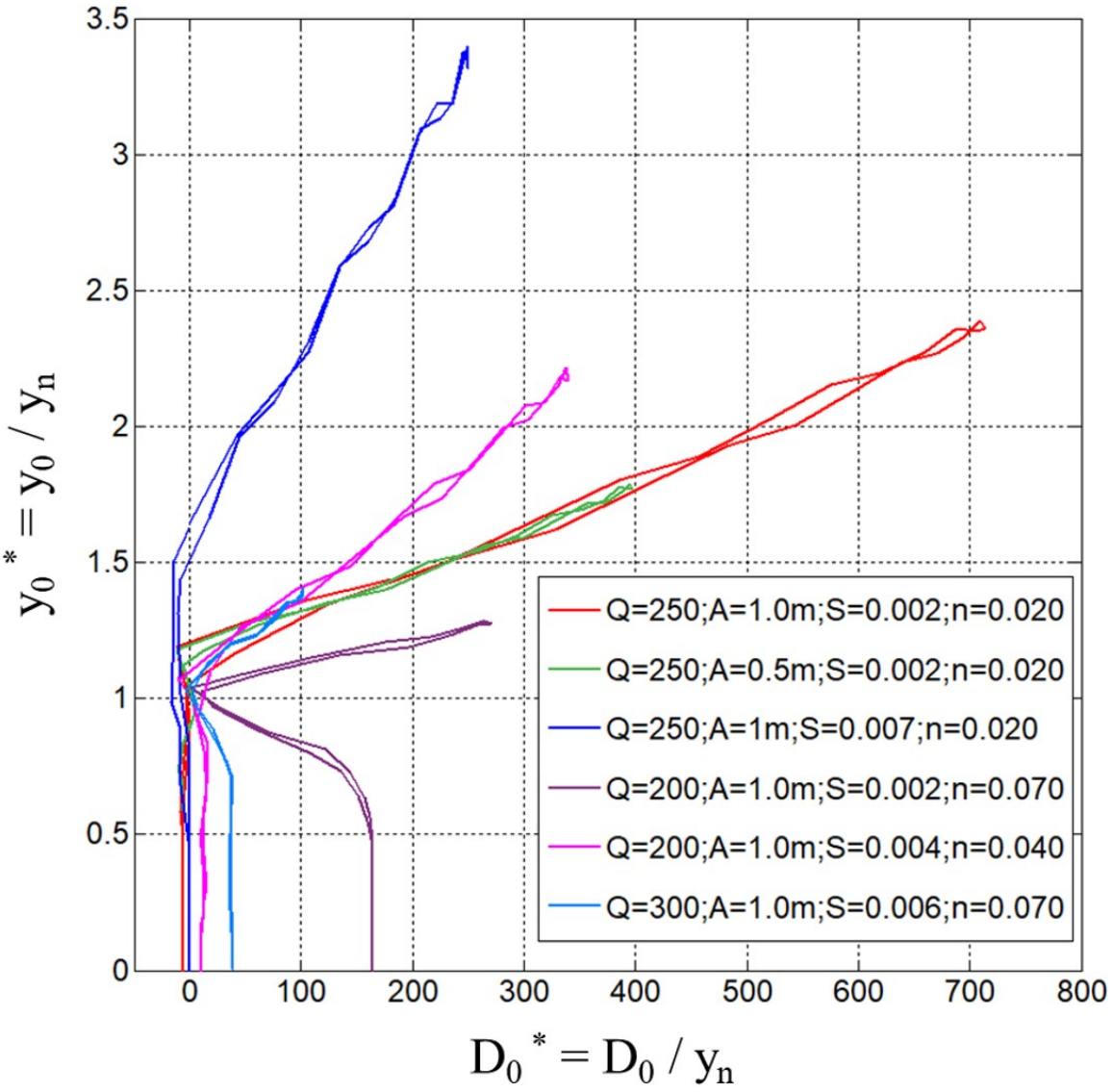


Figure 2.5.3: Example of representative simulations for different input parameters.Curve performance fits to general behaviour.

critical distances $D_0^*$ are located in a narrower interval and higher results are obtained for those simulations with higher stream roughness, lower discharges, and/or lower stream slopes.

Figure (2.5.4) is employed to analyse how $m_u$ varies as a function of input parameters at Region 1. In the figure, each point corresponds to a simulation, limited to those cases with $y_0 > y_n$ during the complete tidal cycle. X-axis classifies the simulation for different stream slopes, and Y-axis corresponds to $m_u$. Markers are used to differentiate stream roughness for each simulation. Scenarios with a higher slope ($S = 0.007$) lead to results for $m_u$ between 100 and zero, depending on stream roughness and $y_0^*$. For simulations with the lower slope ($S = 0.002$), $m_u$ results are located in a wider range, between 100 and 400, notably depending on stream roughness and $y_0^*$.

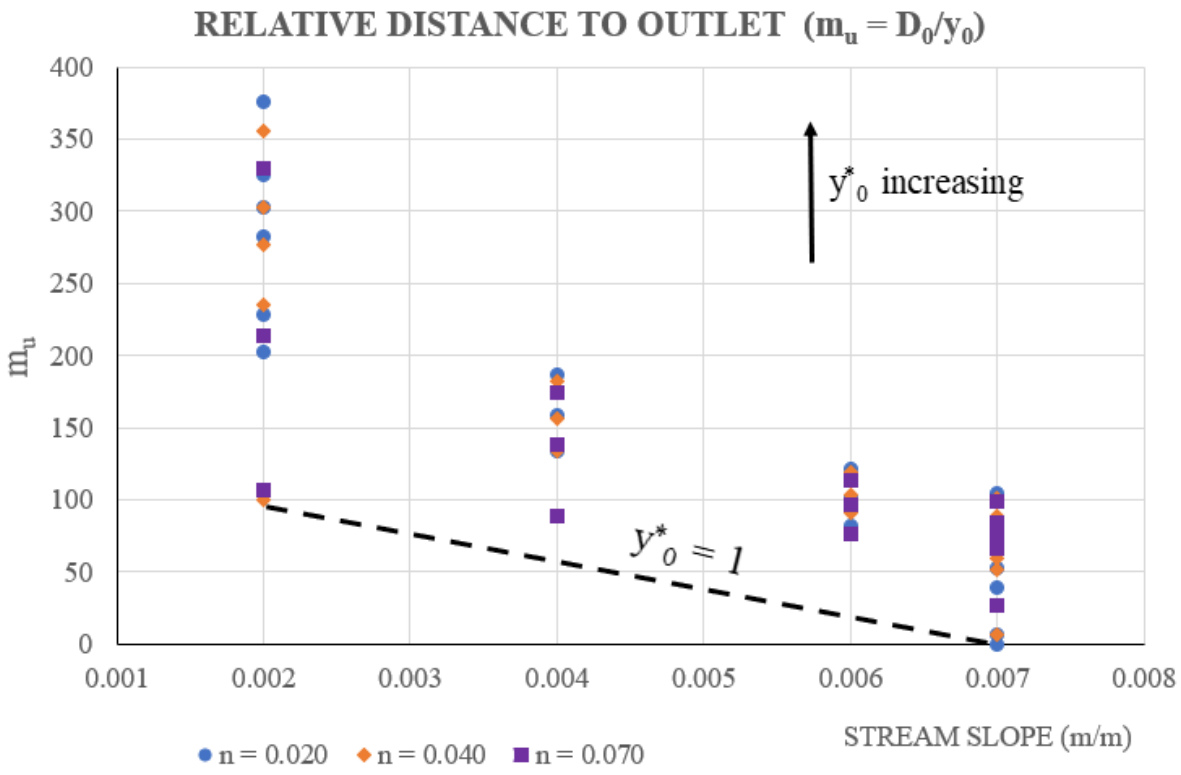


Figure 2.5.4: Results for $m_u$ (Region 1) of different simulations as a function of stream and roughness slope.

Cases with intermediate stream slopes show results in a transition zone between these two ones.

2.5.5 depicts $D^*_{0,cr}$ for Region 2. A wider range for this variable (0-250) is observed for those simulations with a lower stream slope ($S = 0.002$) whereas narrower intervals (0-70) are found for higher stream slopes, with no significant differences between $S = 0.004$ and $S = 0.007$. Furthermore, this figure reflects that higher stream roughness leads to higher $D^*_{0,cr}$.

## 2.6 Discussion

Within the tidal cycle, for $y^*_0 > 1$ (Region 1) the marine influence along the stream is characterized by an increase of water depth and a velocity reduction as the flow reaches the outlet. The previous results determine that the calculation of the maximum marine influence distance ($D_{0,max}$) along the river axis in this region, can be obtained using the following expression for a particular case:

$$D_{0,max} = m_u y_{0,max} \tag{2.7}$$

Therefore, the assessment of $D_{0,max}$ is reduced to the determination of $m_u$. According to 2.5.4, $m_u$ depends on $S$, $n$ and $y_{0,max}$.

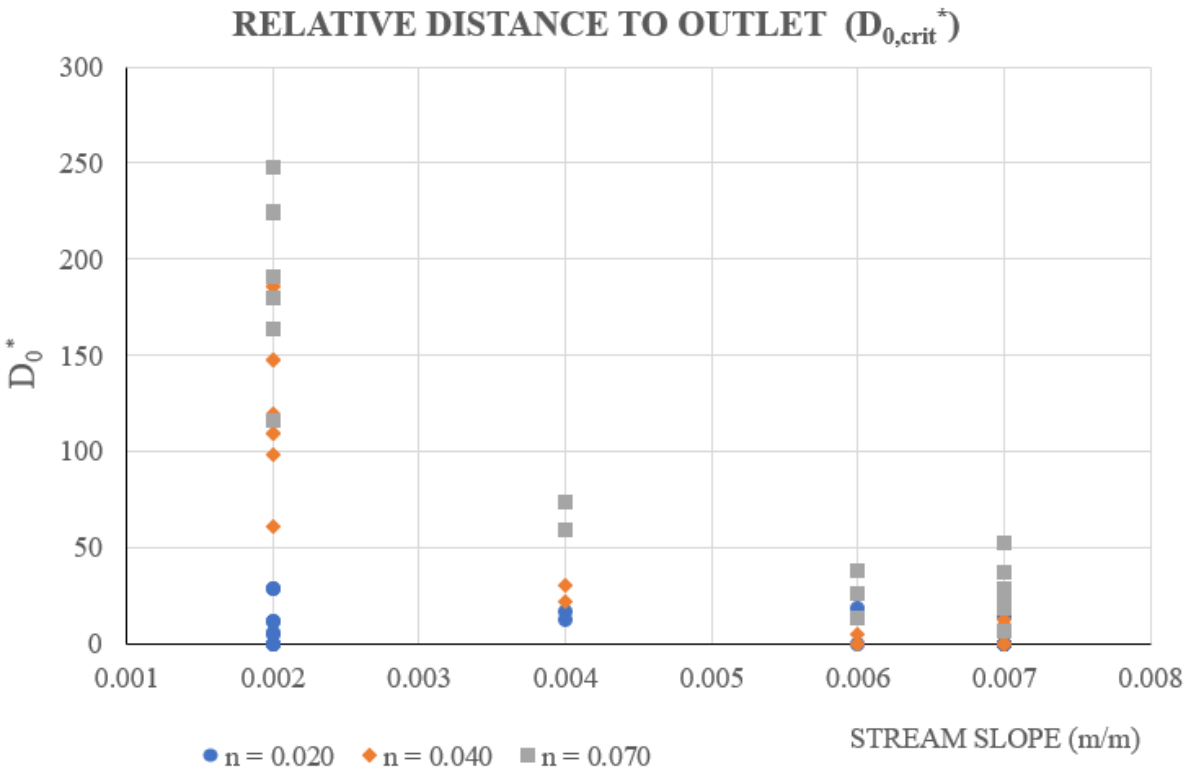


Figure 2.5.5: Results for critical $D_0^*$ (Region 2) of different simulations as a function of stream and roughness slope.

After the analysis of the results, stream slope stands out as the main parameter: a higher stream slope leads to a lower value of $m_u$, limiting the marine influence to a lower extent. As stream slope decreases, $m_u$ spreads in a wider interval and stream roughness and $y_{0,max}^*$ increase their relevance in the assessment of $m_u$. Hence, higher stream roughness and higher non-dimensional water level implies an increase of $m_u$. From these assumptions a general expression is proposed:

$$m_u = \left(y_{0,max}^* - 1\right)^{C_1} \left(\frac{1}{S}\right)^{C_2} n^{C_3} \tag{2.8}$$

This expression was fitted to the results ($R^2 = 0.953$) with $C_1 = 0.403$, $C_2 = 1.082$ and $C_3 = 0.320$. These values agree with Figure (2.5.4) highlighting the major influence of the stream slope in the assessment of $D_{0,max}$. The dependency on stream roughness emphasizes the importance of vegetation and maintenance conditions of the streams.

On the other hand, regarding Region 2, for $y_0^* < 1$ the marine influence along the stream is characterized by a water depth decrease and a velocity increase. In this case, the critical distance can be directly obtained as:

$$D_{0,cr} = D^*_{0,cr} y_n \tag{2.9}$$

Figure 2.5.5 shows that $D^*_{0,cr}$ depends on $S$, $n$, and $y_n$. Hence, the water level on the coastal platform ($y^*_{0,max}$) vanishes as a direct factor for the assessment. Note this calculation is based on the assumption that critical flow is developed in the river mouth section, what implies $D^*_0$ values are aligned on a vertical stretch of the curve showed in Figure (2.5.2).

Similar to previous calculations for Region 1, in Region 2 stream slope is the main parameter for the calculation: a higher stream slope leads to a lower value of $D^*_{0,cr}$. A significant spreading of results is observed between stream slopes of 0.002 and 0.004. Moreover, lower stream roughness and lower $y_n$ along the stream seems to lead to a reduction of $D^*_{0,cr}$, especially for those simulations with a lower stream slope. Based on these observations, this general expression is proposed:

$$D^*_{0,cr} = y_n^{C_4} \left(\frac{1}{S}\right)^{C_5} n^{C_6} \tag{2.10}$$

This expression was fitted ($R^2 = 0.916$) obtaining these coefficients: $C_4 = 0.507$, $C_5 = 1.228$ and $C_6 = 1.029$. In this case both friction and slope have a similar dependency, whereas the uniform flow conditions (i.e., the river discharge) is less important.

**Final remarks**

In this chapter, the interplay between river discharge and astronomical tides is analysed in order to identify the marine-fluvial boundary during extreme river floods at river mouths. This boundary is evaluated in terms of distance from the river mouth.

The results show that the frontier is closely related to river slope, river roughness and tidal conditions. A non-dimensional curve for the position of the frontier within a tidal cycle was constructed based on the determination of two representative parameters, and two experimental expressions are proposed for their practical calculation. According to the analysis, the river gradient emerges as the most important factor in determining the extent of the marine influence, with the bed roughness (i.e. vegetation, river conservation conditions) and the discharge/tidal conditions being particularly relevant for low values of the river gradient.

The detailed analysis of the location of this boundary contributes to a deeper knowledge of the dynamics of the river mouth and to the application of risk assessment procedures based on the identification of hazard areas classified by threshold values of water depth and velocity. The results also show that further research is needed to gain a better understanding of estuarine hydrodynamics under extreme river discharge and tidal influence, particularly with respect to flow velocities. The following two chapters are devoted to this.

CHAPTER 3

# RIVER MOUTH HYDRODYNAMICS: THE ROLE OF THE OUTLET GEOMETRY ON THE JET STRUCTURE

Throughout Chapter 2, an analysis of the influence of the geometry of the river mouth and the tidal range on the tidal excursion, and therefore on the extent of the zone of influence of the marine agents, has been carried out when analysing the hydrodynamics of river discharges. Once this zone of influence has been defined, the next step is to analyse the hydrodynamics themselves, and in particular the jet structure. To this end, this chapter describes the jet theory used in the literature for this analysis, as well as the application of the numerical model to idealised scenarios under conditions of constant discharge and without tidal effects. The results obtained allow us to analyse how the geometry of the outlet and the cross-shore nearshore profile determine the shape and structure of the jet. Subsequently, in Chapter 4, the analysis is completed with transient conditions of river discharge and sea level, thus completing the hydrodynamic analysis of the problem. The results of this chapter are presented in Ruiz-Reina and López-Ruiz (2024).

## 3.1 Introduction

The hydrodynamics of the river mouth is dominated by a confined turbulent jet flowing into a basin where waves, storm surges and astronomical tides can modify the shape and intensity with which this jet spreads laterally and reduces its seaward velocity. Outlet and nearshore geometries also play a key role in the evolution of this jet, modifying both the flow structure at the outlet and the propagation velocity once it enters the shelf. Consequently, the interaction between hydrodynamics and sediment is a feedback process in which the jet structure determines the sediment deposition, which in turn determines the morphology with the formation of features such as bars, which are crucial for the development of deltas.

To characterise jet hydrodynamics, authors such as Abramovich and Schindel (1963) and Özsoy and Ünlüata (1982) developed time-averaged solutions of the integral jet theory, in which the jet structure is divided into two zones: (1) the zone of flow establishment (ZOFE) near the outlet, where the flow leaves the channel and expands abruptly; and (2) the zone of established

flow (ZOEF) far from the outlet, where the flow is stable and similarity hypotheses can be applied (Ortega-Sánchez, Losada, and Baquerizo, 2008). From these pioneering works, this theory has been refined to describe a transition zone between the ZOFE and the ZOEF (Ortega-Sánchez, Losada, and Baquerizo, 2008), although in the last 15 years the focus has been on the use of process-based models to analyse the effects of jet hydrodynamics on bar development, analysing the effects of sediment size (Edmonds and Slingerland, 2007), levee formation (Rowland, Dietrich, and Stacey, 2010), human activities (Anthony, Marriner, and Morhange, 2014; Fan et al., 2006; Besset, Anthony, and Bouchette, 2019), frictional effects (Canestrelli et al., 2014) or the presence of vegetation (Nardin, Edmonds, and Fagherazzi, 2016; Lera et al., 2019).

In most of these works, simplified outlet geometries were defined using lower channel width to outlet depth ratios (Canestrelli et al., 2014). In addition, many of them have considered channels with no slope or very gentle slopes flowing into horizontal basins (Edmonds and Slingerland, 2007; Leonardi, Kolker, and Fagherazzi, 2015; Nardin, Edmonds, and Fagherazzi, 2016). Jiménez-Robles, Ortega-Sánchez, and Losada (2016) analysed the influence of shelf slope on jet hydrodynamics, defining the shelf as a surface with a constant slope. Their results show that this slope plays a very important role in the jet structure, and therefore in the formation of bars and their final geometry. Shortly afterwards, **Jimenez2018** also analysed the role of the river-shelf orientation.

The literature review suggests that the interactions between fluvial discharge and marine agents are very complex, although they are crucial for the management of river mouths and deltas. Furthermore, despite all the recent advances described above, there are still important aspects to be analysed in order to describe the jet structure at outlets. In particular, the effect of more realistic geometries, both in terms of characteristic outlet dimensions and platform shape, may have on the hydrodynamics already described for simpler geometries remains to be further explored.

The main objective of this chapter is to analyse the effect of outlet characteristics (ratio of outlet depth to channel width) and nearshore geometry on the jet structure. To achieve this goal, a process-based numerical model is used on idealised but realistic geometries where the channel and platform slopes, as well as the outlet shapes commonly observed in small river mouths with high seasonal variability and relatively high slopes due to their proximity to mountain ranges are maintained. To validate the numerical modelling, the simulations are compared with the jet theory, showing that the model adequately reproduces the hydrodynamics for the simplest cases for which the solutions of this theory have been developed, while for more complex and realistic situations this theory has limitations that the model is able to overcome. Once validated, the model results are analysed in terms of the longitudinal and transverse distribution of the velocity field, as well as in terms of the momentum balance, which allows us to describe how the geometric characteristics of the river mouth influence the structure of the jet and, in particular, the boundary in the ZOFE and ZOEF.

## 3.2 The jet theory

Jet theory has been used extensively in recent decades to describe the jet that develops when a river discharges into a still water basin, with fluvial forces dominating over marine forces (Wright, 1977). In particular, the dominant primary force is a combination of inertia and turbulent bed

friction, i.e. a river discharges into a still body of water with the same density as the incoming river (Fagherazzi et al., 2015), and no buoyancy effects are considered. At river mouths, the flow can be described by the shallow water equations (Özsoy and Ünlüata, 1982; Leonardi et al., 2013) due to the larger ratio of outlet depth to channel width ($W/h_0 > 4$). The hydrodynamics of such a turbulent jet, also called a shallow bounded plane jet (Fagherazzi et al., 2015), can be divided into two zones: (1) a zone of flow establishment (ZOFE), in the vicinity of the outlet, characterised by a core of constant velocity and rapid momentum dissipation; and (2) the zone of established flow (ZOEF), dominated by the turbulent eddies and centreline velocity decrease with a Gaussian transverse distribution of the velocity profile (Özsoy and Ünlüata, 1982; Jirka and Giger, 1992).

An extensive body of work has been developed for an integral plane jet theory assumed to be incompressible, stationary, depth-constant and frictionless (Jiménez-Robles, Ortega-Sánchez, and Losada, 2016). A more complex analysis was developed by Özsoy and Ünlüata (1982) for ebbing flows at microtidal inlets, incorporating the effects of bottom friction to analytically solve the depth-averaged equations of motion under the assumptions of quasi-steadiness and self-similarity. The equations of motion (mass and along channel momentum balance) for the jet are (Özsoy and Ünlüata, 1982):

$$\frac{\partial(hu)}{\partial x} + \frac{\partial(hv)}{\partial y} = 0 \tag{3.1}$$

$$\frac{\partial(hu^2)}{\partial x} + \frac{\partial(huv)}{\partial y} = -\frac{f}{8}u^2 + \frac{1}{\rho}\frac{F_{xy}}{\partial y} \tag{3.2}$$

where $h$ is the water depth, $u$ and $v$ are the depth-averaged velocity components in the $x$ and $y$ directions (Fig. 5.4.1), $\rho$ is the water density, $F_{xy}$ is the depth-integrated turbulent shear stress, and $f$ is the friction factor, which can be expressed as a function of the Chezy number ($f = 8g/C_z^2$). To solve eqs. 3.1 and 3.2 along the channel centreline ($y = 0$, Fig. 5.4.1) and obtain $u_c(x) = u(x,0)$, the velocity distribution $u(x,y)$ is assumed to be self-similar with respect to the normalised coordinate $\zeta = y/b(x)$, where $b(x)$ is the half-width of the jet, which facilitates the integration of the equations of motion. According to (Abramovich and Schindel, 1963), the velocity field is parameterised as follows, where $F(\zeta) = u(x,y)/u_c(x)$:

$$F(\zeta) = \begin{cases} 0 & 1 < \overline{\zeta} \\ \left(1 - \overline{\zeta}^{1.5}\right)^2 & 0 < \overline{\zeta} < 1; \quad \overline{\zeta} = \dfrac{\zeta - r/b}{1 - r/b} \\ 1 & \overline{\zeta} < 0 \end{cases} \tag{3.3}$$

where $r(x)$ is the core width which vanishes at $x = x_s$, the boundary between ZOFE and ZOEF. The integration of equations 3.1 and 3.2 is based on the assumption that $u(x,y)$ and $F_{xy}$ decrease as $y$ increases, but with consideration of a lateral entrainment velocity $v_e = v(x,y)|_{y\to\infty} = au_c$, where $a$ is the entrainment coefficient. When the following normalised variables are introduced (Özsoy and Ünlüata, 1982)

$$\xi = \frac{x}{b_0}; \quad \mu = \frac{f b_0}{8h_0}; \quad H(\xi) = \frac{h}{h_0}; \quad R(\xi) = \frac{r}{b_0}; \quad B(\xi) = \frac{b}{b_0}; \quad U(\xi) = \frac{u_c}{u_0}; \tag{3.4}$$

two ordinary differential equations are obtained for both regions:

$$\frac{d}{d\xi}(I_1 HBU) = aHU \tag{3.5}$$

$$\frac{d}{d\xi}(I_2 HBU^2) = -\mu I_2 BU^2 \tag{3.6}$$

Where $b_0$, $h_0$, and $u_0$ are respectively the half-width, depth and velocity at the outlet. The non-dimensional flow establishment distance is expressed as $\xi_s$.

If the analysis is restricted to the ZOEF, the numerical constants $I_1$ and $I_2$ can be obtained as 0.450 and 0.316 (Özsoy and Ünlüata, 1982), respectively, after integrating $F^n(\xi)$ between 0 and 1 ($n = 1,2$). The solution of the ODE system (eqs. 3.5 and 3.6), and hence the jet structure, is strongly dependent on the nearshore profile geometry $H(\xi)$. Previous works mainly analysed turbulent jet hydrodynamics for horizontal beds, where $H = 1$ (Edmonds and Slingerland, 2007; Nardin and Fagherazzi, 2012; Leonardi, Kolker, and Fagherazzi, 2015), or for sloping beds with constant slope $m$, where $H = 1 + \nu\xi$ and $\nu = mb_0/h_0$ (Jiménez-Robles, Ortega-Sánchez, and Losada, 2016). However, these are simplified geometries of the nearshore profile that in nature presents a variable slope with a corss-shore variations of the water depth that can be described by its equilibrium shape $h(x) = Ax^{2/3}$ (Dean and Dalrymple, 2004), where $A$ is the profile scale factor, a dimensional parameter that depends on the sediment size (Dean and Dalrymple, 2004). This elliptical profile, after non-dimensionalisation, is expressed as $H = 1 + k\xi^{2/3}$, where $k = Ab_0^{2/3}/h_0$. The numerical solution of the ODE system using a finite difference scheme described in Appendix 3.3 is implemented to obtain $u_c$ for the three geometries described above. These results are used to validate the simulations performed with the depth-averaged 2D hydrodynamic model for steady-state conditions (still water level and constant river discharge) shown in section 4.1.

Finally, as mentioned above, the transverse distribution of the velocity field in the ZOEF region shows a Gaussian profile that can be approximated with sufficient accuracy for the purposes of this work by the following expression (Jirka and Giger, 1992), with $A = -Ln(0.5) = 0.693$.

$$\frac{u(x,y)}{u_c(x)} = e^{-A\zeta^2} \tag{3.7}$$

## 3.3 Solution of the turbulent jet theory

The numerical solution for the turbulent jet theory was obtained to validate the results from the Delft3D modelling by using a simple finite difference scheme for the ODE system defined by eqs. 3.5 and 3.6. If the nondimensional along channel coordinate $\xi$ is discretized into $i = 1,2,...N$ points equally spaced by the distance $\Delta\xi$, the use of an explicit forward difference for $\xi$ reads as follows:

$$U_{i+1}B_{i+1} = \frac{1}{I_1 H_{i+1}}(I_1 H_i U_i B_i + a\Delta\xi H_i U_i) \tag{3.8}$$

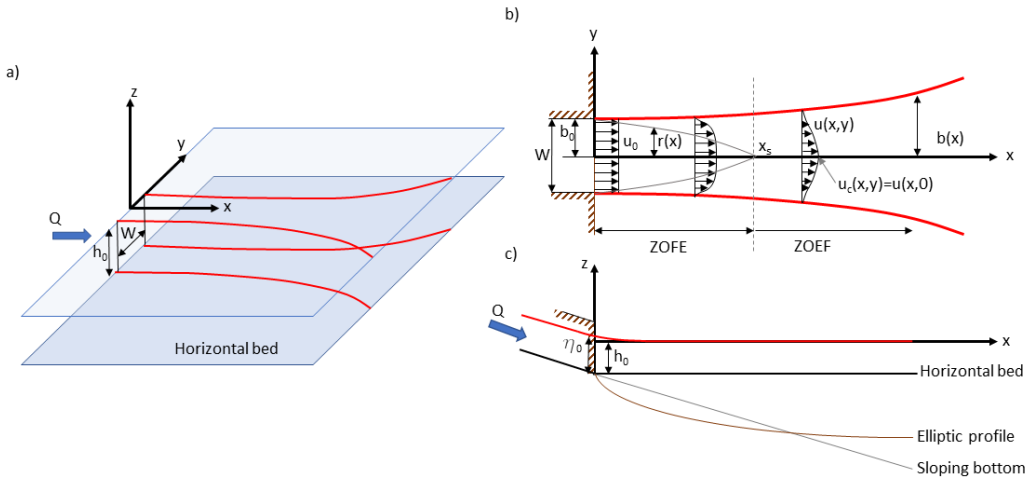


Figure 3.2.1: a) Definition sketch of a horizontal bounded jet. b) Zone of Flow Establishment (ZOFE) and Zone of Established Flow (ZOEF). $Q$ is the river discharge, $h_0$ is the outlet depth, $\eta_0$ is the water level at the outlet, $W$ is the mouth width, $b_0$ is the mouth half-width, $u_0$ is the mean outlet velocity, $u_c(x)$ is the jet velocity along the axis, $u(x,y)$ is the streamwise velocity, $b(x)$ is the jet half-width, and $x_s$ is the flow establishment distance. Panel c) shows the three considered nearshore profiles

$$U_{i+1}^2 B_{i+1} = \frac{1}{H_{i+1}} \left( H_i U_i^2 B_i - \mu \Delta\xi B_i U_i^2 \right) \tag{3.9}$$

Eqs. 3.8 and 3.9 define a system of two equations with $U_{i+1}$ and $B_{i+1}$ as unknowns, which can be solved at any point along the jet axis using $U_{i=1} = 1$ and $B_{i=1} = 1$ as boundary conditions at the outlet $x = 0$.

To validate this numerical scheme, the results for simple geometries (horizontal and sloping beds) were compared with the analytical solutions obtained by Özsoy and Ünlüata (1982), who obtained the following expression for $U(\xi)$ along the ZOEF using the functions $J(\xi)$ and $L(\xi)$:

$$J(\xi) = \exp\left( -\mu \int_0^{\xi} \frac{d\xi'}{H(\xi')} \right) \tag{3.10}$$

$$L(\xi) = \frac{2aI_2}{I_1} \int_{\xi_s}^{\xi} H(\xi') J(\xi') d\xi' + J^2(\xi_s) \tag{3.11}$$

$$U(\xi) = J(\xi) L(\xi)^{-1/2} \tag{3.12}$$

being $\xi_s = x_s/b_0$. The solution for an horizontal bed ($H = 1$) is (Özsoy and Ünlüata, 1982):

$$U(\xi) = e^{-\mu\xi}\left[e^{-2\mu\xi_s} + \frac{2aI_2}{\mu I_1}\left(e^{-\mu\xi_s} - e^{-\mu\xi}\right)\right]^{-1/2} \tag{3.13}$$

For a sloping bottom with constant slope $m$, considering $H = 1 + \nu\xi$ and $\nu = mb_0/h_0$, the solution is:

$$U(\xi) = H^{-\mu/\nu}\left[H_s^{-2\mu/\nu} + \frac{2aI_2}{I_1(2-\mu/\nu)}\left(H^{2-\mu/\nu} - H_s^{2-\mu/\nu}\right)\right]^{-1/2} \tag{3.14}$$

Fig. (3.3.1) compares the results for the two proposed geometries for which the analytical solution is known: i) horizontal bed; ii) flat bed with a slope of $m = 0.05$ and iii) bed with an elliptical profile, for which only the numerical solution is shown. For these calculations the following parameters were used: $C_z = 55$; $h_0 = 1.0$m; $a = 0.05$, which are realistic values and will be used in the following simulations. A good fit is observed for the horizontal bed case as well as for the sloped bottom case, although the latter gives maximum differences around 20% for $\xi = 9.0$, which are considered acceptable since they are punctual. Thus, from this theoretical basis and with the support of the numerical resolution of the three proposed cases, a solution derived from the jet theory is available to compare the results of the simulations carried out throughout the manuscript.

## 3.4 Numerical experiments

### Physical scenarios

The physical scenarios in which the Delft3D model was implemented represent a straight channel flowing into a basin representing the continental shelf. To analyse the role of the mouth geometry on the jet structure, three parameters were varied: (1) the width of the channel $W$; (2) the depth of the channel at the outlet with respect to mean sea level (hereafter MSL) $h_0$; and (3) the geometry of the continental shelf.

The channel geometry was defined with a rectangular cross section perpendicular to the shoreline orientation. This channel has a width $W_i = (100, 200, 500)$ m and a longitudinal slope $S_s = 0.002$. The lateral edges of the section are vertical walls with a height greater than 4 m at each section to prevent overtopping and to ensure mass conservation between the upstream boundary condition and the outlet. The depth of the outlet is $h_{0i} = (1, 3)$ m. The channel length is 2.5 km, which ensures that the tidal excursion can be simulated correctly while avoiding the numerical effects of the upstream boundary condition.

The shoreline is straight and the geometry of the beach profile was defined as (1) a horizontal bottom with depth $h_{0i}$; (2) a bottom with constant slope $S = 0.05$; and (3) a bottom with the equilibrium elliptical shape defined by Dean and Dalrymple (2004) (see Ruiz-Reina and López-Ruiz, 2021 for further details). This elliptical shape is concave and therefore more realistic in the shallower part of the continental shelf. Finally, the platform is extended to the offshore boundary

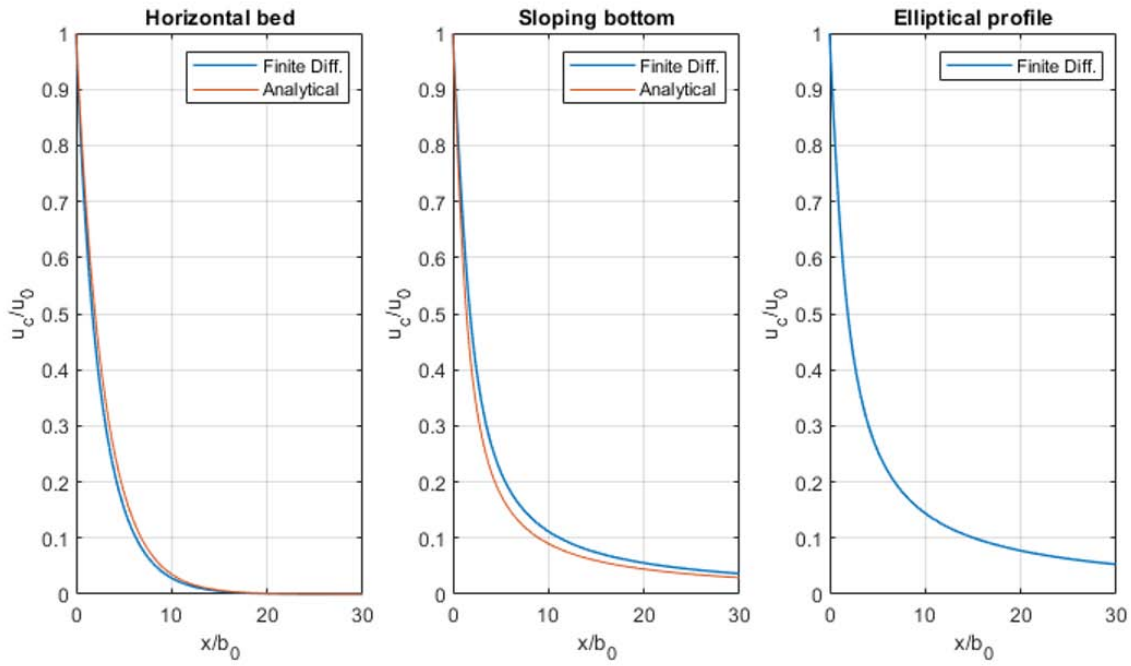


Figure 3.3.1: Dimensionless solutions for the streamwise velocity of a bounded jet along the axis ($u_c$) for horizontal, sloping bottom and elliptical profiles (from left to right) obtained with the analytical and numerical solutions (orange and blue lines, respectively).

of the domain with maximum depths above 50 m. The combination of $W_i$, $h_{0i}$ and platform geometries configures a set of 18 physical scenarios (see table 4.2).

## Numerical model

Similarly to chapter 2, the physical scenarios described in Section 3.1 were implemented using a regular grid of quadrangular cells aligned with the channel axis and the shoreline. To improve the efficiency of the simulations, the cell size varies from 100x100 m$^2$ at the offshore boundary to 10x10 m$^2$ at the outlet. This grid was previously used by Ruiz-Reina and López-Ruiz (2021), where the numerical results were already validated. In order to meet the stability and accuracy requirements of the numerical scheme, a time step of 1.5 s was used. As in (Ruiz-Reina and López-Ruiz, 2021), constant coefficients were used for the bed roughness ($C_z = 55$) and the background horizontal eddy viscosity ($\epsilon_H^{back} = 1$ m$^2$/s) over the computational grid.

Three types of open boundaries were defined to analyse the role of the outlet and nearshore geometry in the jet structure under conditions equivalent to those used to define the plane-turbulent jet theory described in section 2: (1) the offshore boundary, with constant water level conditions $\eta = 0$ during the entire simulation; (2) the upstream boundary, located in the very upstream part of the channel, with constant discharge rate per unit channel width $q = Q_i/W_i = 2.5$ m$^2$/s; and (3) two cross-shore boundaries, where Neumann-type conditions were used, imposing a zero water level gradient in the direction perpendicular to the boundary (Roelvink and Walstra, 2004). As there are three values of $W_i$ among the defined physical scenarios, three discharge

| Type | Id | Profile | $W$ (m) | $h_0$ (m) | $Q_p$ (m$^3$/s) | Offshore | $\phi$ (rad) |
|---|---|---|---|---|---|---|---|
| | 111 | | 100 | | 250 | | |
| 1 | 121 | Horizontal | 200 | 1.0 | 500 | Still water | - |
| | 151 | | 500 | | 1250 | | |
| | 211 | | 100 | | 250 | | |
| 1 | 221 | Sloping | 200 | 1.0 | 500 | Still water | - |
| | 251 | | 500 | | 1250 | | |
| | 311 | | 100 | | 250 | | |
| 1 | 321 | Elliptical | 200 | 1.0 | 500 | Still water | - |
| | 351 | | 500 | | 1250 | | |
| | 113 | | 100 | | 250 | | |
| 1 | 123 | Horizontal | 200 | 3.0 | 500 | Still water | - |
| | 153 | | 500 | | 1250 | | |
| | 213 | | 100 | | 250 | | |
| 1 | 223 | Sloping | 200 | 3.0 | 500 | Still water | - |
| | 253 | | 500 | | 1250 | | |
| | 313 | | 100 | | 250 | | |
| 1 | 323 | Elliptical | 200 | 3.0 | 500 | Still water | - |
| | 353 | | 500 | | 1250 | | |

Table 3.4.1: Numerical scenarios: main characteristics.

values $Q_i = (250, 500, 1250)$ m$^3$/s were used for $q$. Keeping $q$ constant allows to analyse the effect of channel geometry and $W/h_0$ ratio without altering the results due to the different averaged velocities at the outlet section.

## 3.5 Results

### Comparison to jet theory

The numerical modelling was validated by comparing its results with those obtained using the jet theory. Comparing the results of the streamwise velocity along the channel axis for the horizontal geometries and $h_0$ = 1 m (Fig. 3.5.1a), the model solution agrees with the analytical results in the initial part of the jet for the cases with a narrower mouth $W$ =(100, 200) m, but differs in the downstream part. However, there are significant differences between the two solutions for $W$ = 500 m, scenario with a significant higher $W/h_0$ than those for which the jet theory was developed. These differences may be due to the decrease of the role played by friction as $W/h_0$ increases. Consequently, a better fit was obtained for those simulations with a horizontal bed and $h_0$ = 3 m. Furthermore, it can be observed that to find a good fit, an initial $\xi_s$ =(0.0, 1.0, 0.7) for $W$ =(100, 200, 500)m is used. In addition, the analytical solution tends to zero as the jet moves towards the offshore boundary, while the model shows a lower streamwise velocity reduction along the nearshore, especially for the case of $W$ =500m.

For the sloping bottom simulations there are notable differences with respect to those with a horizontal bed. For the cases with $h_0$ = 1 m, the velocity profile for the numerical model results has a local maximum at about $\xi$ =2.0, from which the velocities decrease. This maximum is

related with the balance between jet contraction and its energy dissipation as it advances along the nearshore profile, as showed in the next section. This shape of the velocity profile is more pronounced for simulations with $W$ =(200, 500)m, showing the influence of $W$ on the jet structure. In comparison with the jet theory, a good fit can be observed for approximately every simulation from $\xi$ =4.0. The simulations with sloping bottom and $h_0$ = 3 m agree with these results, although in these cases the velocity profile is constantly decreasing for $W$ =100 m, while it shows a slight increase for $W$ =200 m, and for $W$ =500 m a relative maximum of the velocity is observed in the vicinity of $\xi$ =1.5, in agreement with previous results.

The elliptical profile simulations show velocities very similar to the previous sloping bottom results, with a local maximum velocity observed at $\xi$ =1.5-2.5. The similarity of these results shows that the variable slope of the elliptical nearshore profile does not affect the shape of the velocity profile at distances close to the mouth. However, it can be observed that $u_c/u_0$ is higher for the elliptical profile simulations than for those with a sloping bottom. The fit between the numerical models and the jet theory is particularly good for $h_0$ = 3m and $W$ =(100, 200)m. Therefore, for the $W/h_0$ ratios for which the jet theory solution was developed, the numerical model satisfactorily reproduces the jet behaviour that has been extensively analysed in the literature (Abramovich and Schindel, 1963; Özsoy and Ünlüata, 1982; Jirka and Giger, 1992; Fagherazzi et al., 2015).Therefore, the numerical model is a valuable and reliable tool to analyse the jet structure and the hydrodynamics of the river mouth, but its applicability is much wider than the jet theory, as it can be extended to more complex and realistic geometries with higher $W/h_0$ ratios. Furthermore, the results in Fig. (3.5.1) show that the local maximum on the velocity profile has implications for the location of the transition between the ZOFE and the ZOEF, which will be discussed in the next sections.

### Streamwise velocity of the jet

Fig. (3.5.2) shows the depth-averaged velocity contours near the outlet for the 18 numerical experiments. In this graph, the distances from the outlet are given in absolute dimensions to show the velocity isolines in a more realistic manner. The results show that the profile geometry determines the jet shape: while the horizontal bed shows an expanding jet with velocity contours extending away from the jet axis, the sloping and elliptical profiles show a contracted jet. This phenomenon was already identified by Özsoy and Ünlüata (1982), who pointed out that with increasing depth the jet contracts due to mass conservation, while the centreline velocity remains constant. The numerical results reproduce this behaviour for more complex geometries. Therefore, the effect of increasing depth is to suppress the jet expansion due to bottom friction, which becomes less dominant. The results also show that the transition from an expanded to a contracted jet occurs for bottom slopes between 0.00 (horizontal) and 0.05 for both $h_0$ values.

The jet contraction in simulations with sloping and elliptical profiles is similar, but there are two main differences: i) the jet width is slightly higher in simulations with elliptical profiles, due to the lower slope of the bed profile from a certain distance from the mouth (x=100 m); and ii) the distance over which the jet contraction extends also depends on the bed profile, but the influence of the mouth width is more relevant. Fig. (3.5.2) clearly shows that the contraction for $W$ = 500 m extends over a greater distance than those with smaller widths.

Focusing on the role of $h_0$, the analysis of the results for the horizontal bed leads to similar conclusions. For $h_0$ = 1 m the jet is wider because bottom friction dominates. In contrast, for

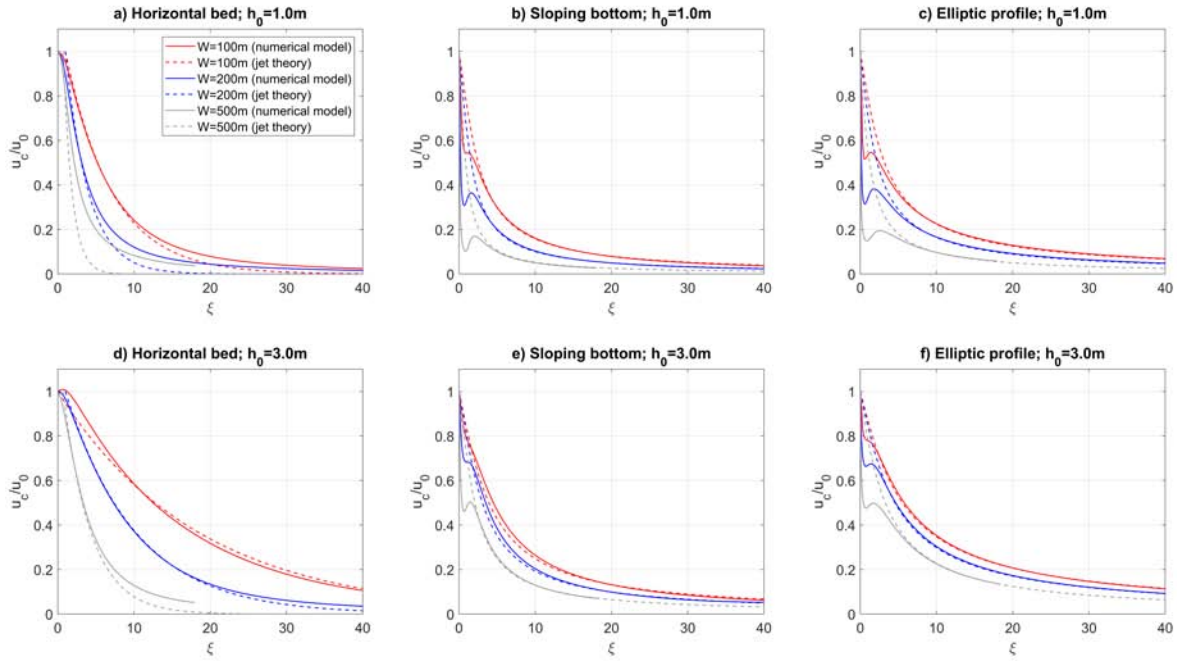


Figure 3.5.1: Velocity profiles obtained with the numerical model (solid line) and the jet theory (dashed line). The X axis represents the non-dimensional distance to the outlet, whereas the Y axis represent the non-dimensional streamwise velocity.

$h_0 = 3$ m the effect of bottom friction diminishes and the jet reduces its spreading. Furthermore, for the sloping and elliptical profiles, the velocity distribution in the sections near the mouth (Fig. 3.5.3) shows that the maximum velocity at the mouth and in the downstream sections is located along the edges of the jet for simulations with $h_0 = 1$ m, whereas for simulations with $h_0 = 3$ m it is located along the jet axis. In the first case, this effect is pronounced for $W$ =(500, 200)m, but barely noticeable for $W$ = 100m. The factors controlling the structure and the location of the maximum velocities are $h_0$ mainly, and secondly $W$. As discussed in section 5, these differences in the jet structure may play a significant role on the river mouth morphodynamics.

The outlet depth $h_0$ also has a direct effect on the mean outflow velocity ($\overline{u_0}$), with lower values of $h_0$ associated with higher values of velocity. When the jet flows into the nearshore the streamlines are contracted towards the jet axis. This phenomenon leads to a profile with two maxima at the edges of the jet ($h_0 = 1$ m) or with the maximum at the axis ($h_0 = 3$ m). It can be concluded that for a given $h_0$, and therefore for a given velocity, the velocity peaks at the edges are similar to the velocity at the centre and the cross-sectional velocity distribution adopts a shape with a single maximum at the axis.

This can be observed in more detail in Fig. (3.5.3). The maximum velocities for $h_0 = 1$ m are significantly higher (about twice) than for $h_0 = 3$ m. In addition, simulations with $h_0 = 1$ m and $W$ =(200, 500) m show a velocity profile with two peaks at the edges of the jet, regardless of the ocean geometry. However, for cases with $W$ =100 m, this profile tends to show a single peak velocity along the jet centre. For $h_0 = 3$ m, simulations with $W$ =(200, 500) m tend to

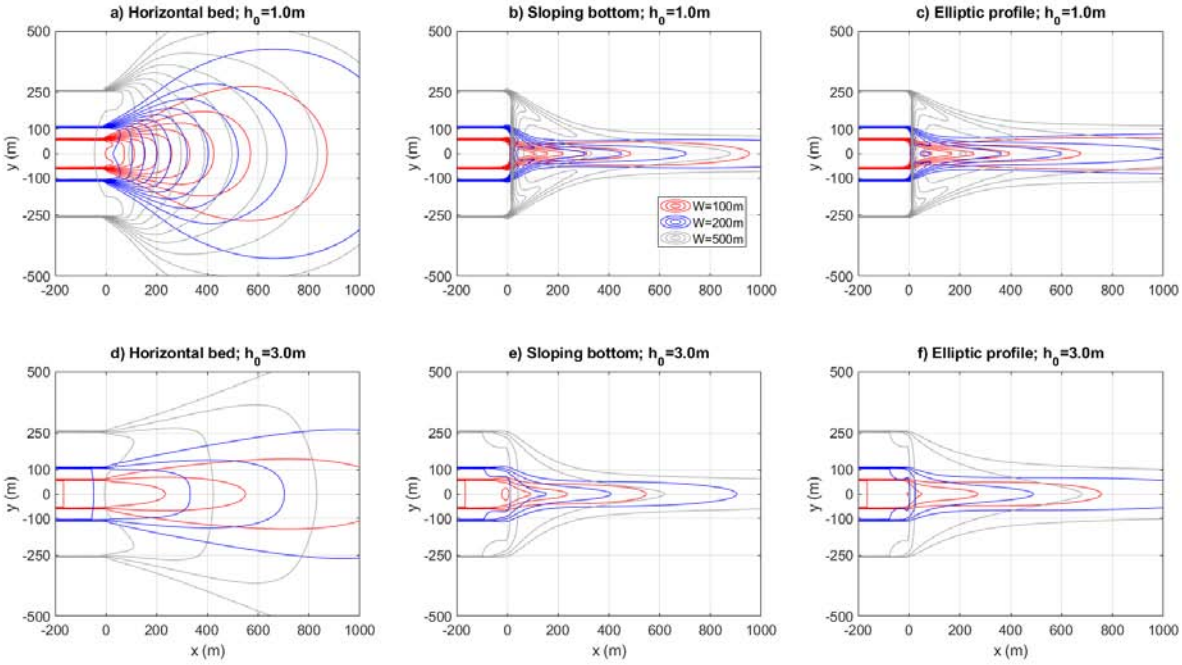


Figure 3.5.2: Streamwise velocity isolines $[0.0 - 2.0m/s]$ in intervals of $0.2m/s$. First row and second row correspond to simulations with outlet depth $h_0 = [1.0m, 3.0m]$, respectively. First column shows those simulations with horizontal bed; second column is related to sloping bottom geometry, and third column corresponds to a elliptical profile for the marine geometry. Each panel shows results for simulations with three different mouth widths: $W = 100$ m in red, $W = 200$m in blue and $W = 500$m in grey.

have velocity profiles with a constant value at the top, decreasing towards the jet boundaries, consistent with the description of the jet theory at the ZOEF region. Simulations with a narrower width ($W$ =100 m), as in the previous results, clearly show a velocity profile with a peak velocity along the jet centre. This means that in these cases the flow is fully established in this section. The similarity of the results for geometries with sloping and elliptical profiles is due to the value of the longitudinal slope of the nearshore profile, as both profiles have a similar slope for the first 100 m. Beyond this distance, the slope of the elliptical profile remains lower, implying a shallower bottom depth and leading to a smaller reduction in streamwise velocity and a larger jet width at these distances.

These results show that $W$ plays a significant role in determining the distance of flow establishment and hence the jet structure. Furthermore, $\overline{u_0}$, which is closely related to $h_0$, is a key parameter in defining the streamwise velocity profile, i.e. shallower outlets imply streamwise velocity profiles with two peak velocities along the edges of the jet, while deeper outlets are associated with velocity profiles with a single peak velocity along the jet axis.

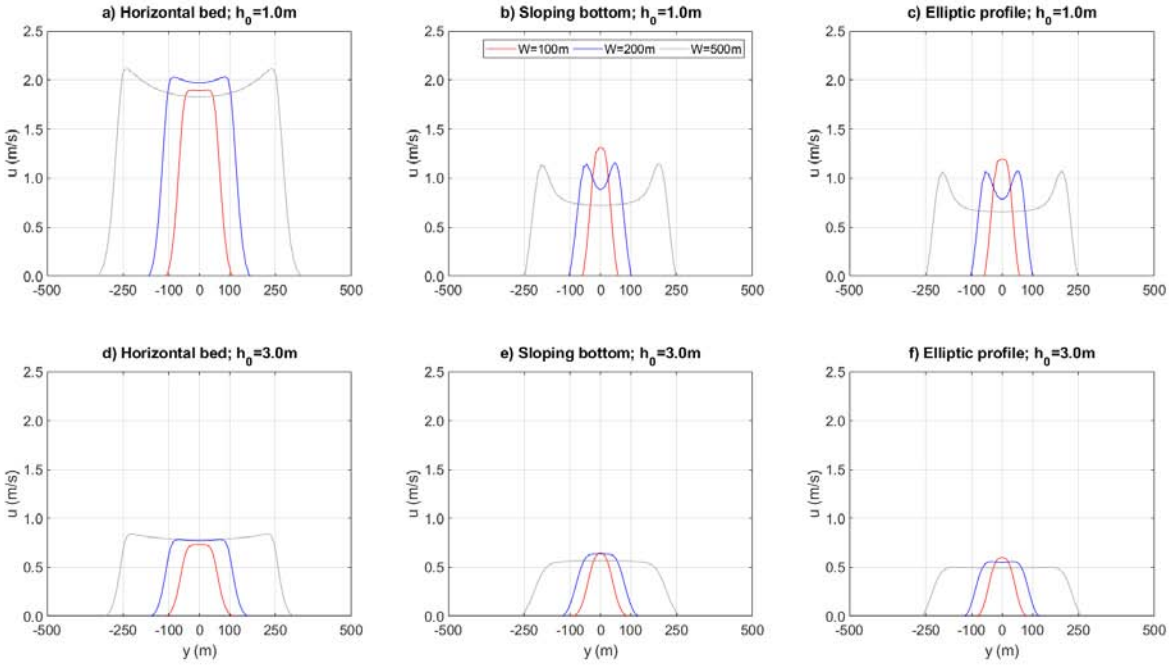


Figure 3.5.3: Transverse distribution of the streamwise velocity for a section located at 50 m, in the ZOFE for every simulation. Symbology and distribution of the panels are similar to Fig. (3.5.2).

### Transverse component of the velocity

Fig. (3.5.4) shows the non-dimensional transverse component of the velocity $v/u_c$ at $\xi = 4$ and $\xi = 7$, two sections where the flow is clearly established. The velocity trends are similar to those described in Jiménez-Robles, Ortega-Sánchez, and Losada (2016). For the horizontal bed cases, the velocity magnitudes are larger, with maxima in the region of $v/u_c = 0.5$, while for the sloping and elliptical profiles and $h_0 = 1$ m, $v/u_c$ is below 0.1 at both cross sections.

Fig. (3.5.4) also shows differences in the flow direction for the horizontal bed simulation on either side of the jet axis, so that the negative values are on the left and the positive values on the right. This sign criterion corresponds to a jet expanding with a transverse velocity that has its maximum at a point located at a distance equal to the half-width of the jet ($\zeta = 1$) for $h_0 = 1$ m and slightly closer the mouth for $h_0 = 3$ m. On the other hand, for the sloping and elliptical profiles, a change of sign is also observed in the velocities on either side of the jet, indicating a contracting jet. These two geometries show very similar magnitude and shape of the transverse velocity profile for simulations with $h_0 = 1$ m and $h_0 = 3$ m. The magnitude of the transverse velocity with respect to the streamwise velocity indicates that the jet is contracting weakly, so there is no significant variation in its width. It can be noted that the parameter $h_0$ has a relevant influence only for geometries with a horizontal bottom.

The analysis of the transverse velocity shows that for sloping bottom geometries there is a value of slope for which the jet width is constant. As stated by Özsoy and Ünlüata (1982), the

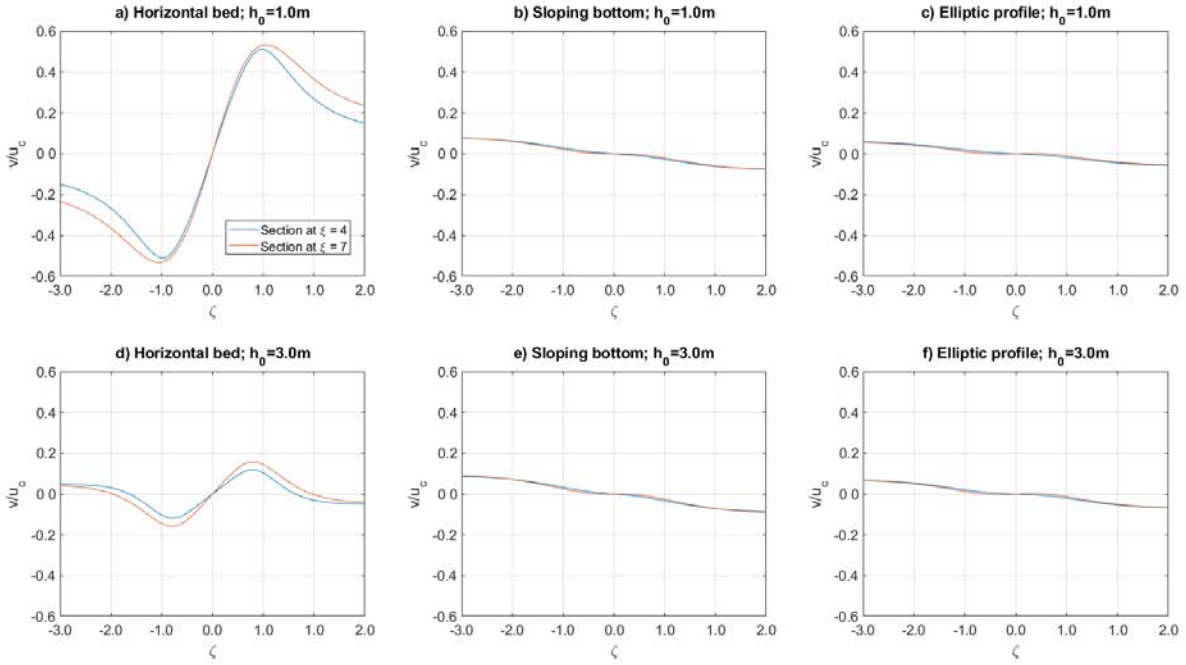


Figure 3.5.4: Non-dimensional Transverse component of the velocity at $\xi = 4$ and $\xi = 7$ for simulations with $W = 200$m. The velocity is non-dimensionalized with the streamwise velocity along the axis, and the X-axis is non-dimensionalized with the half-width of the mouth width.

width of the jet depends on the balance between the entrainment coefficient, $\mu$ and $\nu$. Excluding the influence of the former, with the values used for roughness, half-width and mouth depth (i.e. n, $b_0$, $h_0$), we obtain that this slope value is around $S_s = 0.0327$ for the cases with $h_0 = 1$ m and in the region of $S_s = 0.0225$ for those with $h_0 = 3$ m. This result is consistent with those obtained by Jiménez-Robles, Ortega-Sánchez, and Losada (2016).

## 3.6 Momentum balance and jet expansion/contraction

According to Wright (1977), the main depth-averaged processes that dominate the momentum balance in the spreading of river-dominated jets are: (i) inertia and momentum transport, (ii) turbulent bed friction, and (iii) acceleration due to water level variations (the barotropic term). The momentum balance for the simulations performed with constant discharge are in agreement with Wright (1977), showing that among the terms in momentum equations, these three terms are at least one order of magnitude higher than any other. The following paragraphs are devoted to discussing the relationship between the balance of these terms and the structure of the jet.

The magnitudes of the these three main along-channel momentum balance terms are shown in Fig. (3.6.1). In the vicinity of $\xi = 0$ (the outlet region) the results are similar for the geometry with sloping and elliptical profiles, while it shows remarkable differences with the simulation with horizontal bed. In the rest of the axis, both in the channel and in the marine zone, the results tend to be similar for all geometries. In the case of the acceleration due to friction (negative

values), it can be observed that its influence is limited to a reduced distance in the vicinity of the outlet for non-horizontal geometries, while it extends up to $\xi = 4.0$ (x=400 m) for the geometry with horizontal bed.

Along the stream axis, there is a balance between friction and hydrostatic pressure accelerations for each geometry, while the acceleration due to inertial forces (momentum transport) is negligible as a consequence of a regular and constant geometry of the channel, corresponding to an uniform flow. In the outlet region, this balance changes and significant accelerations appear, especially those corresponding to the hydrostatic pressure and inertial terms, with relevant differences in magnitude for the geometry with horizontal bottom compared to the geometries with sloping and elliptical profiles. In this area, the perturbation of the flow created by the outlet propagates upstream as the flow is subcritical. In the nearshore, the accelerations tend to decrease to a negligible value. The only exception is the acceleration due to friction for the geometry with horizontal bed, which shows its influence up to $\xi = 4.0$ (x=400 m).

As for the accelerations due to the hydrostatic pressure and the momentum transport, a strong variation of the acceleration is concentrated in a distance around the outlet in the interval $\xi = [-2.0, 1.0]$, especially for geometries with sloping and elliptical profiles. Note that the signs of the accelerations are different. It is also observed that the values of these accelerations for the cases with $h_0 = 1$ m are one order of magnitude higher than those obtained for the simulations with $h_0 = 3$ m. This means that the velocity changes are more pronounced in the first case. Therefore, for the horizontal bed geometries, friction dominates in the nearshore over a longer extent, favouring jet expansion, similar to the friction dominated flows described by Wright (1977). In contrast, for the variable bed level geometries, the barotropic and momentum transport terms dominate the momentum balance near the outlet, contracting the jet. Approximately at $\xi = 1$ the balance between barotropic and momentum transport decays and jet contraction ceases.

**Final remarks**

The simulations with constant river discharge and water level analyzed throughout this chapter showed that the outlet geometry determines the jet structure, with the shallower and wider outlets having two velocity peaks on the sides of the jet instead of a single maximum in the centre. For outlets where the nearshore profile is horizontal, the extent of the ZOFE region increases significantly and the jet expands after leaving the outlet geometry, whereas for non-horizontal geometries the jet initially contracts. In addition, the hydrodynamics at the mouth are clearly friction dominated for this horizontal nearshore geometry. However, for sloping and elliptical profiles, inertial and barotropic accelerations significantly increase their role in the vicinity of the outlet.

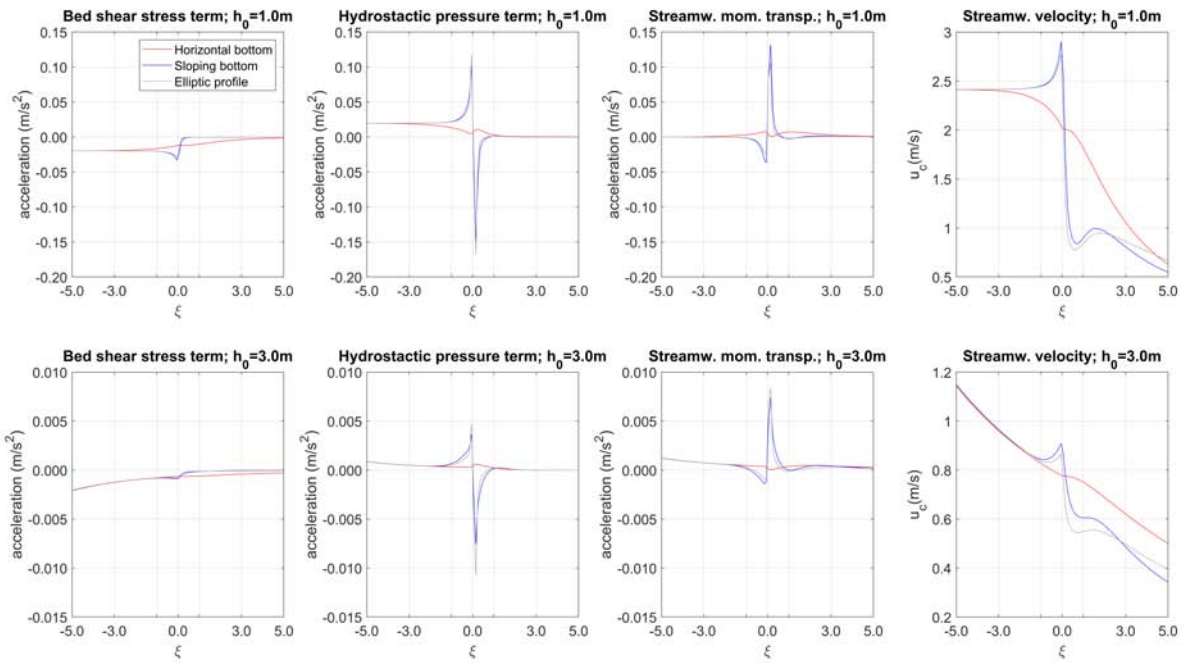


Figure 3.6.1: Results obtained for each of the momentum equation terms for the simulation with constant flow, $W = 200m$ and $h_0 = [1m, 3m]$: acceleration due to streamwise momentum transport, (inertial term) hydrostatic pressure and bed shear in bottom layer. Each line is associated with a geometry type.In the last column, the result for the streamwise velocity along the axis is added for a better understanding.

CHAPTER 4

# RIVER MOUTH HYDRODYNAMICS: HOW TRANSIENT TIDAL AND RIVER DISCHARGE CONDITIONS MODIFY THE JET STRUCTURE

In Chapter 3, the role of the outlet geometry and nearshore profile characteristics on the jet hydrodynamics, including the spreading conditions and the location of the ZOFE and ZOEF transition, was analysed for stationary conditions of river discharge and offshore water levels. The results have enabled the performance of the process-based numerical model and the jet theory to be compared. In this chapter, this analysis is completed for more realistic conditions where both river discharge and sea level vary with time. Specifically, we first analyse the effect of the tide for stationary discharge conditions and then quantify the joint effect of the astronomical tide with river discharge events (pulses). These events are defined by a hydrograph with a reduced time base, whose time scale is of the same order as the astronomical tide, so that the lag between discharge and level emerges as a new parameter controlling the hydrodynamics of the river mouth. The results show that this lag is very important, conditioning the location of the boundary between the ZOFE and ZOEF regions and, in general, the hydrodynamics of the jet. The results of this chapter are presented in Ruiz-Reina and López-Ruiz (2024).

## 4.1 Introduction

As described in the previous chapter, although there is an extensive literature of works analysing the hydrodynamics of the jet debouching onto a continental shelf and how this jet spreads in the nearshore, most of these works have defined simplified outlet geometries using lower channel width to outlet depth ratios (Canestrelli et al., 2014) and channels with no or very gentle slopes flowing into horizontal basins (Edmonds and Slingerland, 2007; Leonardi, Kolker, and Fagherazzi, 2015; Nardin, Edmonds, and Fagherazzi, 2016). Although these simplifications have already been discussed in the previous chapter, there is another major limitation of the studies carried out to date, and that is that most of these studies consider constant river discharge conditions and neglect the effect of astronomical tides, storm surges and waves, although works such as Nardin and Fagherazzi (2012) and Nardin et al. (2013) have analysed the role of waves in the formation and evolution of estuarine bars, concluding that waves play an important role in the

timing of bar evolution as well as in their final geometry. Leonardi, Kolker, and Fagherazzi (2015) focused their interest on the role of tides defining for a very simple geometry with a horizontal bottom cases with constant river discharge (river-dominated) and with oscillating discharge (tidal-dominated) in which the effect of the ebb/flood cycles in the channel is mimicked. The results obtained show that in the river-dominated case the tide has a wave-like dispersive effect, whereas in the tide-dominated case the effect varies considerably depending on the tidal range and river discharge.

This literature review suggests that the interactions between fluvial discharge and marine agents are very complex, although they are crucial for the management of river mouths and deltas. Furthermore, despite all the recent advances described above, there are still important aspects to be analysed in order to describe the jet structure at outlets. In particular, the joint effect of the astronomical tide and what role the time lag between tidal and flow conditions may play in short river discharge events (time scale similar to that of the tide) has to be further explored.

The main objective of this chapter is to analyse the effect of tides and short fluvial discharge pulses on the jet geometry, where their phase difference with the astronomical tide can influence the hydrodynamics of the jet. To achieve this goal, a process-based numerical model is used on idealised but realistic geometries where the channel and platform slopes, as well as the outlet shapes commonly observed in small river mouths with high seasonal variability and relatively high slopes due to their proximity to mountain ranges are maintained. This proximity, which limits the size of the hydrological basins, also causes the fluvial discharge pulses to be short and may have the same time scale as the astronomical tides (Ruiz-Reina et al., 2020; Ruiz-Reina, 2021; Ruiz-Reina and López-Ruiz, 2021).

## 4.2 Numerical experiments

For the numerical experiments, the same Delft3D model setup described in the previous chapter was employed. Hence, three types of open boundaries were defined: (1) the offshore boundary, with water level conditions; (2) the upstream boundary, located in the very upstream part of the channel, with river discharge conditions; and (3) two cross-shore boundaries, where Neumann-type conditions were used, imposing a zero water level gradient in the direction perpendicular to the boundary (Roelvink and Walstra, 2004).

Regarding the experimental setup, since in this chapter we focus on more realistic situations than those for which the jet theory was developed and the numerical modelling has already been validated, physical scenarios in which the continental shelf is horizontal are not considered. In addition, since the effect of the outlet dimensions has already been analysed, the width of the mouth $W$ is limited to 200 m.

In this case two types of simulations were defined depending on the upstream and offshore boundary conditions (Types 1 and 3, as Type 1 was used for the experiments described in Chapter 3). The first type of simulation (Type 2) is used to analyse the effect of the tide and how it modifies the jet structure. In this case, the river discharge conditions described in Chapter 3 are maintained, being defined with a constant discharge rate per unit channel width $q = 2.5$ $m^2/s$. As the analysis is limited to $W = 200$ m, the total discharge is $Q = 500$ $m^3/s$. At the offshore

| Type | Id | Profile | $W$ (m) | $h_0$ (m) | $Q_p$ (m$^3$/s) | Offshore | $\phi$ (rad) |
|---|---|---|---|---|---|---|---|
| 2 | 221-T | Sloping | 200 | 1.0 | 500 (C) | Tide | - |
| | 321-T | Elliptical | | 1.0 | | | |
| | 223-T | Sloping | | 3.0 | | | |
| | 323-T | Elliptical | | 3.0 | | | |
| 3 | 321-HT | Elliptical | 200 | 1.0 | 500 (hyd) | Tide | 0 |
| | 321-ET | | | | | | $\pi/2$ |
| | 321-LT | | | | | | $\pi$ |
| | 321-FT | | | | | | $3\pi/2$ |

Table 4.2.1: Numerical scenarios: main characteristics. For the river discharge conditions, C means constant discharge whereas hyd means variable discharge (hydrograph)

boundary the water level varies with the astronomical forcing defined by a single semi-diurnal harmonic with an amplitude of 1 m.

For the second type of simulation (Type 3), the role of the river discharge pulses in the jet structure is analysed by defining different hydrographs in the upstream boundary, while at the offshore boundary the conditions defined for the second type of simulation are maintained. The hydrographs were defined using the SCS (US Soil Conservation Service) method for the Chow, Maidment, and Mays (1988) shape with a duration of 18 hours, corresponding to one and a half complete tidal cycles, and a peak discharge of $q_p = 2.5$ m$^2$/s. This kind of discharge events are typical for ephemeral streams in limited basins where extreme rainfall events associated to DANAs provoke sudden and short discharge events, as those described in the (Ruiz-Reina and López-Ruiz, 2021) database. Furthermore, according to (Ruiz-Reina and López-Ruiz, 2021), the base time of the hydrographs was the same regardless of the peak discharge value. In addition, to analyse the importance of the phase between the peak discharge at the upstream boundary and the tide at the offshore boundary, the beginning of the hydrograph was defined at 4 different times, corresponding to the peak discharge at high tide, MSL to low tide (ebb tide), low tide and MSL to high tide (flood tide). The combination of such different boundary conditions and physical scenarios results in a total of 26 simulations (Table 4.2). The total duration of each simulation is 48 h, including an initial spin-up interval of 24 h to limit the effects of the prescribed still water initial conditions.

## 4.3 The effect of the tides

In this section, the influence of the tide on the jet velocity profile is analysed using Type 2 simulations, limited to the cases with $W = 200$ m, $Q = 500$ m$^3/s$ and geometries corresponding to the sloping bottom and the elliptical profile (Table 4.2). The horizontal bottom profile was excluded from the analysis because the tidal amplitude is similar to the water depth at the outlet.

Fig. (4.3.1) shows the streamwise velocity contours at different times during the tidal cycle. Similar to the results of the Type 1 simulations, the nearshore geometry plays a minor role in the velocity distribution, with the final jet width being slightly larger for the simulations with an elliptical nearshore profile, as a consequence of the shallower depth. In contrast, $h_0$ is an important factor, with higher $h_0$ values leading to a lower mean exit velocity ($\overline{u_0}$), which

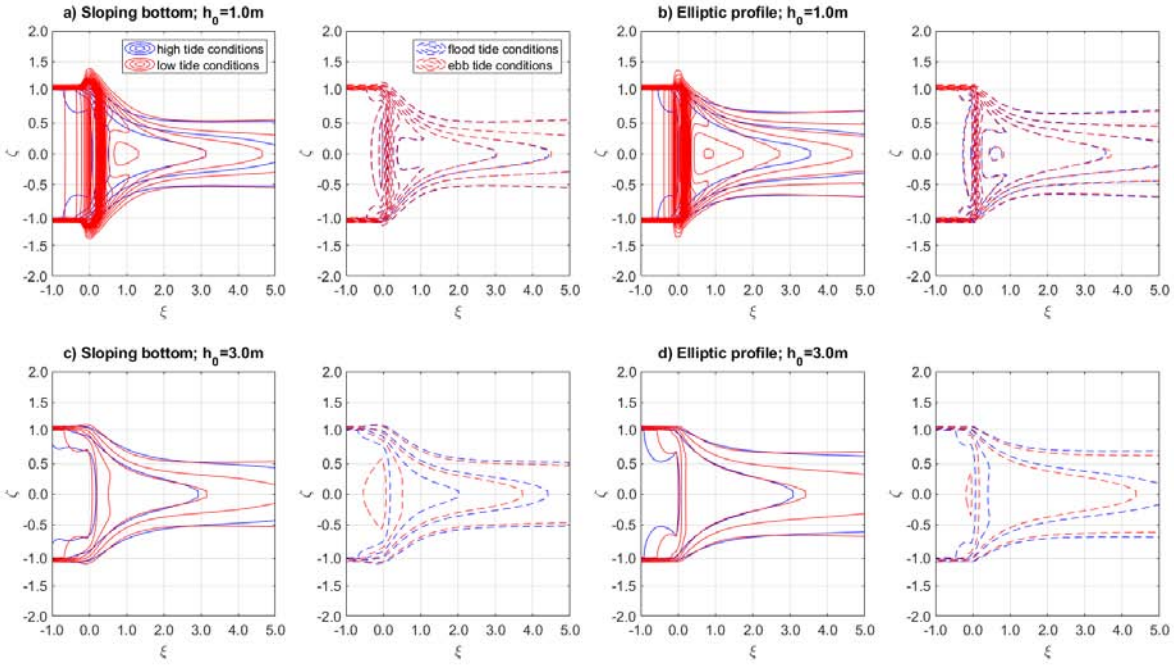


Figure 4.3.1: Velocity isolines with 0.2 m/s intervals and four specific conditions: high, low, ebb and flood tide. Columns 1 and 2 corresponds to the simulations with a sloping bottom, while columns 3 and 4 corresponds to those with an elliptical profile. The first row shows results for geometries with $h_0 = 1$ m and the second one to those geometries with $h_0 = 3$ m.

favours the development of a jet with maximum velocity on the axis and a Gaussian transverse distribution. The tidal conditions emerge as a key factor that plays a significant role in the jet structure at the intratidal scale. Focusing on the simulations with $h_0 = 1$ m, for high tide conditions, maximum velocity values are observed at the mouth along the edges of the jet in sections close to the outlet, although there is a rapid evolution of the jet taking a maximum value along the axis. However, for low tide conditions, the existence of two local maximum velocities for the cross-channel profiles extends over longer distances along the jet path, which means that the development of the jet requires a longer distance, approximately twice as long as for high tide. For ebb and flood conditions, identical velocities are obtained and show a jet structure similar to that for low tide conditions. This means that a jet structure with two peak velocities along the edges is predominant during the tidal cycle for simulations with $h_0 = 1$ m. In contrast, the results for $h_0 = 3$ m show a tendency towards a jet structure with a single peak velocity along the axis for the entire tidal cycle, except for a short area around the mouth for low tide conditions. These results highlight the key role of $h_0$ in the jet structure near the mouth.

Fig. (4.3.2) analyses the time evolution of the flow velocity. This graph depicts the absolute values of the velocity to clearly show the significant differences in values obtained for $h_0 = 1$ m and $h_0 = 3$ m, especially at the outlet. The values obtained for $h_0 = 1$ m peak at 5.0 m/s in sections downstream of the mouth for instants coinciding with low tide conditions, whereas at high tide this maximum velocity decreases to below 1.5 m/s, implying a variation of more than twice the

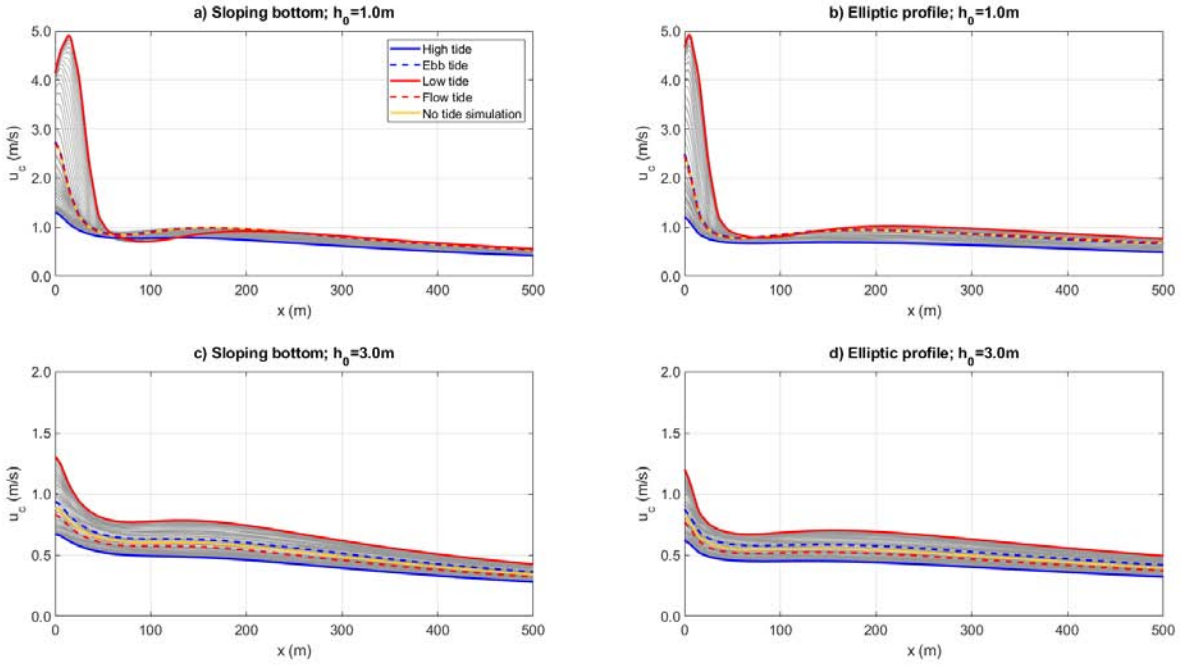


Figure 4.3.2: Time evolution of the absolute velocity profiles as a function of time with intervalos of 10 minutes. A yellow line is added to show the result obtained for cases with constant flow without sea level variation.

minimum value. Furthermore, the section where the maximum velocity is located varies during the tidal cycle, moving downstream as the sea level drops. The velocity profiles are very similar for the two seabed profiles. For $h_0 = 3$ m, lower velocity values and variabilities are obtained with velocities between 0.6 m/s and 1.3 m/s. In addition, the maximum velocity value is located at the mouth, the velocity decrease after the outlet shows a smoother shape and the velocity profiles are parallel to those of the non-tidal case, that are also shown in Fig. (4.3.2).

If the results are non-dimensionalized (Fig. 4.3.3), all the velocity profiles for both nearshore profiles show: i) a sharp decrease at a distance less than $\xi = 1$; ii) increase in velocity and maximum value located in a section at a distance $\xi$ =1.5-2.0; and iii) a velocity decrease with decreasing ratio. Furthermore, there is a significant variation of the velocity with the tidal phase. For the cases with $h_0 = 1$ m, the maximum difference observed is $u_c/u_0 = 0.4$ at $\xi = 1.2$, which implies a variation of more than 100%. This difference decreases further away from the mouth but maintains a value around $u_c/u_0 = 0.1$ at $\xi > 5$. On the other hand, for simulations with $h_0 = 3$ m, the trends are similar but the differences are smaller. In this case, the maximum difference is $u_c/u_0 = 0.15$ at $\xi > 0.7$, which remains practically constant along the jet. These results show that the tide has an outstanding influence on the jet structure, with differences in $u_c/u_0$ above 100%. These differences, and hence the role of the tide, are clearly intensified for shallow river mouths.

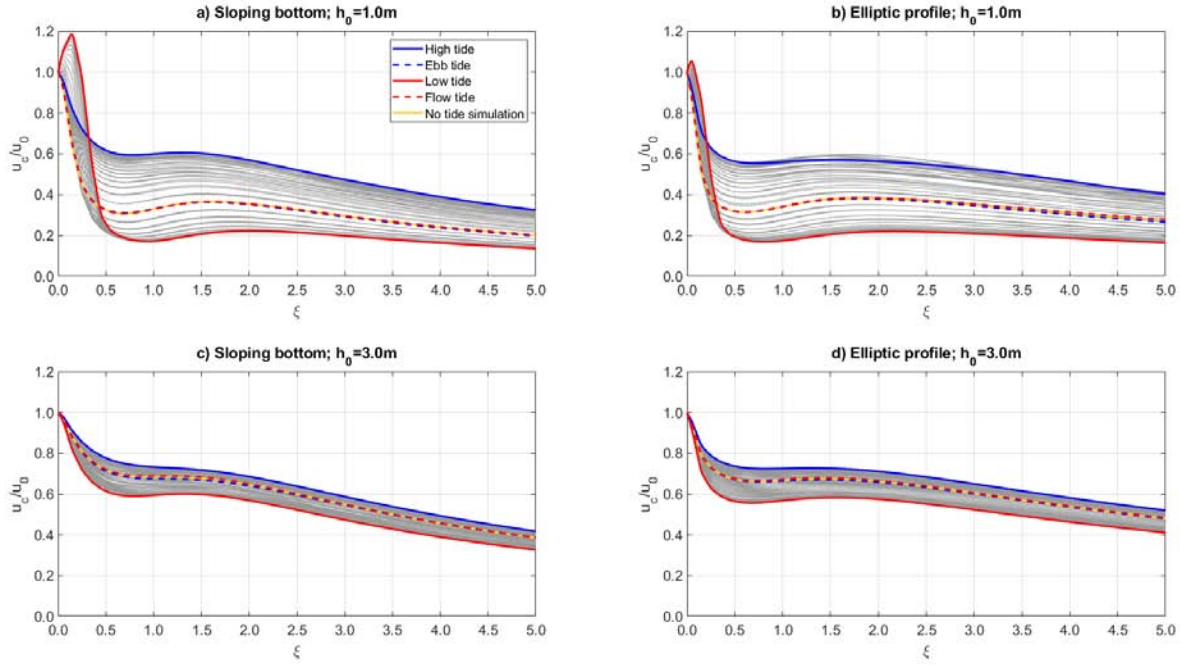


Figure 4.3.3: Dimensionless time evolution of the velocity profiles. Yellow line corresponds to the result with constant flow without sea level variation.

## 4.4 Transient river discharge: the role of the phase lag between the hydrograph and the tidal conditions

In this section, the results of type 3 simulations (Table 4.2), where the geometry is restricted to the elliptical profile with $h_0 = 1$ m and $W = 200$ m, are analysed. A hydrograph with a base time of 18h and a peak discharge of 500 $m^3/s$ is defined as the upstream boundary condition. Tidal conditions are maintained at the offshore boundary. These forcings introduce a new variable into the analysis of the jet structure: the time lag between the instant of peak flow and high tide at the offshore boundary $\phi$ (Fig. 4.4.1).This delay is measured in terms of the phase of the tidal cycle. The analysis of the results show that the time that takes to the tidal wave to propagate from the offshore boundary towards the outlet is negligible.

The plan view structure of the jet during the peak discharge for the different values of $\phi$ is shown in Fig. (4.4.2). For $\phi = 0$, the jet contracts and shows a single peak velocity on the axis close to the mouth. Thus, the velocity profile quickly evolves to a transverse distribution with a single peak velocity on the axis. In contrast, for $\phi = \pi$, two maximum velocity peaks are clearly visible at the edges of the jet up to a distance of more than 100 m ($\xi = 0.5$). Beyond this distance the velocity profile evolves to a single maximum on the axis.

These results are consistent with those shown in the previous section. High water levels lead to velocity profiles with a single maximum value in the centre, while low water levels lead to velocity profiles with two maximum values at the edges, over a length of the order of $\xi = 1.0$. The high water conditions imply a greater water depth at the mouth ($\eta_0$) and therefore lower mean

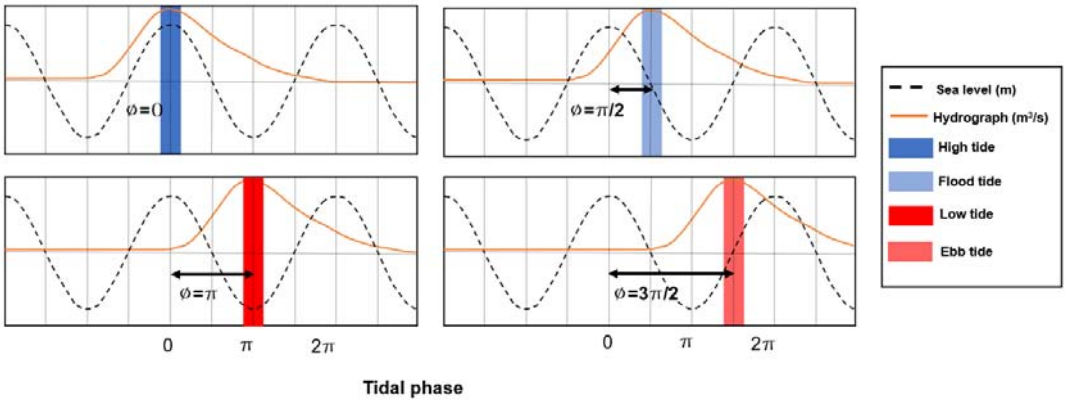


Figure 4.4.1: Definition sketch of the phase difference between the peak river discharge and the tidal level for the analyszed simulations.

velocities at the outlet ($\overline{u_0}$), as was the case for the simulations with $h_0 = 3$ m.

Fig. (4.4.3) highlights the large variation in the velocity values at the outlet for the four cases analysed, with a range that oscillates between 0 and 3 m/s for $\phi = 0$ and between 0 and 5 m/s for $\phi = \pi$. This shows that when the hydrograph coincides with the high tide, the value of the depth at the outlet ($\eta_0$) is higher, leading to a lower value of the outlet velocity ($u_0$), resulting in velocity profiles similar to those of the jet theory, with a single maximum value at the jet axis. On the other hand, when the peak of the river discharge coincides with low tide conditions, it implies a lower depth ($\eta_0$), higher velocity at the outlet ($u_0$) and velocity profiles with two peaks at the jet edges. It is also relevant that the maximum value of the velocity is not located at the mouth in every profile, but is slightly shifted towards the coast for $\phi = \pi$, especially during low tide conditions.

The flow velocity along the axis shows a significant variability during the tidal cycle. For low discharges, corresponding to the ascending and descending limbs of the hydrograph, the velocity shows a moderate value at the outlet and a slight decrease along the profile until it reaches an almost constant value close to 0.3 m/s at x =100 m ($\xi = 0.5$). For discharges close to the peak value of 500 $m^3/s$, there is a maximum velocity in the area of the outlet followed by a sharp decrease in the first 50 m ($\xi = 0.5$). This profile with a relative minimum and maximum is more clear for $\phi = \pi$. This behaviour is similar to that described in the previous section for constant discharge. On the other hand, it can be observed the lower inertial force of the simulated cases with hydrograph and peak flow compared to those with constant flow over time (yellow line).

To make the comparison with previous results easier, Fig. (4.4.4) shows the dimensionless velocity profile along the axis. A significant variation is observed between them depending on the tidal conditions. The profiles associated with low tide ($\phi = \pi$) are more similar to those with constant river discharge (Fig. 4.4.1), as they are associated with a higher velocity at the mouth.The use of dimensionless velocities shows new velocity trends, especially for $\phi = \pi$. There is also the presence of a second relative maximum at $\xi = 20 - 30$, associated with the advance of the river discharge.

This important variation in the shape of the streamwise velocity profiles is also transferred

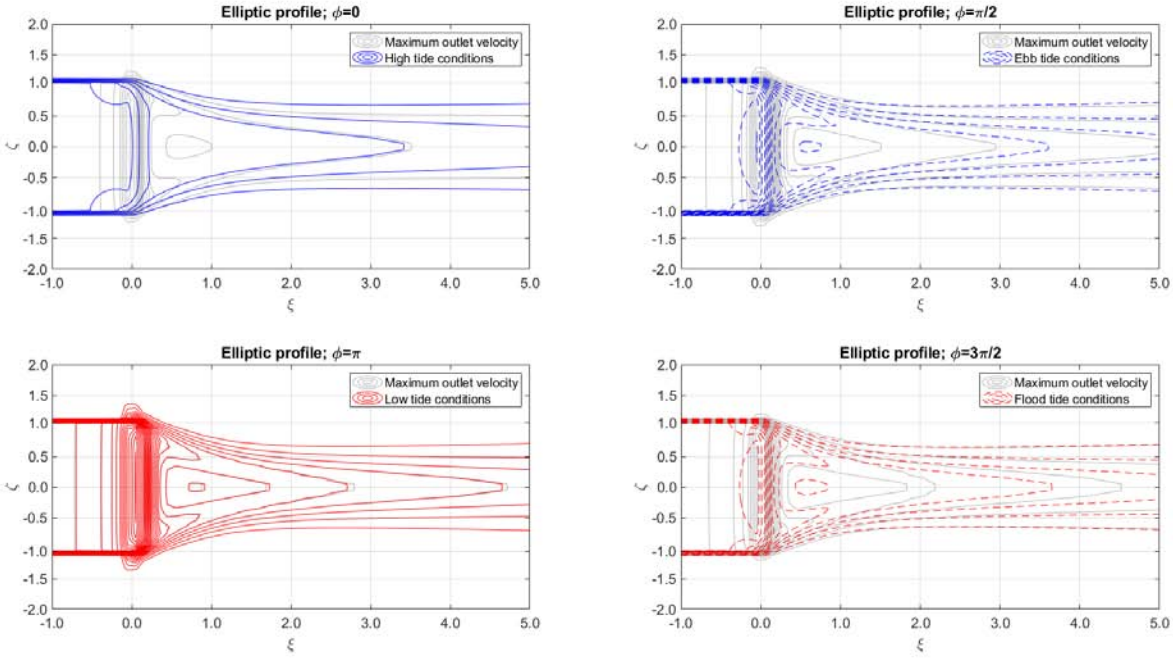


Figure 4.4.2: Velocity isolines for $W = 200$ m, $h_0 = 1$ m, elliptical profile, and $\phi = [0, \pi/2, \pi, 3\pi/2]$ (coincidence between peak flow and high tide, low tide, ebb tide and flood tide conditions, respectively). Coloured lines represent the results for the maximum discharge instant, while the grey lines represent the maximum velocities obtained for each simulation, associated to a different instant.

to their cross-sectional distribution (Fig. 4.4.5). Velocity profiles with Gaussian distribution are observed for instants corresponding to high tide, regardless the value of $\phi$, whereas two velocity peaks are observed at low tide. On the other hand, there are significant differences between the velocity profiles corresponding to the simulations with hydrograph and tide compared to those with constant discharge and still water. The latter show a profile with two maximum velocity values, around 1.0 m/s. For the simulations with $\phi = 0$, all the profiles show velocity values lower than this value and none of them coincide with the case of constant discharge and still water. As for the simulations with $\phi = \pi$, the simulations with hydrograph and tide show greater similarity with those corresponding to constant discharge and still water, although a transverse distribution with more pronounced peak velocity values is observed.

## 4.5 Time-varying location of the transition between ZOFE and ZOEF regions

Jet theory describes the Zone of Flow Establishment (ZOFE) as the part of the jet where the transverse velocity remains constant until momentum dissipation and turbulence generated by edge shear reaches the entire jet (Fagherazzi et al., 2015). From this point on, the jet is dominated by turbulent eddies (Zone of Established Flow, ZOEF) and leads to a similar Gaussian transverse velocity distribution. Although this structure is observed for some of the numerical experiments

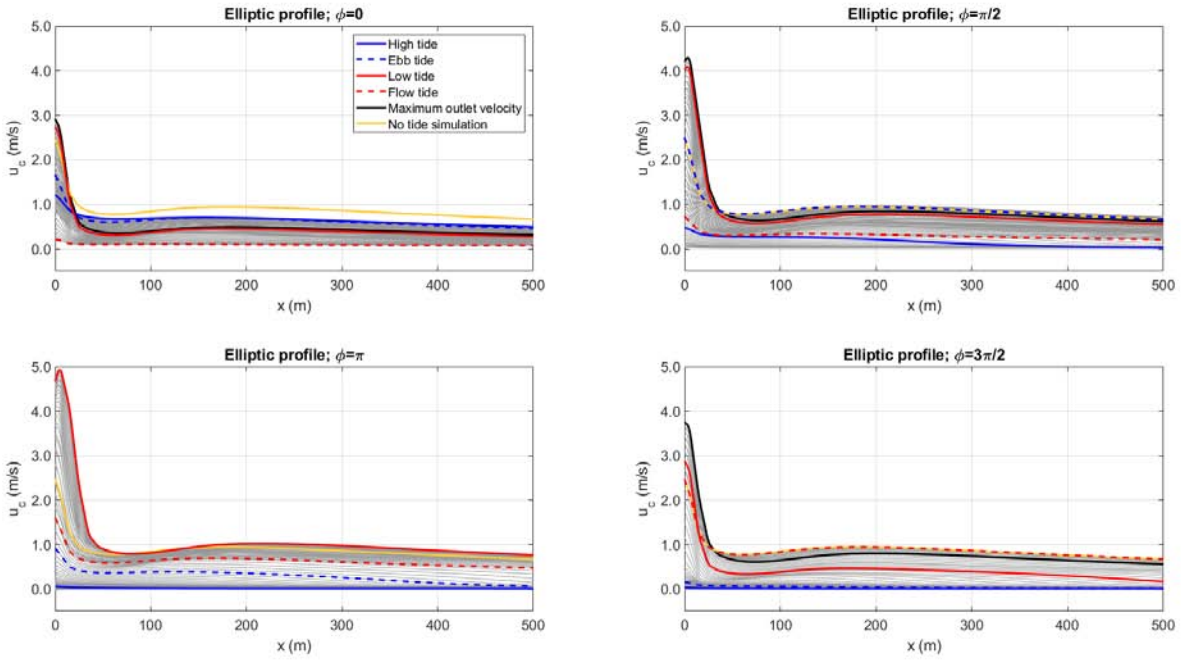


Figure 4.4.3: Velocity along the axis during the entire tidal cycle for the simulations considered ($\phi = [0, \pi/2, \pi, 3\pi/2]$; $W = 200m$; $h_0 = 1m$), analogous to Fig. 4.4.2 in the previous section. Note that these are absolute values of velocity.

performed, the results show that depending on the outlet and nearshore geometries, a different jet structure can develop, in which two velocity peaks are observed at the edge of the jet near the mouth. These two velocity peaks at the edges progress transversely towards the centre until they reach the axis, and from that point on the Gaussian profile is observed, as shown in Fig. (4.5.1). Therefore, the establishment of the flow is beyond this point of maximum velocity where the two peaks at the sides oof the jet converge. In addition, these differences in the behaviour of the velocity distribution in the jet are accentuated for mouths with a greater width ($W$), a shallower depth at the outlet ($h_0$) and a sea profile different from a horizontal plane. In all these cases, the location of the relative maximum velocity along the axis was found between $\xi = 1.5 - 2.5$. In the cases with tides as the offshore boundary condition, and even when the river discharge is not constant, analogous results are observed. In these cases, depending on the tidal conditions, the velocity profile corresponds to the first group, with a single peak at the axis (related to high tide), or to the second group, with two peaks at the jet edges (related to low tide).

It is therefore clear that different mouth geometries and hydrodynamic forcings lead to different jet velocity structures and turbulence progression from the edges to the jet axis, as well as the location of the transition between the ZOEF and ZOFE regions. The location of the beginning of the ZOEF region was determined from a comparison between dimensionless simulated streamwise velocity at every cross section and the jet theory in the ZOEF region, ensuring that the difference between them in the interval $\zeta = [-1, 1]$ does not exceed 5%. Fig. (4.5.2) shows the results for the location of the transition zone between ZOFE and ZOEF for the

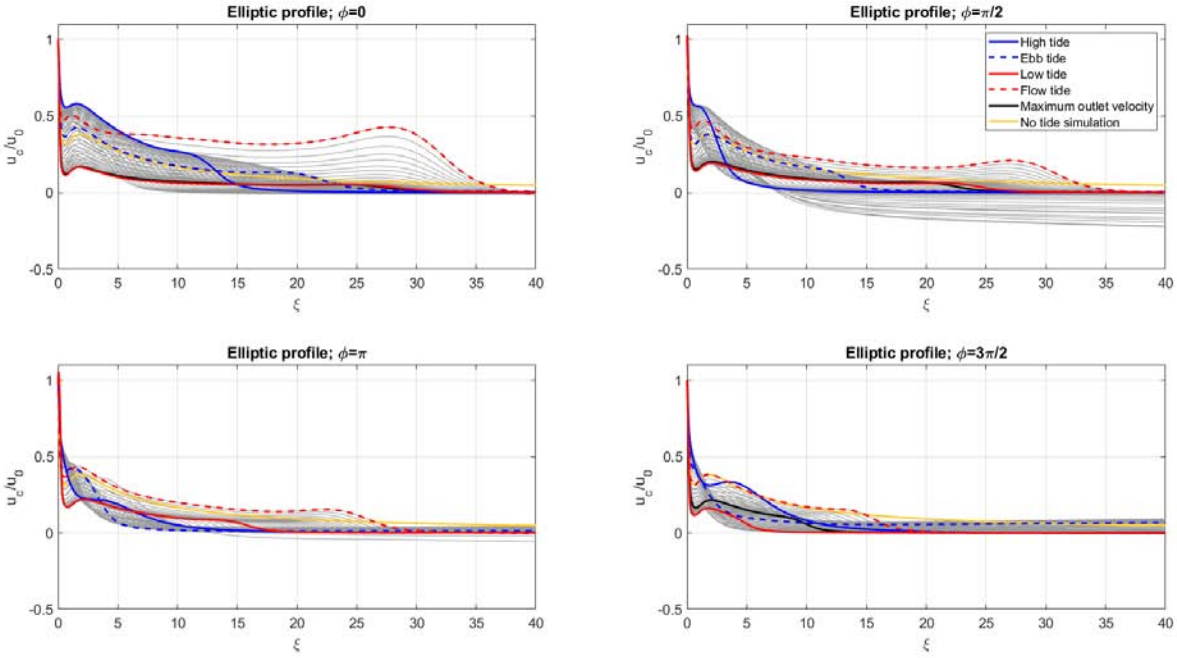


Figure 4.4.4: Dimensionless velocity along the axis during the entire tidal cycle ($\phi$ = $[0, \pi/2, \pi, 3\pi/2]$; $W = 200m$; $h_0 = 1m$). Omitted cases with $u_0 < 0.3$ m/s.

three types of simulations tested. For constant river discharge, still water and horizontal bed profiles (Fig. 4.5.2a) the results do not show a clear trend. As summarised in Fagherazzi et al. (2015), previous works state that for a plane unbounded jet this transition occurs at a distance $\xi = [4.0 - 6.0]$. In addition, Rowland, Dietrich, and Stacey (2010) reported higher values for their experiments ($\xi = [16 - 18]$), but they argued that these results might be related to their particular experimental setup with a pair of levees providing partial confinement. Therefore, the results presented in this paper are consistent with the literature not showing clear trends for the location of the ZOFE/ZOEF transition. The analysed geometries have a very high $W/h_0$ ratio, with a velocity profile influenced by the upstream section of the channel, which significantly affects the jet structure and modifies the initial conditions of other studies.

However, for sloping bottom geometries and elliptical profiles (i.e. increasing bottom depth along the axis) a similar behaviour and tendency is observed. The wider outlets result in a further location of the ZOEF region in the range $\xi = [1.0 - 4.0]$. For the simulations with an elliptical profile, slightly higher distances are observed compared with those of a sloping bottom. These distances are significantly lower than those given for planar unbounded jets.

Fig. (4.5.2c) shows the results obtained for each time point during the tidal cycle for all simulations with constant river discharge. The parameter $h_0$ has a significant influence: for $h_0 = 3$ m, the ZOEF region remains at the same distance throughout the tidal cycle, although for $h_0 = 1$ m, at low tide conditions, this distance is greater, especially for the elliptical profile simulations. The location of the transition is in the interval $\xi = [1.5 - 3.0]$. The results for simulations with tides and transient river discharge (Fig. 4.5.2d) show that at low tide conditions,

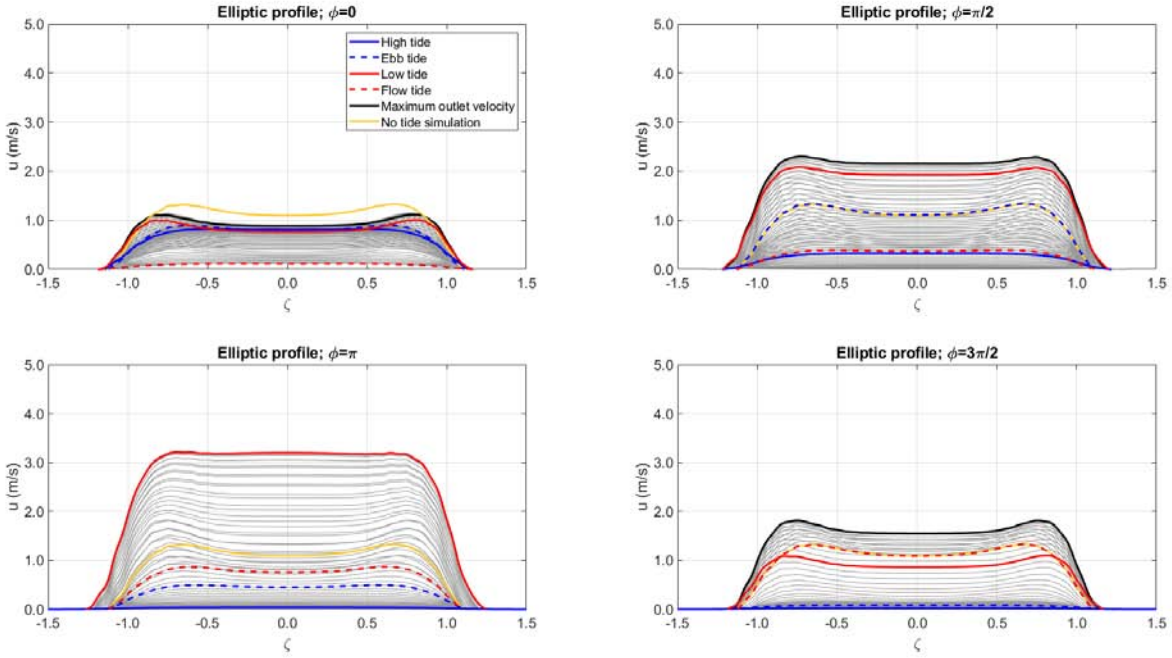


Figure 4.4.5: Cross-sectional distribution of velocities at 100 m from the outlet ($\xi = 0.5$), located in the ZOFE region. Yellow line is added showing the result for the same geometry, corresponding to the simulation with constant discharge and still water. Black line corresponds to transverse velocity profile at the instant of maximum velocity at the outlet.

the distance from the mouth where the ZOEF region is located increases. This is more evident in the simulation with $\phi = \pi/2$ as this low tide coincides with the peak of the hydrograph. In the case of $\phi = 0$, two instants are observed in which the ZOEF region is located at a greater distance: the first corresponds to the peak of the hydrograph and the second to the low tide. As in the previous group of simulations, the distance for the beginning of the ZOEF region is within the interval $\xi = [1.5 - 4.0]$.

Therefore, the location of the transition between the ZOFE and ZOEF regions with non-horizontal geometries is at a shorter distance from the mouth than in the cases with horizontal bottom. The decreasing mouth width and increasing bottom slope in the nearshore area lead to shorter distances for the location of this transition, whereas a shallower outlet depth ($\eta_0$) contributes to increasing this distance during a tidal cycle, i.e. showing a maximum value during low tide conditions. Furthermore, this transition an hence the jet structure varies significantly during the tidal cycle regardless the outlet geometry.

## 4.6 Jet structure and the development of lateral levees

The jet structure plays an important role in the morphodynamic evolution of river mouths and the development of bars, both at short-term and long-term (Jiménez-Robles, Ortega-Sánchez, and Losada, 2016) scales. The changes in the initial bed geometry would, in a feedback process,

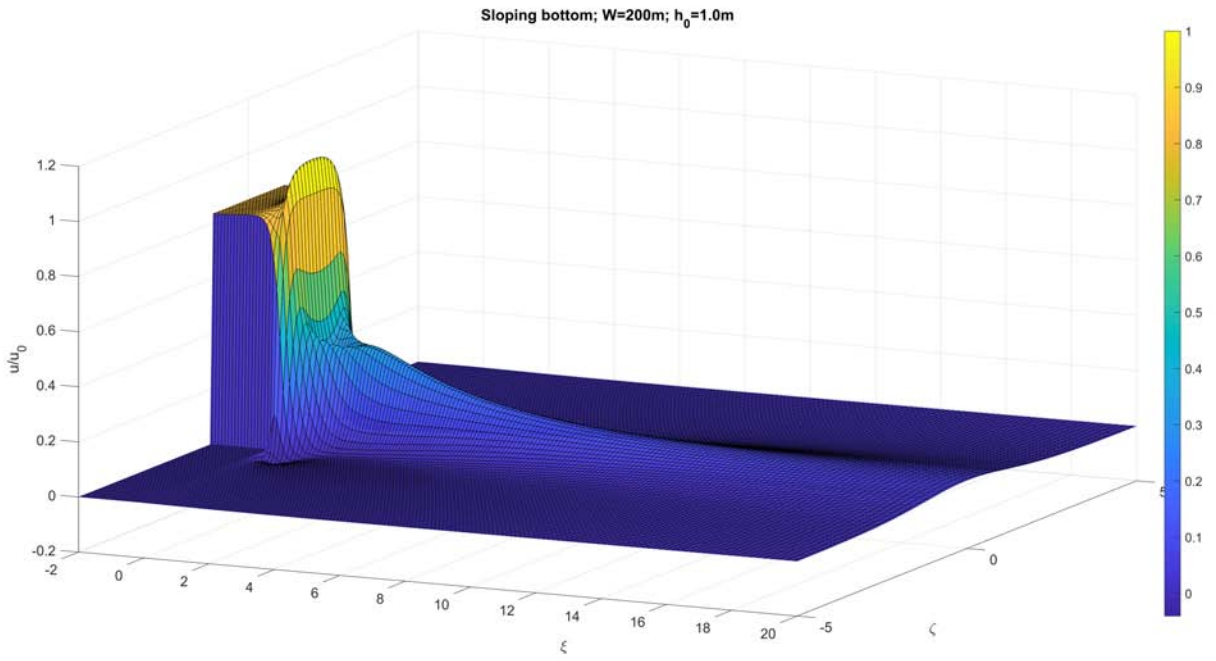


Figure 4.5.1: 3D view of the velocity distribution for the case of constant flow, W=200m, $h_0 = 1$ m, and sloping bottom profile.X-axis and Y-axis are dimensionless distances related to the mouth half-width ($b_0$).

modify the jet structure and, consequently, the hydrodynamics of the river mouth. However, the results presented in this work provide some insights that can be used to establish relationships with morphodynamic analyses.

For example, a clear influence of the width of the mouth on the transverse profile of the flow velocity was observed, favouring the formation of two peaks of maximum velocity at the edges. This phenomenon is more pronounced in cases where the bottom depth at the mouth is shallower ($h_0 = 1$ m in the previous simulations). Both Ruiz-Reina and López-Ruiz (2021) and Jiménez-Robles, Ortega-Sánchez, and Losada (2016) observed the formation of lateral levees parallel to the channel walls for river mouths with channel widths similar to those considered in this study. This morphodynamic evolution implies a lower bottom depth up to a certain point of the bar, from which a pronounced slope is formed where the levees do not develop. The bottom depth in these points, in the case of (Ruiz-Reina and López-Ruiz, 2021), reaches values below 2.0 m. On the other hand, the levees are more clearly shown in those simulations where the peak of the hydrograph coincides with the low tide, which implies a higher value of the velocity at the mouth $u_0$, in agreement with the results obtained in the present work.

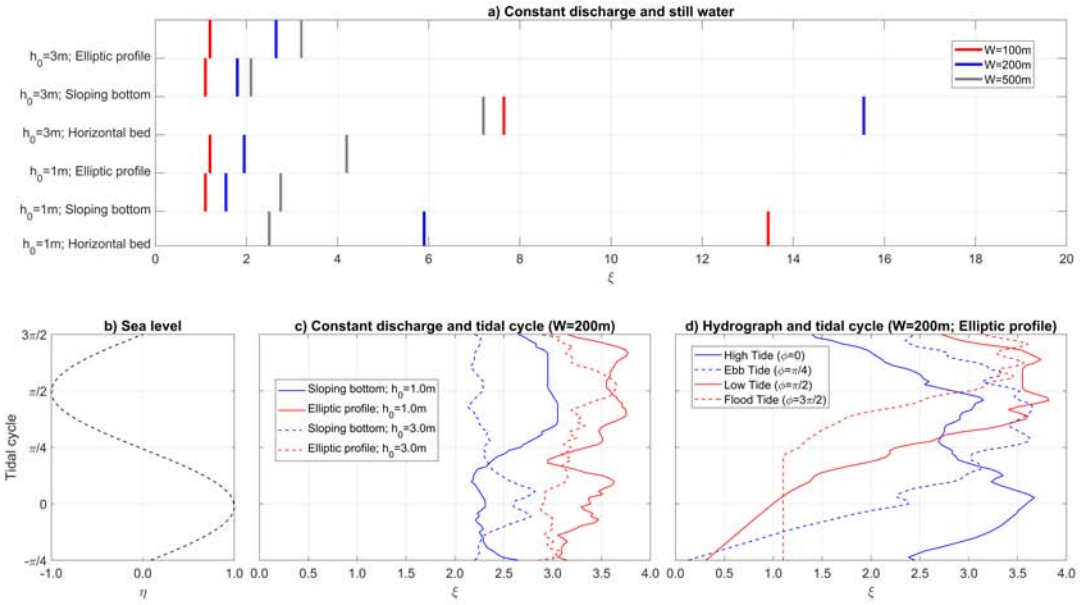


Figure 4.5.2: Analysis of the location of the transition of the ZOFE and ZOEF regions. a) Results for simulations with constant flow and still water. b) Results for simulations with W=200 m and a constant discharge during a tidal cycle, for geometries with sloping bottom and elliptical profile and $h_0 = [1m, 3m]$. c) Results for simulations with $W = 200$ m, $h_0 = 1$ m, elliptical profile during a tidal cycle and $\phi = [0, \pi/4, \pi/2, 3\pi/2]$.

**Final remarks**

For the tidal simulations, it is observed that the changes in velocity during the tidal cycle are up to 100%, while when transient river discharges are also included, the variability of the jet structure during the tidal cycle is very important, limiting the applicability of the analyses carried out for stationary conditions in tidal environments or with a variable hydrological regime. This variability causes the position of the boundary between the ZOFE and ZOEF regions to vary greatly (up to 100%) depending on the time lag between the peak of the hydrograph and the tidal conditions.

Furthermore, this phase and the time along the tidal cycle also determine the geometry of the transverse velocity profile. During low tide conditions, the extent of the ZOFE region increases and the velocity profile tends towards a profile with two lateral velocity peaks. During high tide conditions, a shorter extension of the ZOFE region and a velocity profile with a single maximum on the axis is observed. This is consistent with the literature analysing bar formation in equivalent estuaries. The results obtained in this work, which improve the understanding of the jet structure in river mouths, allow to gain insight into the complexity of the river-ocean interaction during extreme events and its effects on the morphodynamic evolution of river mouth bars and deltas.

CHAPTER 5

# SHORT-TERM RIVER MOUTH BAR DEVELOPMENT DURING EXTREME RIVER DISCHARGE EVENTS: THE ROLE OF THE PHASE DIFFERENCE BETWEEN THE PEAK DISCHARGE AND THE TIDAL LEVEL

The results obtained in the previous chapter show that for basins where extreme river discharge events have a time scale similar to that of the tidal period, the time lag between the peak of the hydrograph and the tidal level plays a very important role in jet hydrodynamics. The potential of this variability in jet hydrodynamics to determine the morphodynamic evolution of river mouths during extreme flood events has also been discussed. To analyse this morphodynamic evolution, this chapter addresses the role of the phase difference between the peak discharge and the tidal level on the development of nearshore bars at river mouths during extreme river discharge events. In this occasion, the hydrodynamic and morphodynamic modules of the Delft3D model are coupled to reproduce extreme river discharge events on an idealized river mouth debouching on a nearshore shelf, characterized by a elliptical cross-shore profile. Different peak river discharges and lags between the peak discharge at the upstream boundary and the high tide at the offshore boundary are tested. The analysis of the water levels, currents, bed shear stresses, sediment transport rates and bed level changes shows that the lag between tidal conditions and river discharge triggers significant changes in (1) the instant in which the maximum currents at the outlet are reached, (2) the period for which the sediment is mobilized trough the outlet, and (3) the maximum sediment transport rates during the events. These changes significantly modify the final characteristics of the river mouth bars, doubling their final extension and quadrupling the final bar volume for the same river discharge conditions and different phase lag, varying also their plan shape and the development of lateral subaqueous levees. These results emphasize the complex interplay between river and coastal hydrodynamics, being of major interest for researchers and managers dealing with projections of the consequences of coastal extreme events and plans to mitigate their effects. This chapter is based on Ruiz-Reina and López-Ruiz (2021).

## 5.1 Introduction

River mouths constitute the transition between rivers and oceans, where tides and waves combine and interact with river discharges transporting most of the sediment eroded on the continents to the oceans (Nienhuis et al., 2016) and forming deltas and depositional river mouth bars (Preoteasa et al., 2016; Jiménez-Robles and Ortega-Sánchez, 2018), resulting in one of the most dynamic environments on Earth (Dalrymple and Choi, 2007). The mixing of fresh and salt water, along with the presence of a high concentration of sediment and nutrients, makes these systems host complex ecosystems (Massuanganhe, Westerberg, and Risberg, 2018) that often struggle to survive in areas that are usually densely populated (Ericson et al., 2006) and host also extensive industrial areas and agricultural lands (Syvitski and Saito, 2007). Hence, understanding the mechanisms that govern deltaic and depositional bar formation and evolution is fundamental for their optimum management (Jiménez-Robles, Ortega-Sánchez, and Losada, 2016).

In recent years a significant number of researchers have focused their attention on the morphodynamics of deltas and river mouths using different approaches, ranging from theoretical (Lamb et al., 2012) and experimental studies (Rowland, Dietrich, and Stacey, 2010) to analyses with numerical models (Jiménez-Robles, Ortega-Sánchez, and Losada, 2016; Nienhuis et al., 2016; Li, Storms, and Walstra, 2018; Gao et al., 2018; López-Ruiz, Garel, and Ferreira, 2020) and field observations (Esposito, Georgiou, and Kolker, 2013). The results of these works improved our knowledge about how bar systems are formed and evolve in river mouths and the importance of the sediment size (Edmonds and Slingerland, 2007), the deposition from sediment-laden flows for the levee formation (Rowland, Dietrich, and Stacey, 2010), the wind waves (Nardin and Fagherazzi, 2012; Nardin et al., 2013; Anthony, 2015; Gao et al., 2018), the human activities (Anthony, Marriner, and Morhange, 2014; Fan et al., 2006; Besset, Anthony, and Bouchette, 2019), the frictional effects (Canestrelli et al., 2014), the nearshore bottom slope (Jiménez-Robles, Ortega-Sánchez, and Losada, 2016), the alongshore sediment bypassing (Nienhuis et al., 2016), the river-shoreline alignment (Jiménez-Robles and Ortega-Sánchez, 2018) or the presence of vegetation (Nardin, Edmonds, and Fagherazzi, 2016; Lera et al., 2019).

Nevertheless, this analysis of the literature reveals that previous research has been focused on the mid- to long-term morphodynamics of bar development, considering steady or quasi-steady river discharge conditions and subtidal processes. However, short-term river mouth morphodynamics during extreme events has received much less attention by researchers, despite its analysis is essential for further understanding the complex dynamics (Del-Rosal-Salido et al., 2019; Del-Rosal-Salido et al., 2021; Leijnse et al., 2021) involving sediment deposition and river mouth bar development (Giosan et al., 2005; Maillet et al., 2006). This is of particular interest in some areas, such as the Mediterranean coasts (Brocchini et al., 2017; Melito et al., 2020), where extreme events frequently occur (Martín-Vide et al., 1999; Dayan, Nissen, and Ulbrich, 2015). These events are characterized by sudden and abrupt freshwater discharges occurring immediately after a rainfall event, lasting from hours to few days, and usually involving important financial and social costs (Liquete et al., 2005; Llasat et al., 2010). Such discharges are common for rivers with relatively small catchment areas (Liste, Grifoll, and Monbaliu, 2014), being controlled by very complex factors that mainly include characteristics of the rain and physical and hydrological properties of the watershed (Rozalis et al., 2010).

Although the effect of tides has been recognized as an important factor controlling both

the hydrodynamics of the jet stream leaving the river mouths and the morphology of their sedimentary deposits (D'Alpaos et al., 2010; Lamb et al., 2012; Leonardi, Kolker, and Fagherazzi, 2015; Cao et al., 2020), there are still some aspects of the interaction between tidal hydrodynamics and river flow that deserve further investigation. In particular, the effect of the time lag between the tide and the maximum river discharge has not been studied in depth, despite its significant importance in extreme river flood events, as the time scales of both the main tidal constituent (diurnal or semidiurnal) and the hydrograph are similar. In this regard, although the idea that the greatest morphodynamic effects occur when the peak river discharge is synchronous with tidal ebb conditions may seem intuitive, it is important to quantify the differences for different lags between river discharge and tidal conditions in order to analyze the importance of these tidal effects and to what extent they can be neglected, as is often done.

The main objective of this Chapter is the analysis of the intratidal effects of the phase difference between the peak discharge and the tidal levels on the development and final characteristics of the river mouth bars created after extreme river flood events. The methodology is based on the numerical modeling of these events in an idealized river mouth, also analyzing the influence of different peak discharge values. In the analysis, only the ocean tides and the river discharge are considered to isolate the effects of their interactions and facilitate the interpretation of the results, that can be used as the basis to later works that could include other forcings such as storm surges and wind waves. The discussion and conclusions described in this manuscript are of interest not only to researchers, but also to engineers and managers responsible for developing both projections of the consequences of these extreme events at river mouths and plans for mitigating their effects.

## 5.2 Physical scenario

The physical scenario in which the numerical model was implemented (Fig. 5.2.1) is very similar to those used in previous chapters, consisting on a single domain representing the nearshore and continental shelf receiving the river. For the definition of the scenario, we used averaged data extracted after the analysis of a 16-stream database of seasonal and ephemeral rivers in the Mediterranean coast of Southern Spain (Ruiz-Reina, 2021), where extreme river discharge events have been observed (Liquete et al., 2005). According to this database, that assures the link between the numerical setup and the real world, a non-cohesive sediment with mean grain size of 1 mm was considered both for the river and coastal domains. This type of sediment is usually found in rivers with relatively small catchment areas where these extreme events occur.

The river geometry was defined as a straight, shore-normal channel with a width of $W = 200$ m and a stream slope of $S_s = 0.002$. The cross section of the channel is rectangular with 5 m height vertical banks. This geometry aims to avoid the overflowing of the lateral banks and hence the inundation of the emerged land at the sides of the stream, thus neglecting the effects of the topography in the analysis and assuring that all the water from the river discharge reaches the river mouth. The bed level at the outlet is $h_0 = 1$ m below the mean sea level (MSL hereinafter), as a representative value obtained from the revision of the database (Ruiz-Reina, 2021). The river channel was defined with a length of 2.5 km to: (1) avoid the numerical effects of the upstream boundary condition on the stretch of the channel coinciding with the tidal excursion; and (2) capture the complete interaction between the river discharge and the tides.

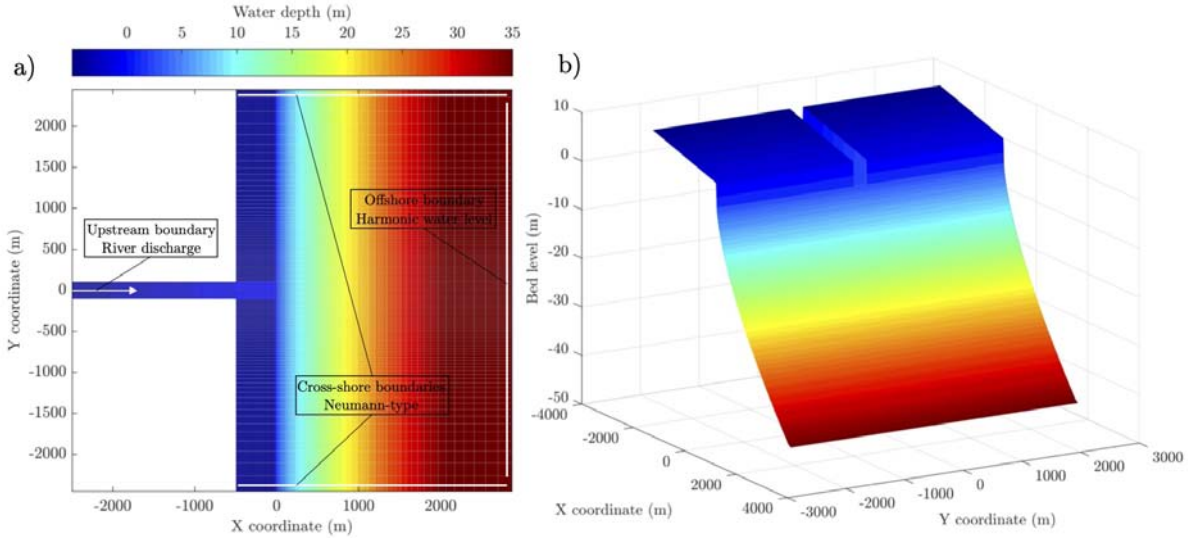


Figure 5.2.1: Physical scenario: a) Plan view of the domain and boundary conditions used; and b) 3D plot including the bathymetry and the river channel.

The shoreline is straight and the cross-shore profiles of the bathymetry were simplified with the elliptical equilibrium profile defined in Chapters 3 and 4 (Dean and Dalrymple, 2004):

$$h = Ax^{2/3} \tag{5.1}$$

where $h$ is the bed level respect to the mean sea level (MSL), $x$ the cross-shore distance measured from the shoreline and $A$ is the profile scale factor which is a dimensional parameter and is a function of the energy dissipation and indirectly the grain size of the beach (Dean and Dalrymple, 2004). In this case, $A = 0.210$ m$^{1/3}$ was adopted according to the sediment size. The curve described by Eq. (5.1) is concave upwards and thus similar to profiles found in nature. This nearshore profile was defined up to 10 m depth, value above the maximum depth that the river mouth bars reached after the numerical experiments. For depths over 10 m the profile has a constant slope equal to the slope of Eq. (5.1) at $h = 10$ m. The offshore boundary of the bathymetry was extended to approximately 43 m depth, 3 km away from the shoreline assuring that the numerical implementation of the offshore boundary conditions did not influence the obtained results.

## 5.3 Numerical model: morphodynamics

Considering the objectives set for this chapter, both sediment transport and bathymetry updating to model the morphodynamic evolution were also activated within the flow module of the Delft3D model, whose hydrodynamic equations have already been described in chapter 2. Bed load and suspended sediment transport for non-cohesive sediments are computed separately with the model. The empirical transport formula proposed by Rijn (1984a) was used for the bed load:

$$S_b = A\sqrt{\Delta g D_{50}^3} D_*^{-0.3} T^B \tag{5.2}$$

with $A = 0.053$ and $B = 2.1$ for $T < 3.0$ and $A = 0.1$ and $B = 1.5$ for $T \geq 3.0$. In this latter equation, $\Delta = (\rho_s - \rho_w)/\rho_w$ is the submerged specific gravity of a sediment with density $\rho_s$, median diameter $D_{50}$ and nondimensional particle diameter:

$$D_* = D_{50}\left(\frac{\Delta g}{\nu^2}\right)^{1/3} \tag{5.3}$$

being $\nu$ the kinematic viscosity of water. The nondimensional bed shear parameter $T$ is defined as:

$$T = \frac{\mu_c \tau_b - \tau_{b,cr}}{\tau_{b,cr}} \tag{5.4}$$

with $\mu_c \tau_b$ being the effective shear stress related with the grain friction and $\tau_{b,cr}$ the Shield critical bed shear stress:

$$\tau_{b,cr} = (\rho_s - \rho_w) g D_{50} \theta_{cr} \tag{5.5}$$

where the threshold parameter $\theta_{cr}$ is calculated according to the Shields curve as a function of the non-dimensional grain size $D_*$ (Eq. 5.3) following Rijn (1993). For the sediment used in the numerical simulations $\tau_{b,cr} \simeq 0.5$ N/m$^2$. The model incorporates the bottom slope effects by adjusting these expressions (Jiménez-Robles, Ortega-Sánchez, and Losada, 2016).

For the suspended sediment transport, both the approach of Rijn (1984b) and the advection-diffusion equation were used. This equation reads:

$$\frac{\partial hc}{\partial c} + \frac{\partial huc}{\partial x} + \frac{\partial hvc}{\partial y} = h\left[\frac{\partial}{\partial x}\left(\epsilon_s \frac{\partial c}{\partial x}\right) + \frac{\partial}{\partial y}\left(\epsilon_s \frac{\partial c}{\partial y}\right)\right] + hS \tag{5.6}$$

where $c$ is sediment concentration, $\epsilon_s$ is the sediment eddy diffusivity and $S$ in the source term modeling the net mass flux between the water column and the bed. Among the turbulence closure models available in Delft3D to obtain $\epsilon_s$, the algebraic eddy viscosity closure model was used. The reader is referred to Jiménez-Robles, Ortega-Sánchez, and Losada (2016) for further details on the sediment transport calculations. The changes in bed bathymetry computed every time step (except for the morphological spin-up interval) are determined by the spatial gradients of the bed load and the balance of the source and sink terms of the suspended sediment transport near the bottom.

## 5.4 Model setup and numerical scenarios

Similarly to previous chapters, the numerical domain was defined with a regular grid made by rectangular elements aligned with the river axis. The grid size varies, ranging from 100 x 100 m$^2$ at the offshore boundary to 10 x 10 m$^2$ at the river mouth. Stability and accuracy requirements were fulfilled using a time step of 1.50 s. The initial conditions were defined as water at rest (cold-start) and null global suspended sediment concentration. A 21-hour spin-up interval (starting at mean sea level towards high tide and finishing at low tide at the offshore boundary) was used, in which only the effect of the tides and a constant low river discharge of 5 m$^3$/s were modeled without morphological update.

Four open boundaries were considered (Fig. 5.2.1a). At the offshore boundary an harmonic water level condition representing astronomical tides was used, with an amplitude of 1 m (i.e., tidal range of 2 m) and a period of 12 h, characteristic of semidiurnal and mesotidal conditions. With this boundary condition, the ocean tide propagates form the seaward boundary towards the outlet with negligible variation of the tidal range, and then upstream the river mouth until approximately a distance of $5W$, considered as the tidal excursion. The two cross-shore boundary conditions were defined as Neumann-type, with null alongshore gradient of the water level to avoid numerical inaccuracies (Roelvink and Walstra, 2004). Finally, at the upstream boundary of the river channel, synthetic hydrographs were used as discharge boundary conditions after the spin up interval. These hydrographs were defined using the SCS (US Soil Conservation Service) method for shape (Chow, Maidment, and Mays, 1988) with a duration of 18 hours, equivalent to one and a half complete tidal cycle. According to the dataset (Ruiz-Reina, 2021), peak discharges of $Q_p = 200, 500, 1000$ m$^3$/s were used. The base time of the hydrographs was the same irrespective to the peak discharge value, which is based on a theoretical rainfall with same duration and increasing intensity. Equilibrium sediment concentrations were defined for the transport boundary conditions. Hence, at the upstream boundary this sediment concentration varies according to the instantaneous river discharge. This assumption prevents accretion or erosion near the model boundaries (Nardin and Fagherazzi, 2012; Jiménez-Robles, Ortega-Sánchez, and Losada, 2016). Constant coefficients for the bed friction (Manning $n$ = 0.020), background horizontal eddy viscosity ($\epsilon_H^{back}$ = 1 m$^2$/s) and sediment eddy diffusivity ($\epsilon_s$ = 1 m$^2$/s) were used over the computational grid. The values for the two later were defined according to (Jiménez-Robles, Ortega-Sánchez, and Losada, 2016).

A total of 12 simulations were defined as the combinations of three peak discharges per river width unit $q_p = Q_p/W = 1.0, 2.5, 5.0$ m$^2$/s and four lags between the peak discharge at the upstream boundary and the tide at the offshore boundary (Table 6.2.1). This lag, defined as $\phi$ and sketched in Fig. (5.4.1), accounts for the phase difference in a semidiurnal time scale between high tide and $q = q_p$, and values of $\phi = (0, \pi/2, \pi, 3\pi/2)$ were used, corresponding to peak discharge at high tide (HT), mean sea level towards low tide (MLT), low tide (LT) and mean sea level towards high tide (MHT), respectively. All simulations were run for 48 hours varying the upstream hydrograph used as boundary condition.

To validate the model and test the influence of the grid size on the results, two additional simulations were carried for $q_p$ = 2.5 m$^2$/s and $\phi = 0$: (1) one with a finer grid with resolution ranging from 50 x 50 to 5 x 5 m$^2$ at the offshore boundary and the outlet, respectively; and (2) another with a coarser grid with resolution ranging between 200 x 200 and 20 x 20 m$^2$. The results for the simulation 05 (Table 6.2.1) were used as reference values. The accuracy of the results was assessed using the depth average velocity in the centre of the outlet cross section and the instantaneous total sediment transport across the outlet section, for which a correlation coefficient ($R^2$) between the tested and the reference values was calculated for the period with the hydrograph flowing through the outlet section. The results for the depth average velocity were $R^2 = [0.997, 0.996]$ for the finer and coarser grids, respectively, whereas for the total sediment transport were $R^2 = [0.998, 0.994]$. The river mouth bar length along the axis from the outlet to the bar toe was also compared, obtaining relative errors of 9.1% and 9.3% for the finer and coarser grids. Hence, the results described throughout the next sections are numerically stable, and the obtained conclusions are not influenced by the numerical discretization of the domain.

| Simulation ID | $q_p$ (m$^2$/s) | $\phi$ (-) | Tidal level |
|---|---|---|---|
| 01 | 1.0 | 0 | HT |
| 02 | 1.0 | $\pi/2$ | MLT |
| 03 | 1.0 | $\pi$ | LT |
| 04 | 1.0 | $3\pi/2$ | MHT |
| 05 | 2.5 | 0 | HT |
| 06 | 2.5 | $\pi/2$ | MLT |
| 07 | 2.5 | $\pi$ | LT |
| 08 | 2.5 | $3\pi/2$ | MHT |
| 09 | 5.0 | 0 | HT |
| 10 | 5.0 | $\pi/2$ | MLT |
| 11 | 5.0 | $\pi$ | LT |
| 12 | 5.0 | $3\pi/2$ | MHT |

Table 5.4.1: Cases defined.

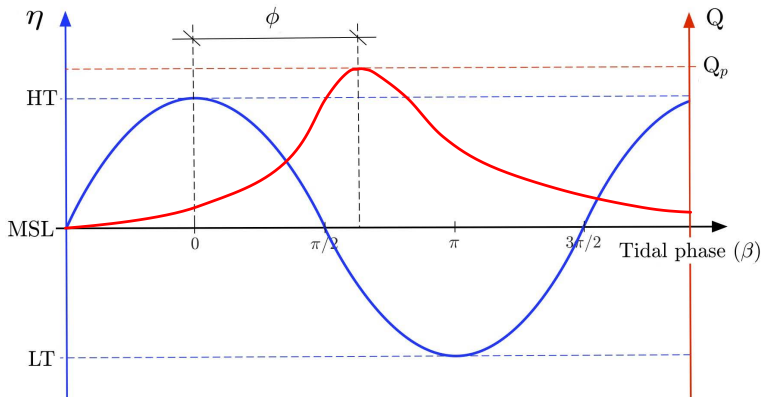


Figure 5.4.1: Definition sketch of the phase difference between the peak river discharge (red) and the tidal level (blue).

## 5.5 Hydrodynamics

### Water depths

Fig. (5.5.1) depicts the results for the water depth along the stream axis for the simulations detailed in Table 6.2.1. The X-axis represents time in terms of the tidal phase $\beta$, whereas the Y-axis represents the distance along the river axis non-dimensionalized with the river mouth width $W$, with positive values corresponding to the nearshore area. For the time scheme, $\beta = \pi$ represents half tidal cycle starting from $\beta = 0$. The results are showed for the interval $\beta \in [-2\pi, 3\pi]$ where the interplay between the river discharge and the tidal level plays a significant role on the hydro-morphodynamics. The origin ($X/W = 0$) is located at the river mouth outlet for the initial bathymetry. Rows and columns in the figure represent different $q_p$ and $\phi$ values, respectively. The last row illustrates the lag between the peak discharge (highlighted with a vertical red line) and the tidal cycle. Note that water depth values over 3.0 m were blanked to facilitate the interpretation of the colors in the figure. Furthermore, the results extracted at two locations

along the river axis are depicted in Fig. (5.5.2), showing the water depths at the initial outlet ($X/W = 0$) and $X/W = -4$, a section close to the upstream limit of the tidal excursion .

The analysis of Figs. (5.5.1) and (5.5.2) reveals that along the tidal excursion, the water depths resulting from the interaction between the river discharge and the tide depends mainly on $q_p$: whereas for $q_p = 1.0$ m$^2$/s the water depth increases are only clearly revealed along the entire lower part of the stream for $\phi = \frac{\pi}{2}, \pi$. For $\phi = 0, \frac{3\pi}{2}$ these increases are only perceived for $X/W \in$ (-4, -2). For these later cases, the effects of the tide and the river discharge in the lower part of the stream are not easily distinguished (Fig. 5.5.2, upper panel, solid lines). In contrast, as $q_p$ increases the effects of the river discharge are perceived closer to the outlet, regardless the value of $\phi$. Furthermore, the results at $X/W - 4$ (Fig. 5.5.2, lower panel) also shows that the effect of the river discharge and tidal celerities can be neglected at this subtidal time scale since there is no lag for maximum water depths along the stream: local maximum water levels before the hydrographs ($\beta = -2\pi$) coincide in time with the high tide prescribed at the offshore boundary, and maximum water depths after the hydrographs coincide with the peak discharges prescribed upstream.

For the role of $q_p$ at the outlet, Figs. (5.5.1) and (5.5.2) show that the higher $q_p$, the higher water depths are observed. Furthermore, as $q_p$ increases, water depths below 3 m are observed in the nearshore, indicating the formation of a nearshore bar. The final nearshore extension and advance rate of the bar depend on the combination of $q_p$ and $\phi$, and are described in following sections where the morphodynamic results are presented and discussed. In these sections, the formation of irregular bedforms in the lower part of the stream that trigger the water depth perturbations observed for $q_p = 5$ m$^2$/s (Fig. 5.5.1, third row) is also analyzed.

As for the role played by $\phi$ on the water depths at the outlet, maximum values are observed for $\phi = \frac{\pi}{2}, \pi$ regardless $q_p$ (Fig. 5.5.1, third column, Fig. 5.5.2, upper panel). Furthermore, the maximum water depths at the outlet are observed at the high tide following the peak discharge ($\beta = 2\pi$) for all the modeled scenarios. In contrast, the maximum water depth upstream ($X/W = -4$) is observed for the peak discharge (Fig. 5.5.2, lower panel). Hence, the maximum water depths are not observed when the maximum river discharge coincide with the high tide. This result highlights the importance of the complex interaction between river discharge and ocean tides at the downstream stretch of the channel, as maximum depths at the outlet coincide with the high tide after the peak discharge regardless $\phi$.

## Along-channel velocities

Following the scheme presented for Fig. (5.5.1), Fig (5.5.3) depicts the results for the along-channel current. The results for a complete tidal cycle before the discharge begins ($\beta \in [-2\pi, 0]$ for $\phi = 3\pi/2$ in Fig. 5.5.3, third column), show that maximum ebb velocities are observed approximately at low tide conditions, corresponding to a quasi-purely progressive tidal wave, which is typical for rivers with constant cross-channel section (Savenije, 2012). For all cases, velocities are clearly higher at the channel, with a sudden descent as the discharge flows into the nearshore due to the increase of the cross-sectional area. As mentioned for the water depth analysis, the bar formation at the outlet triggers the advance of higher currents to $X/W > 0$ as the bar develops and its crest moves into the nearshore.

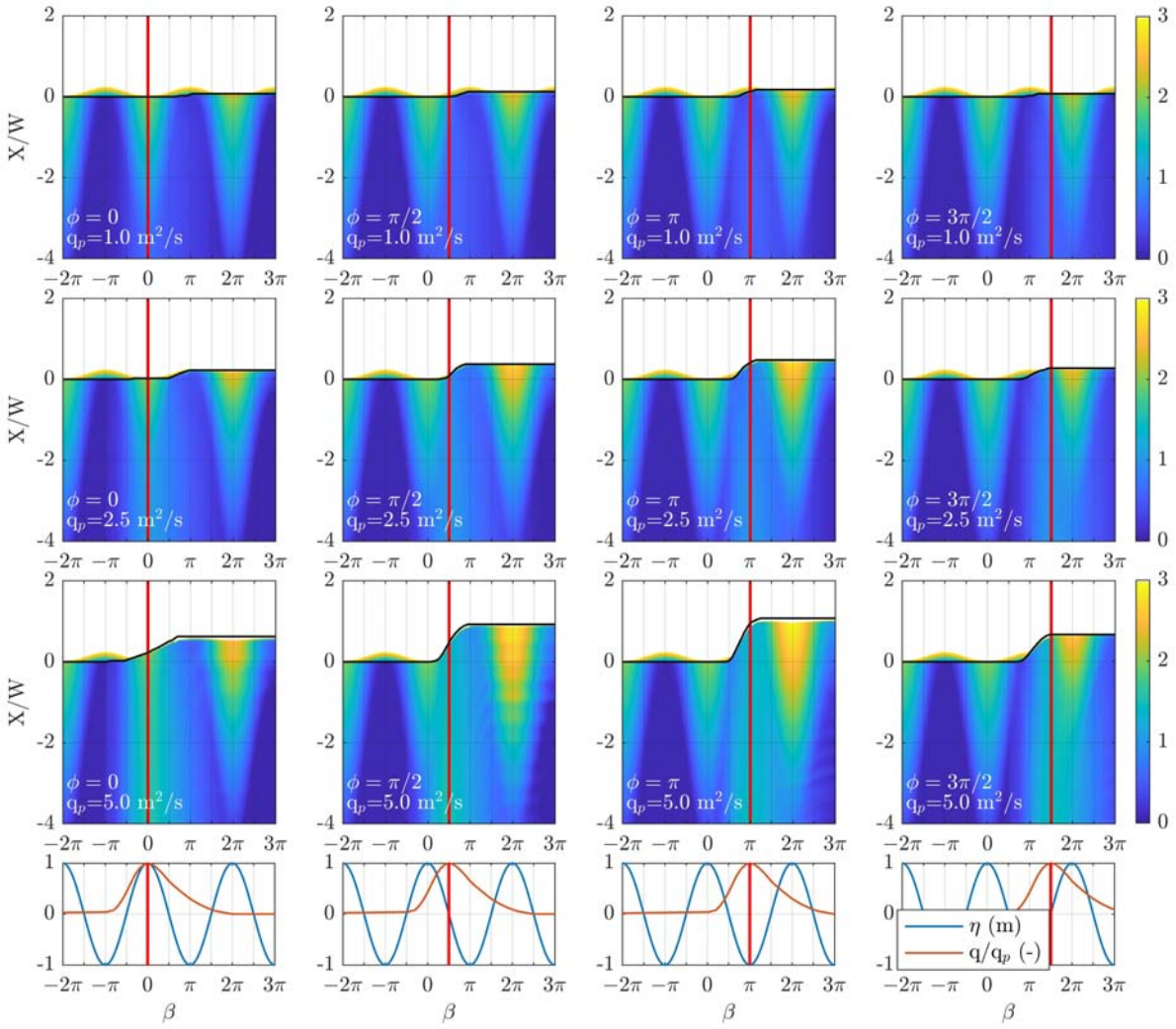


Figure 5.5.1: Time evolution of the water depth (m) along the stream axis ($Y = 0$) for the simulations detailed in Table 6.2.1, with columns and rows showing different $\phi$ and $q$ values, respectively. Vertical and horizontal axes represent the non-dimensional length along the stream axis ($X/W$) and time in terms of the tidal cycle ($\beta$), respectively. The last row shows the offshore water level (blue) and the non-dimensional river discharge (red). Vertical red lines represent the instant for the peak river discharge at the upstream boundary. The black lines represent the position of the outlet as the bar develops.

Results in Fig. (5.5.3) show that the maximum velocities observed in $X/W \in [-4,2]$ depend mainly on the $q_p$ value, with increasing velocities as the river discharge rises. The tidal lag $\phi$ plays a secondary role on these maximum values, which are higher for $\phi = \pi$, when the peak discharge coincides with the maximum ebb approximately at low tide. However, although these maximum velocities are observed at the outlet for all the cases, the instant in which these velocities are found depends mainly on the tidal conditions, as maximum velocities are observed always at $\beta = [\pi/2, \pi]$ (tidal ebb). Hence, if the peak discharge occurs before $\beta = \pi$ (Fig. 5.5.3, first

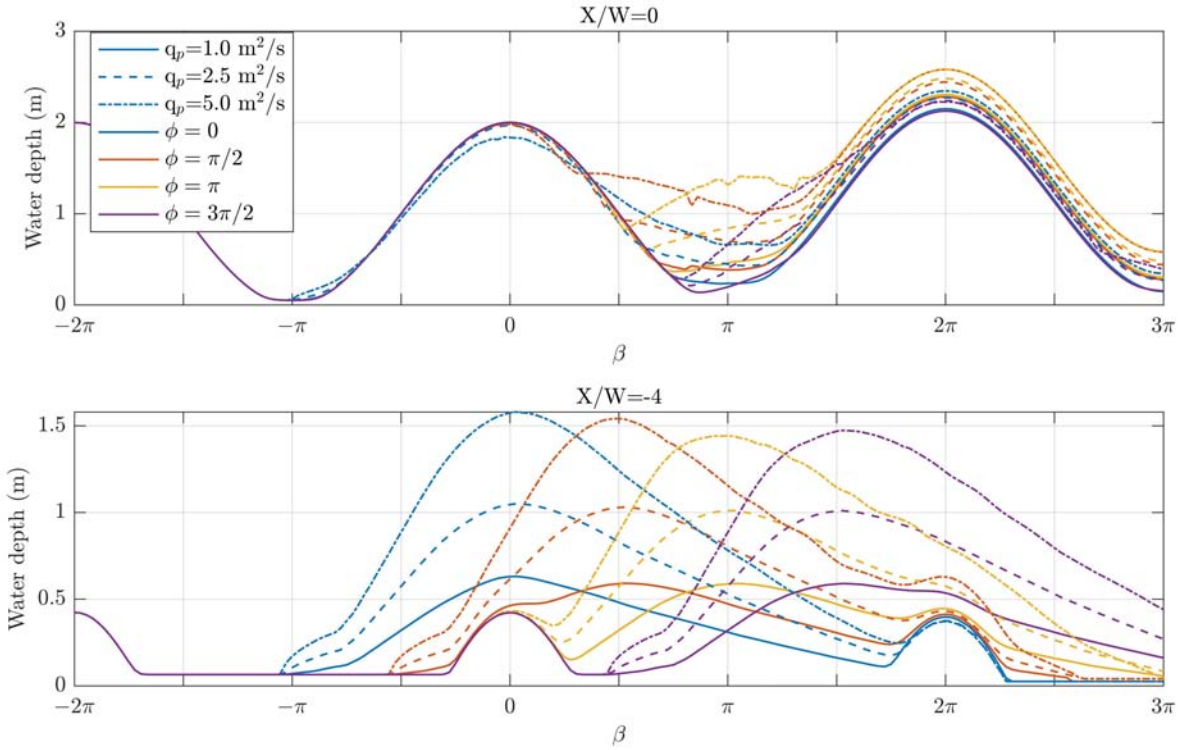


Figure 5.5.2: Time evolution of the water depth (m) at $X/W = 0$ (upper panel) and $XW = -4$ (lower panel). Solid, dashed and dash-dotted lines represent results for $q_p = [1.0, 2.5, 5.0]$ m$^2$/s, respectively. Blue, red, yellow and purple lines represent the results for $\phi = [0, \pi/2, \pi, 3\pi/2]$, respectively.

and second columns), the maximum currents progress until low tide, delaying if the opposite occurs (Fig. 5.5.3 fourth column). This effect has an important consequence on the duration of higher currents triggered by the extreme river discharge events: whereas for $\phi = 0$ and $\phi = 3\pi/2$ the period is over one tidal cycle ($\Delta\beta \in [2\pi, 3\pi]$), it reduces to less than a tidal cycle for $\phi = \pi/2$, even when the hydrograph has the same base time. Conversely, maximum upstream ($X/W < -2$) and offshore ($X/W > 1$) currents coincide with the maximum river discharges. Hence, the effect of $\phi$ on the temporal distribution of the maximum velocities is reduced to a channel length of approximately $3W$ located close to the outlet.

Summarizing, the value of the maximum currents is dominated by the maximum river discharge, with the lag between this peak discharge and high tide playing a secondary role. However, the tidal conditions stand out as the key parameter controlling the instant in which these maximum velocities are observed. These results highlight the complexity of the interaction between river discharge and tide at the lower part of the stream, particularly between $X/W \simeq -2$ and the outlet although as discussed in the next section, tides also affect along-channel velocities up to $X/W = -8$ for the highest peak discharge. This complex behavior of the hydrodynamics is key on the control of the morphodynamic behavior, as showed throughout the following paragraphs.

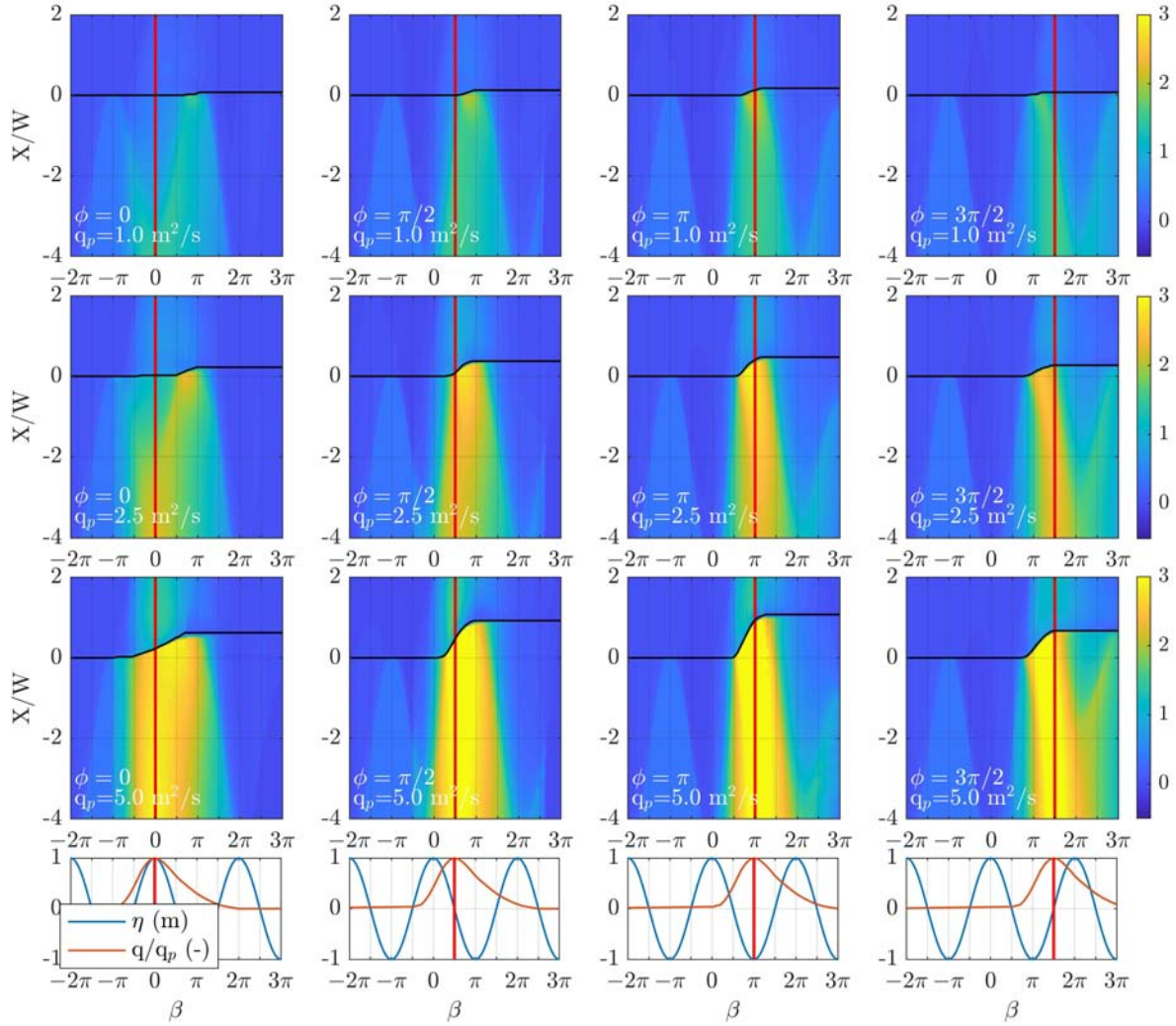


Figure 5.5.3: Time evolution of the along-channel current (m/s) along the stream axis ($Y = 0$) for the simulations detailed in Table 6.2.1, with columns and rows showing different $\phi$ and $q$ values, respectively. Positive values indicate water flowing from the upstream boundary to the outlet. Vertical and horizontal axes represent the non-dimensional length along the channel axis ($X/W$) and time in terms of the tidal cycle ($\beta$), respectively. The last row shows the offshore water level (blue) and the non-dimensional river discharge (red). Vertical red lines represent the instant for the peak river discharge at the upstream boundary. The black lines represent the position of the outlet as the bar develops.

## Maximum velocities

The understanding of the hydrodynamic conditions during extreme river discharge events can be further understood through the analysis of the along-channel variations of the maximum velocity reached during the simulation along the stream axis (Fig. 5.5.4a). As expected, the maximum velocity remains constant along the upstream section of the channel where geometry, slope and roughness are constant. As a consequence, higher discharges lead to higher maximum

velocities. However, as the flow approaches the river mouth, the influence of the tide is clearly perceived through a local increase of the maximum velocity up to a local peak value at the outlet $U_0$. As previously described, after this peak value is reached, a sudden decrease of the maximum velocity in the nearshore is observed. These results are qualitatively very similar to the quasi-2-D numerical experiments for high flow transient river discharges obtained by Chatanantavet and Lamb (2014), who also conducted exploratory flume experiments to validate the model, and those of Lamb et al. (2012) for high river discharges at the Mississippi river.

Note that the geometry and physical conditions of the stream, based on the aforementioned seasonal and ephemeral river database (Ruiz-Reina, 2021), lead to a subcritical hydraulic regime along the channel. However, higher river discharges, steeper bed slopes or a less frictional channels could lead to supercritical flows, for which hydraulic jumps could develop at the outlet, varying their positions with the tidal conditions and the evolution of the river mouth bar. In that case, the detailed calculation of the hydraulic response at the outlet (i.e. hydraulic jump development), should be analyzed with a 3D extension of the numerical modeling and the inclusion of non-hydrostatic effects.

The location of the peak velocity $U_0$ (and hence the location of the outlet) varies for each simulation as a consequence of the bar development. This position was determined as the location where maximum along-channel velocities are found inside an area close to the river mouth, coinciding with the position of the bar crest that evolve during the simulation. Higher peak values correspond to $q_p = 5$ m$^2$/s. However, for $q_p = 2.5$ m$^2$/s and $\phi = \pi$, the $U_0$ value is similar to that for $q_p = 5$ m$^2$/s and $\phi = 0$. A similar behavior can be observed for $q_p = 2.5$ m$^2$/s and $q_p = 1.0$ m$^2$/s. These results emphasize the relevance of $\phi$ as a key parameter controlling $U_0$: whereas maximum velocities similar to those of the upstream boundary are found for $\phi = 0, 3\pi/2$, there is a significant increase when the peak of the hydrograph approximately coincides with the ebb $\phi = \pi/2, \pi$. Contrasting to the main role played by the ebb in the outlet velocity increase, water depths at this location are higher for ebb conditions close to the peak discharge (Fig. 5.5.2). The rise in $U_0$ involves higher bed shear stresses in the river bed, which is the key parameter for the bed load transport. A second consequence of the $q_p$ variation is the extension of the tidal influence along the stream. It is clear that higher discharges imply larger tidal-influence distances upstream; in particular, $X/W = [-8, -5, -1]$ for $q_p = [5.0, 2.5, 1.0]$ m$^2$/s, respectively. This is due to the backwater curves associated to each simulation, for which the difference between the normal depth and the depth at the outlet increases as $q_p$ does (Ruiz-Reina et al., 2020), hence increasing the length where the varied flow develops. The extension of the upstream tidal-influence may vary for different river discharges and physical characteristics of both the channel and the nearshore, such as slopes, roughness and channel width and convergence (Melito et al., 2020). However, although the results presented here were obtained for the averaged characteristics of the rivers included in (Ruiz-Reina, 2021), the role played by $\phi$ must remain.

The temporal variations in $U_0$ are analyzed in Fig. (5.5.4b), where the X-axis represents time in terms of the tidal phase $\beta$, whereas the Y-axis represents the maximum velocity at the outlet ($U_0$) for each simulation. The outlet movements towards the nearshore as the bar develops (Fig. 5.5.3) were considered to obtain these results. Again, the higher the $q_p$ is, the maximum peak velocity is achieved for the same $\phi$. Furthermore, the displacement of the instant with maximum velocities along the tidal cycle towards the tidal ebb ($\beta \simeq \pi$) is more pronounced for lower $q_p$.

An imaginary line can be drawn linking the maximum $U_0$ values for the same $\phi$ (dots of the

same color). For $\phi = 0$ (blue dots), this line clearly decreases as $q_p$ does (maximum velocities are obtained later for lower discharges), with $U_0$ approximately coinciding with high tide for $q_p = 5.0$ $m^2/s$. However, as $q_p$ decreases, $U_0$ is displaced towards low tide causing a deformation of the velocity profile. For $\phi = \pi/2$ and $\phi = \pi$ (red and yellow dots, respectively), these lines are more vertical (i.e., the maximum velocities are observed in a shorter period), whereas for $\phi = 3\pi/2$ (purple dots), the imaginary line increases (maximum velocities are obtained later for higher discharges) as $q_p$ does, highlighting once again that for lower $q_p$ the maximum outlet velocities are always close to low tide, whereas for higher $q_p$ values the instant for maximum $U_0$ is less influenced by the tide conditions. For the lower peak discharge, maximum $U_0$ are concentrated in less than a quarter of the tidal cycle, whereas for $q_p = 5.0$ $m^2/s$ instants of maximum $U_0$ spread for almost half of a tidal cycle.

These results emphasize that the dominance of the coastal hydrodynamics leads to notable modifications of the current velocities in terms of maximum velocity values and time evolution, both at the outlet and upstream, with a blur limit to define when this dominance is relevant. In these simulations, the tidal influence on the instant when the higher velocities are obtained is clearly appreciated for $q_p = 2.5$ $m^2/s$, but is much less important for $q_p = 5.0$ $m^2/s$.

## 5.6 Morphodynamics

### Bed shear stresses and sediment transport

The combination of water depths and along-channel velocities determine the bed-shear stresses during the flood event, that in turn trigger both the bed load and suspended sediment transport along the channel. This sediment transport flows into the nearshore, that can be considered as a basin in which there is a rapid expansion in cross-sectional area. There, the flow velocity decreases suddenly, as showed in Fig. (5.5.3), and so does the sediment transport rate, then promoting sediment deposition and the development of a river mouth bar. Consequently, the more intense the sediment transport decay is, the more rapidly the river mouth bar develops and the higher final volume is reached (Edmonds and Slingerland, 2007).

To analyze the role of $\phi$ on the sediment transport variations and the development of the river mouth bar, Fig. (5.6.1) shows the bed shear stresses at the initial outlet and the total sediment transport rates across the initial outlet cross-section. The sediment transport rates were obtained as the combination of the bed load and the suspended sediment transport computed by the model. Furthermore, depth-averaged velocities and water depths in the outlet centerline are also shown, jointly with the total water discharge across the outlet cross-section. For the depth-averaged velocities, in addition to the concentration of the maximum values in a shorter interval, and the fact that maximum velocities at the outlet are higher for $\phi = \pi/2$ and $\phi = \pi$ (peak river discharges simultaneous to tidal ebb as showed in Figs. 5.5.3 and 5.5.4), results show that there is a sudden increase of the velocity for $q_p = 5.0$ $m^2/s$ triggered by the bathymetric changes.

Given the nonlinearity of the bed shear stress with respect to these velocities, the differences in the maximum velocities for different phases are amplified if the bed shear stresses are compared. The relative differences between those two $\phi$ $(\pi/2, \pi)$ values for which maximum velocities are observed and those corresponding with the lower velocities at the outlet are decreasingly important as $q_p$ rises and the role of the tide drops. For instance, the differences

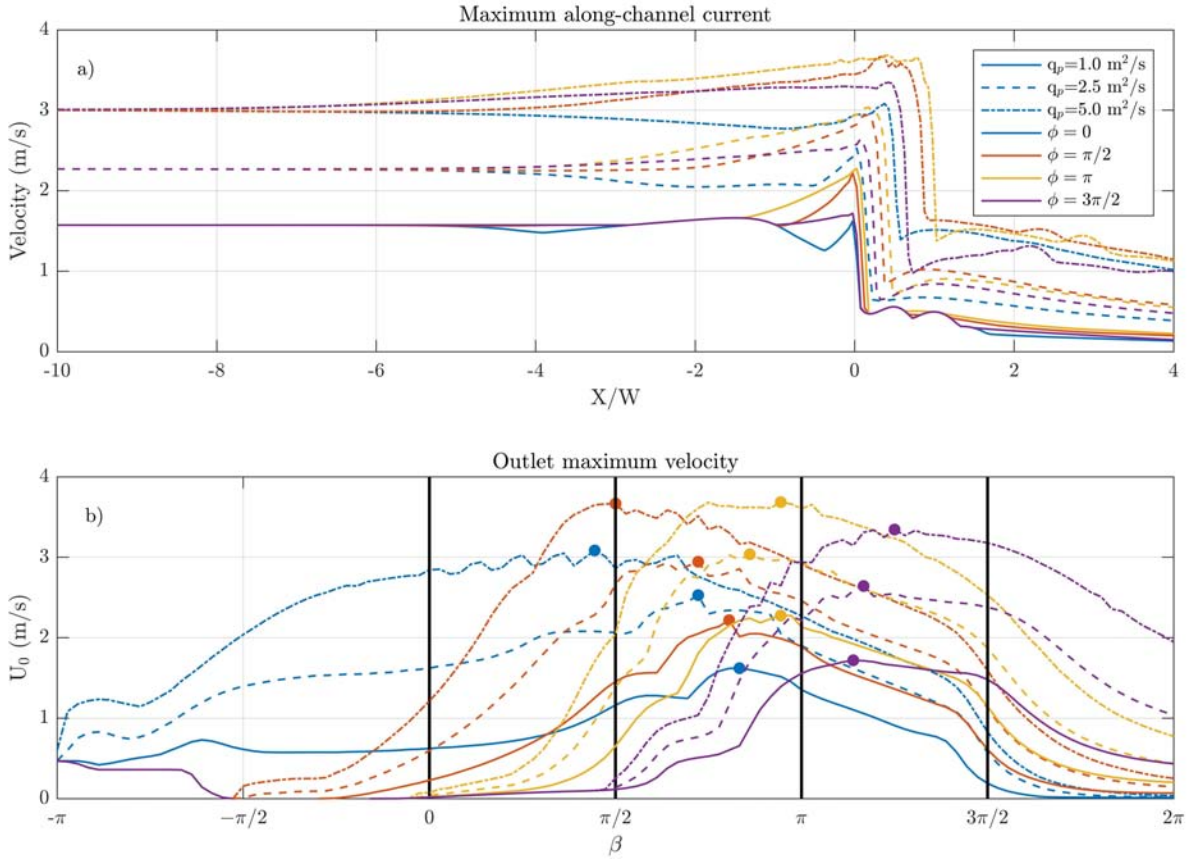


Figure 5.5.4: Maximum velocities: a) along channel; b) at the outlet. Solid, dashed and dash-dotted lines represent results for $q_p = [1.0, 2.5, 5.0]$ m$^2$/s, respectively. Blue, red, yellow and purple lines represent the results for $\phi = [0, \pi/2, \pi, 3\pi/2]$, respectively. Color dots represent the maximum velocities at the outlet during the simulated period, whereas the vertical black lines represent the time for $q = q_p$ for each $\phi$ value.

between maximum bed shear stresses for $q_p = 1.0$ m$^2$/s are close to 100% (see the differences between maximum values for $\phi = 0$ and $\phi = \pi$, Fig. 5.6.1 first column), whereas for $q_p = 5$ m$^2$/s are 40%, approximately.

According to the bed load sediment transport rate used in the model, the transport is proportional to the difference between the actual bed shear stress and its critical value to the power of 1.5 or 2.1, depending on the hydrodynamic conditions (Eq. 5.2). This nonlinearity explains how the differences in maximum values of total sediment transport are also amplified with respect to those of the bed shear stresses. Furthermore, the existence of a movement threshold for the sediment particles shorten the period in which there is sediment transport (and hence the bar may develop) respect to the period in which velocities and bed shear stresses rise due to the river discharge. For $q_p = 1.0$ and 2.5 m$^2$/s, this period is $\beta \in (\pi/2, 3\pi/2)$, corresponding to the interval in which water levels are below the mean sea level. For a semidiurnal tide, this interval corresponds to approximately 6 hours, whereas the base time for the river discharge hydrograph is 18 hours. For these two peak discharge values, the period in which the sediment is mobilized through the

outlet is approximately the same for all the $\phi$ tested. For $q_p$ = 5.0 m$^2$/s, results show that the river discharge is able to produce bed shear stresses above the critical value ($\simeq$ 0.5 N/m$^2$) for longer periods which are not simultaneous between different $\phi$ values. For $\phi = 0$, the period where sediment particles are mobilized is close to $5\pi/2$, while for the rest of the phases is close to $\pi$.

The combination of higher maximum values of total sediment transport and equal (or even shorter) periods of sediment mobilization, determines the differences in the temporal sediment transport gradients, that in turn determine the differences in the river mouth development for each $\phi$. For $\phi = \pi/2$ and $\phi = \pi$, the shorter periods of sediment mobilization determine a higher speed for the bar development, as discussed in the next section. However, since the sediment volumes flowing from the channel to the nearshore (i.e. the area under the total sediment transport curve in Fig. 5.6.1, fifth row) are significantly higher than those of $\phi = 0$ and $\phi = 3\pi/2$, the final extensions and volumes of the bars will show large variability, as discussed below. These differences in the final bar characteristics are significantly important between $\phi = 0$ and $\phi = \pi$, irrespectively the value of $q_p$ value, highlighting the role that the phase plays on the river mouth bar evolution. The development speed, volumes and final extension and shape of the river mouth bars are presented and discussed throughout the next sections.

### River mouth bar profiles

Fig. (5.6.2) depicts the time evolution of the bed level changes along the stream axis for the simulations in Table 6.2.1. For all the cases analyzed, accretion is observed from the outlet (initially at $X/W = 0$) towards the nearshore, corresponding to the formation of the river mouth bar, while some erosion occurs upstream. In contrast with this accretion, the upstream erosion has a maximum value that is partially recovered by the end of the river flood, being slower for decreasing values of $X/W$. The offshore extension of the bar, delimited by the envelope of the accretion observed in Fig. (5.6.2), depends mainly on $q_p$, with larger extensions for higher peak discharges. The lag $\phi$ also plays a relevant role on the final extension: the closer the peak discharge is to the maximum ebb at low tide, the further the bar extends into the nearshore and the higher maximum accretion values are obtained. Hence, larger bars are obtained for $\phi = \pi$ (Fig. 5.6.2, third column).

Fig. (5.6.3) depicts the time evolution of the river mouth bar sediment volume obtained as the cumulative variation of sediment in the nearshore ($X/W \geq 0$). Although the value of $q_p$ determines the order of magnitude of the final sediment volumes achieved (approximately $10^3$, $10^4$ and $10^5$ m$^3$ for $q_p$ = 1.0, 2.5, and 5.0 m$^2$/s, respectively), $\phi$ plays a major role on these volumes with variations close to 400% between $\phi = 0$ and $\phi = \pi$ for $q_p$ = 1.0 and 2.5 m$^2$/s. For $q_p$ = 5.0 m$^2$/s, the relative differences between different lags are lower. Although these relative variations of the sediment volume may suggest that increasing values of $q_p$ can potentially reduce the tidal effects, the magnitude of the sediment volumen variations for $q_p$ = 5.0 m$^2$/s is still much larger than for lower $q_p$ values. Hence, these results also highlight the complexity of the interaction between river and coastal processes, that in turn determines the final characteristics of the river mouth bars.

Fig. (5.6.3) also shows the period during which the bar is developed, defined as the interval between the start of the accretion at the nearshore and the instant for which the sediment volume variations reach a stationary value. The results show that the duration of this development period

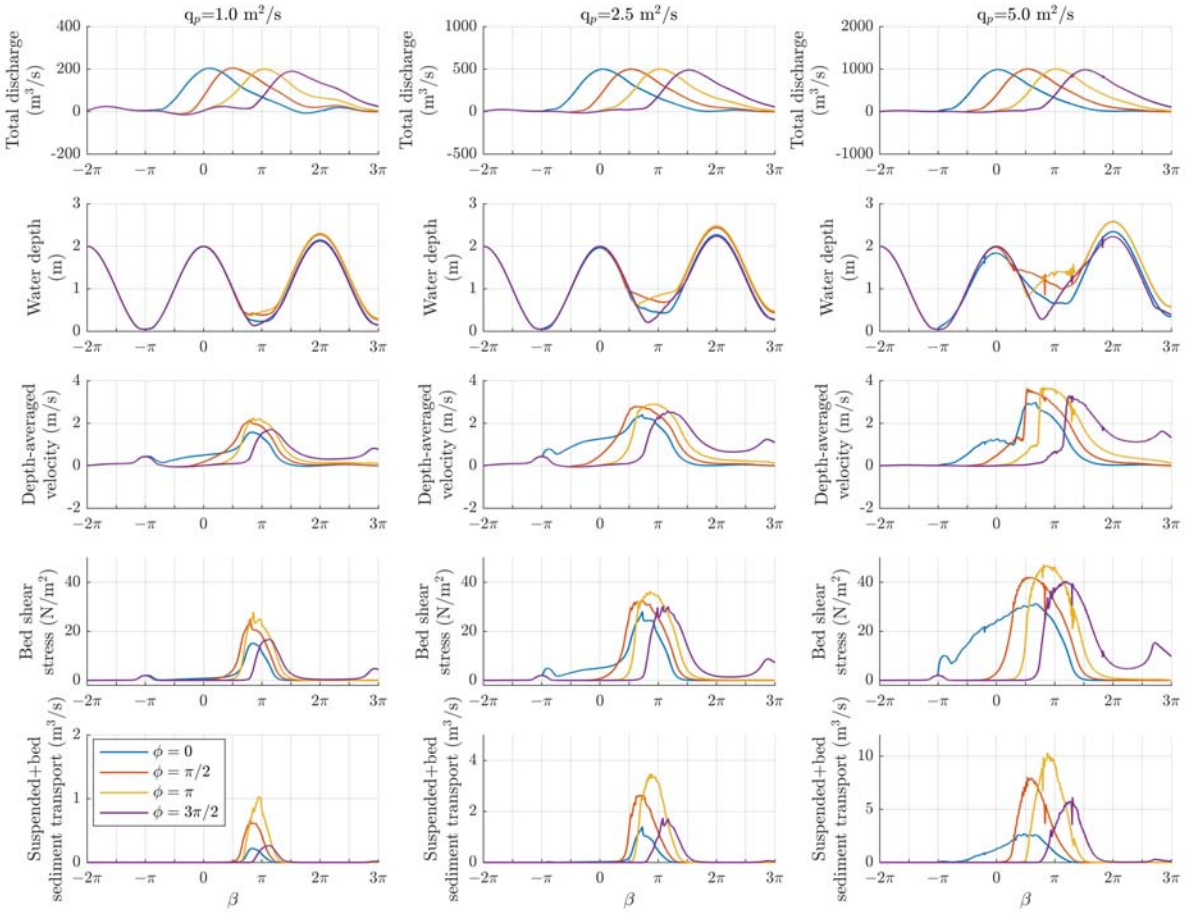


Figure 5.6.1: Hydrodynamics, bed shear stresses and sediment transport at the initial outlet. The first row represents total water discharge across the outlet cross-section. Rows 2 to 5 represent the following variables at $X/W = 0$ and $Y/W = 0$: water depth, depth-averaged velocity, bed shear stress and total sediment transport, respectively. Columns 1 to 3 depicts the results for $q_p$ = 1.0, 2.5 and 5.0 m$^2$/s, respectively. Color in each panel represent the results for $\phi = 0$ (blue), $\phi = \pi/2$ (red), $\phi = \pi$ (yellow) and $\phi = 3\pi/2$ (purple).

mainly depends on $\phi$, since no significant variations for this duration are observed for cases with the same $\phi$ but different $q_p$. This duration is clearly larger for $\phi = 0$, when the maximum river discharge is simultaneous to the high tide. In this case, this duration is approximately 3/4 times of tidal cycle, from the mean sea level preceding the high tide to low tide ($\beta \in [-\pi/2, \pi]$), although for $q_p$ = 1.0 and 2.5 m$^2$/s the initial accretion is very weak until $\beta = \pi/2$. Minimum durations are found for $\phi = \pi$ with durations barely exceeding 1/4 of the tidal cycle ($\beta \in [\pi/2, \pi]$). According with these results, $\phi$ also determines when the bar initiates its development, since depending on the $\phi$ value, the timing of the bed shear stress and sediment transport increases due to the hydrograph rise is modified, coupling this increases with the tidal ebb. However, for $\phi = 0$ and $q_p = (1.0, 2.5)$ m$^2$/s the initial development of the bar is limited, and only for $q_p = 5$ m$^2$/s the river discharge is able to produce significant accretion in the nearshore even during the high tide and the tidal flood period.

Fig. (5.6.4) depicts the final bed level profiles obtained along the channel axis for all the simulations. Results show that there is an important variability of the final extension of the bar, ranging between $0.05W$ and $1.0W$, approximately. The analysis of the first row of this figure, where the results for different $q_p$ and same $\phi$ are compared, shows that the main responsible of the bar advance and its final area is $q_p$. This extension, measured as the final position of the bar crest, is approximately proportional to $q_p$. Likewise, Fig. (5.6.4c) show that $\phi$ has also an important role of the final extension of the bar, but less important than $q_p$: while the variations between the maximum and the minimum extensions of the bar for different $q_p$ is close to $0.75W$ (Fig. 5.6.4a3), it is approximately $0.5W$ for different $\phi$ (Fig. 5.6.4c).

The analysis of the second row in Fig. (5.6.4) reveals that among the $\phi$ values tested, the bar extension is more limited for those phases when the peak discharge coincides with tidal flood ($\phi = 0$ and $\phi = 3\pi/2$), in contrast with those phases at tidal ebb ($\phi = \pi/2$ and $\phi = \pi$) when the maximum bar extensions are obtained. For instance, Fig. (5.6.4b3) shows that for $q_p = 5$ $m^2/s$ the bar crest reaches $X/W \simeq 0.55$ and up to $X/W \simeq 0.95$ for tidal flood and ebb conditions, respectively. This difference represents approximately 100% of the extent for $\phi = 0$. These results suggest that the final extension of the developed bars is clearly controlled by the peak discharge and the tidal conditions. Finally, irregularities along the channel profile are observed for $q_p = 5$ $m^2/s$, corresponding to bedforms up to 0.5 m in height that modifies both the water levels and the along-channel velocities, as previously described. These bedforms develop as a consequence of the erosion processes identified at the final extent of the channel (Fig. 5.6.2).

### River mouth bar plan shape

Fig. (5.6.5) represents the nearshore bed levels for the different $q_p$ and $\phi$ values tested. It shows that for $q_p = 1.0$ $m^2/s$ the sediment eroded along the stream and entering the upstream boundary is deposited in a transverse bar with a linear form and a maximum bar height (bed level difference between the crest and the toe) below 1.5 m. For $q_p = 2.5$ $m^2/s$ the shape is closer to a semi-ellipse, being the nearshore extension larger along the stream axis than along the lateral banks. In these banks, subaqueous levees develop with extensions varying from $0.1W$ to $0.25W$ depending on the $\phi$ value. Finally, for $q_p = 5.0$ $m^2/s$, the shape changes to a round parallelepipedic form with the major axis aligned with the stream axis. For this $q_p$, the further extension of the bar is not clearly located at $Y/W = 0$, and two symmetric peaks begin to appear on $Y/W \pm 0.25$ for $\phi = \pi/2$ and $\phi = \pi$. Water depths at the bar crests for these cases are close to 2.0 m, with heights over the bar toe of 5.0 m due to the progression of the bar into the nearshore. The subaqueous levees extend significantly compared to those for $q_p = 2.5$ $m^2/s$, reaching $X/W = 0.5$. The influence of $\phi$ is equivalent to a scale factor for the plan shapes: for $\phi = \pi/2$ and $\phi = \pi$ they exhibit more extended accretion forms in the nearshore along the X-axis. Furthermore the analysis of the final sediment volumes shows that they are similar for all $\phi$ values, but in case $\phi = 0$ and $\phi = 3\pi/2$, the bar is higher and shorter than those corresponding to $\phi = \pi/2$ and $\phi = \pi$.

Fig. (5.6.6) shows the time evolution of a longshore profile of the bathymetry at $X/W \simeq 0.1$, corresponding to the initial 2.6 m isobath. With this representation of the results, the lateral levees are clearly identified, peaking approximately at $Y/W = \pm 0.6$. For $q_p = 1.0$ $m^2/s$ and $\phi = 0, 3\pi/2$, these levees do not develop, coinciding with the cases with lower bar volumes and extensions. Furthermore, it can be seen how the water depth at this section evolves during the bar development, generally with three periods: (1) a sudden decrease of the depth at the

beginning of the bar development when the bar crest crosses $X/W \simeq 0.1$; (2) a period in which the water depth increases during the bar extension; and (3) the last period in which the water depth decreases again (slower than the fist period) until its final geometry. This behavior is different for $q_p$=1.0 m$^2$/s and also for $\phi = 3\pi/2$ irrespectively the $q_p$ value, cases for which the second period is not identified. These results highlight again the different timing and evolution of the development of the nearshore bar depending on $\phi$, as discussed above.

Although to the best of the authors knowledge no previous works analyzed the river mouth bar development for similar conditions, the geometry of the bar front and the development of the lateral levees obtained for the maximum $q_p$ are qualitatively similar to those obtained by other researcher such as Edmonds and Slingerland (2007) or Jiménez-Robles, Ortega-Sánchez, and Losada (2016) for long-term simulations and steady river discharges. The main differences are: (1) the extension of the bar into the nearshore, and (2) the lateral spreading of the bar, as final bar widths in Edmonds and Slingerland (2007) and Jiménez-Robles, Ortega-Sánchez, and Losada (2016) are clearly larger. These differences are mainly attributed to the differences in the time scale of the events: even considering the extreme river discharge values modeled here, the cumulative sediment and water volumes entering the nearshore through the river mouth are very different, as those previous results were obtained after more than 100 days of simulation. Although similar results can be expected for longer river discharge hydrographs or even with a series of extreme events (neglecting the effects of ocean waves between them), that analysis does not correspond with the aims of this work.

In the case of the lateral spreading, Edmonds and Slingerland (2007) showed that bars under steady conditions present two different stages during their development: (1) basinward prograding; and (2) lateral widening once the bar reaches certain length. In contrast to the results of Edmonds and Slingerland (2007), here the bar stops prograding not because the sediment is not able to reach the bar toe to continue its growth, but because the hydrograph descend after the peak discharge, reducing also the sediment concentration and the bed load (Fig. 5.6.2). Hence, the second stage of widening does not occur. Furthermore, the nearshore slope differentiates the results presented here: whereas Edmonds and Slingerland (2007) and Jiménez-Robles, Ortega-Sánchez, and Losada (2016) intended to model the river mouth development of rivers debouching on water bodies with constant depth or constant beach slopes, here we use a more realistic representation of the nearshore using the equilibrium beach profile defined by Dean and Dalrymple (2004). This profiles, for which water depth increases more rapidly than those with constant slope, imply that water depth increases more quickly as the river discharge and/or the tidal ebb move offshore. This may led to differences in the final shape and reach of the bars, although specific numerical experiments must be done to analyzed that. However, these experiments are out of the scope of the present work, as our main goal is to analyze the role of $\phi$ on the hydro-morphodynamics during extreme events.

### Downstream river bedforms

The analysis of the final bed elevation in the downstream river stretch leads to some additional considerations regarding the development of river bedforms (Fig. 5.6.7). For $q_p = 1.0$ m$^2$/s and $q_p = 2.5$ m$^2$/s the contours in the bed stream show minor modifications of the initial bed elevation, with a slight erosion of the bed in agreement with Figs. (5.5.4) and (5.6.2). In these cases, the general tendency to erosion along the stream is balanced in the outlet with the formation of the

bar.

In contrast, for $q_p = 5.0$ m$^2$/s the final bed elevation shows a clear braided morphology, typical of intense bed-load transport streams (Bristow and Best, 1993). A symmetrical series of alternate erosion/accretion processes is developed in the stream triggering a set of very active channels and ephemeral bars. The resulting balance is general erosion along the stream and deposition in the river mouth bar, jointly with an irregular river bed profile. This process is the response to higher currents, associated with the largest volumes of sediment.

After the analysis of the results, a different pattern for the river and mouth bar morphology for each $q_p$ value can be deduced. The mouth bar develops from a short and linear shape to a ellipse which is elongated and may be transformed into a rounded rectangular form, as $q_p$ increases from 1.0 to 2.5 and 5.0 m$^2$/s, respectively. On the other hand, the downstream bed morphology shows a clear evolution from a constant regular bed slope to a braided geometry when the peak discharge increases from 2.5 to 5.0 m$^2$/s.

**Final remarks**

This chapter aims to shed some light on a question related to the river mouth hydro-morphodynamics during extreme river discharge events: does the time lag between the maximum river discharge rate and the high tide have a role on the bar development during these events? Is this role important enough to be considered in engineering applications? These questions are relevant both from scientific and management perspectives, since they may help to better understand the complex interaction between river discharges and ocean tides, and may be also useful to engineers and managers dealing with the impacts of extreme events in coastal spots, usually densely populated, that historically have caused significant social and financial losses.

The physical scenarios and numerical model implementation used, validated after a sensitivity analysis for grid scale effects, constitute an adequate tool to analyze the proposed problem. The analysis of the results obtained with this framework has demonstrated that the time lag between the maximum river discharge rate and the high tide plays a major role on the river mouth bar development and have to be considered in any short term river mouth hydro-morphodynamic analysis. These statements are supported by the following conclusions:

- Although the peak discharge rate $q_p$ is the major parameter controlling both the hydrodynamics and the morphodynamics of extreme discharge events, the time lag between this maximum rate and the high tide $\phi$ plays also a very important role on the water levels, currents, shear stresses, sediment transport and finally river mouth bar development. This role is more important as $q_p$ decreases.
- Despite of the value of the maximum flow velocities at the mouth is dominated by the maximum river discharge, the tidal conditions stand out as the key parameter controlling the instant when the maximum velocities are observed: as $q_p$ decreases, the maximum velocity of the mouth is advanced or retarded towards low tide causing a deformation of the velocity profile. This complex behavior of hydrodynamics, which may seem intuitive, is essential in the morphodynamic evolution of the mouth bar, determining the duration of its development and its final characteristics, doubling their final extension and quadrupling the final bar volume for the same river discharge conditions and different phase lag.
- The variability in the final extension of the bar is of the same order of magnitude among different $q_p$ and $\phi$ values (0.7 and 0.5 channel widths, respectively). The bar extension is more limited for those phases with the peak river discharge coinciding with the tidal flood, in contrast to those phases at the ebb of the tide where the maximum bar extensions are obtained. These results suggest that the final extension of the bars is controlled by a combination of peak discharge and tidal conditions, and the effect of either cannot be neglected.
- The bar front geometry and lateral levee development obtained for maximum $q_p$ are qualitatively similar to those obtained in other works for long-term simulations and stationary river discharges, although differences in lateral propagation and bar extension are observed due to time scale and beach profile differences.
- The results highlight the complex interaction between fluvial and coastal hydrodynamics, where the dominance of the latter leads to significant changes in current velocities and mouth evolution. The boundary for which tidal processes dominate is very diffuse. In the simulations performed, the influence of the tide at the instant when the highest velocities are obtained is clearly observed for $q_p \leq 2.5$ m$^2$/s but much less important for $q_p = 5.0$ m$^2$/s.

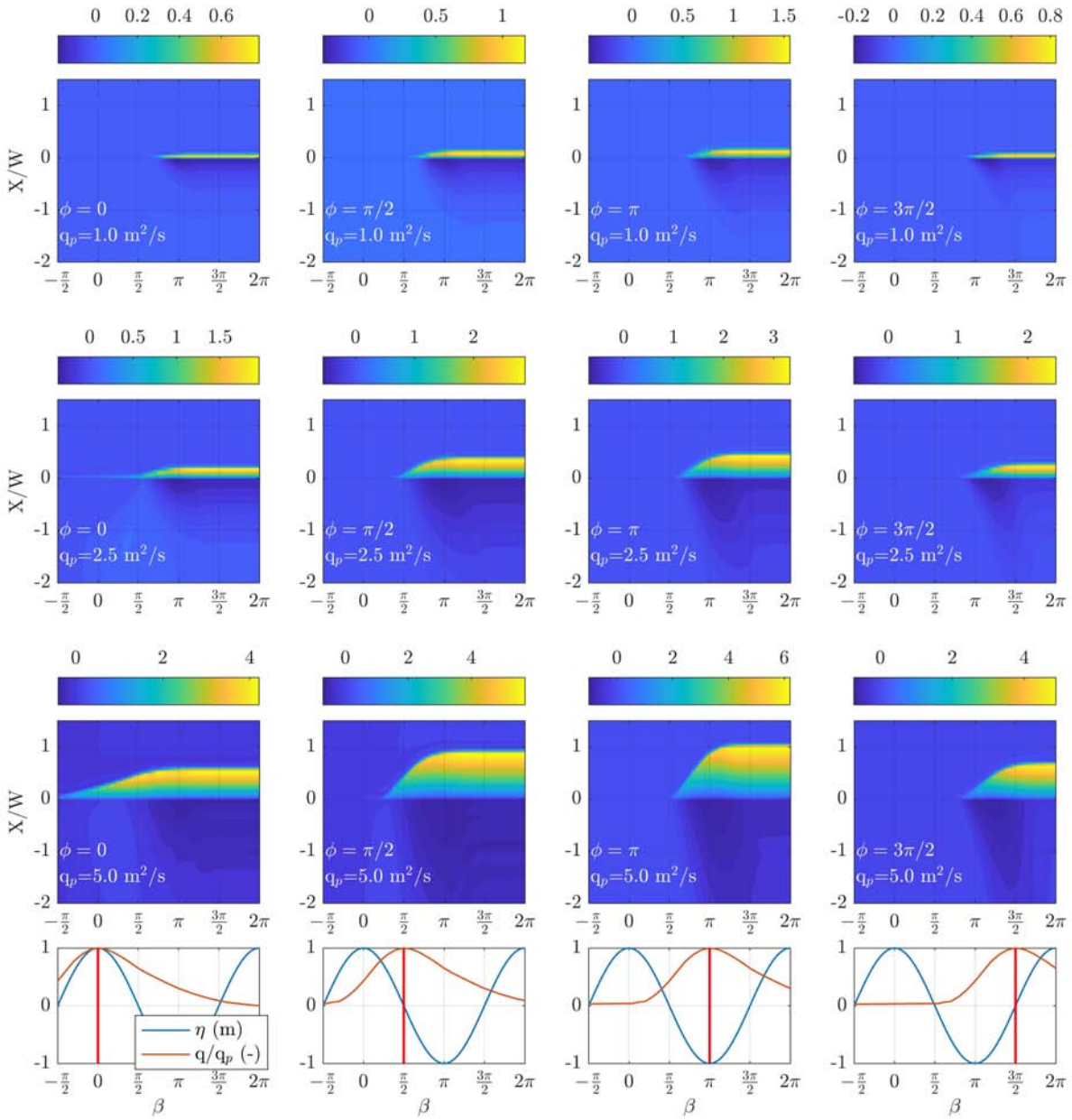


Figure 5.6.2: Time evolution of the bed level changes (m) along the stream axis ($Y = 0$) for the simulations in Table 6.2.1, with columns and rows showing different $\phi$ and $q$ values, respectively. Positive (negative) values indicate accretion (erosion). Axes represent the non-dimensional length along the stream axis ($X/W$) and time in terms of the tidal cycle ($\beta$). The last row shows the offshore water level (blue) and the non-dimensional river discharge (red). Vertical red lines represent the instant for the peak river discharge at the upstream boundary.

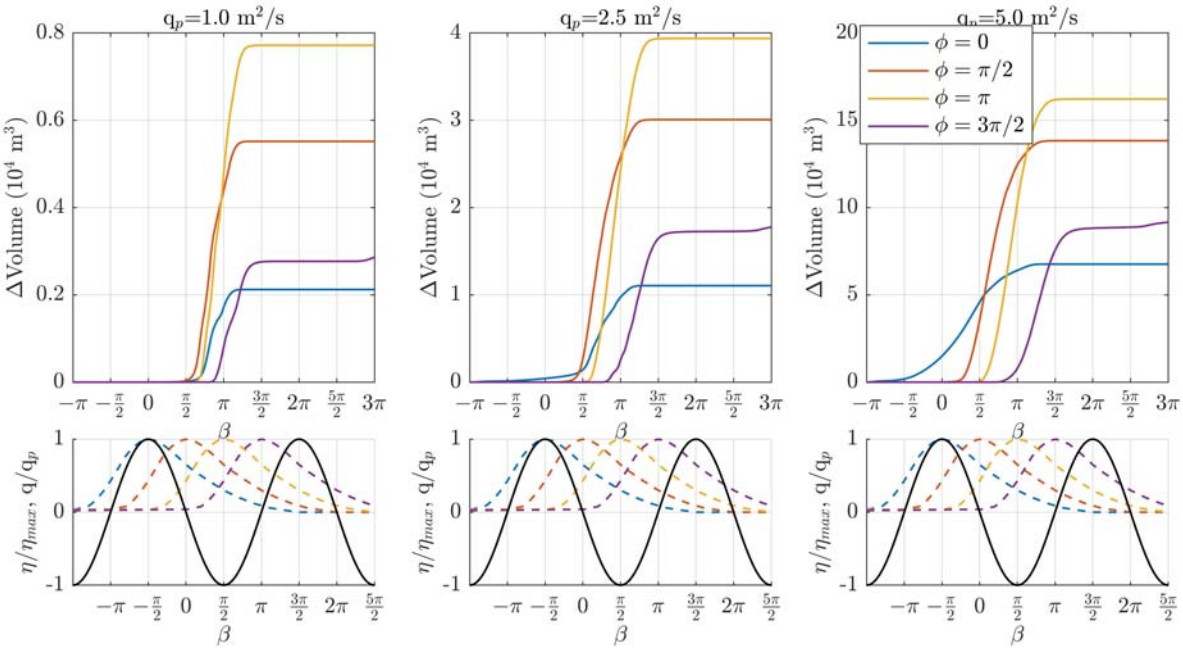


Figure 5.6.3: Time evolution of the river mouth bar sediment volumes for the simulations performed. The lower panels represent the non-dimensional hydrographs and the offshore water levels.

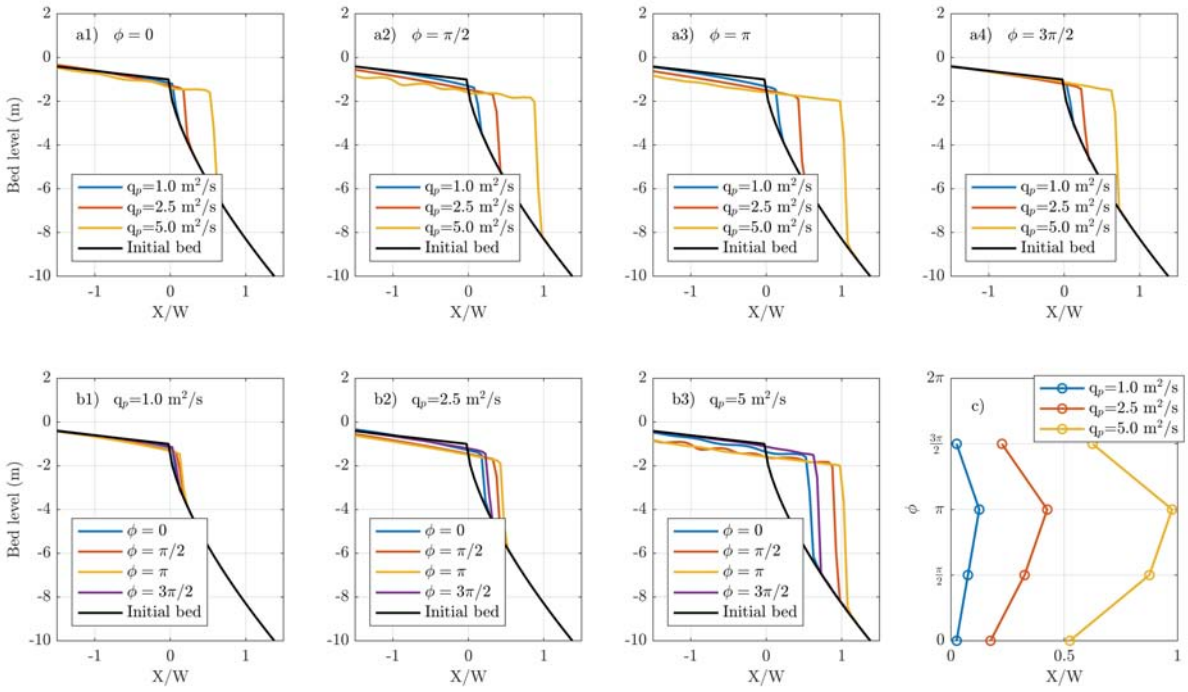


Figure 5.6.4: Final bed level profiles obtained along the stream axis for all the tested combinations of lag $\phi$ and peak river discharges $q_p$. Panel c) shows the final cross-shore position of the bar crests

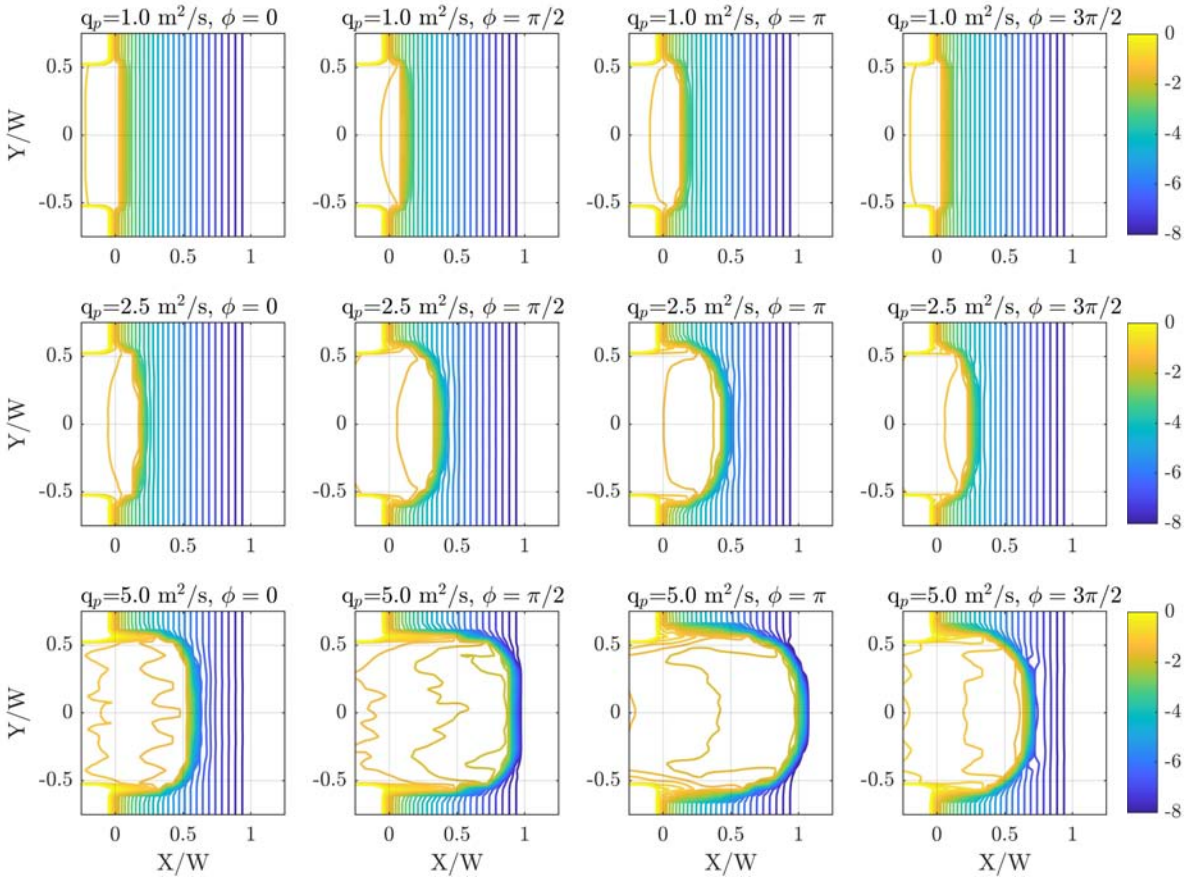


Figure 5.6.5: Bathymetric contour maps of the nearshore area modeled with Delft3D. Colors indicate the bed level (m) at the end of the simulations. First, second and third rows correspond to $q_p$ = 1.0, 2.5, and 5 m$^2$/s, respectively, whereas first, second, third and fourth columns correspond to $\phi = 0$, $\pi/2$, $\pi$ and $3\pi/2$, respectively.

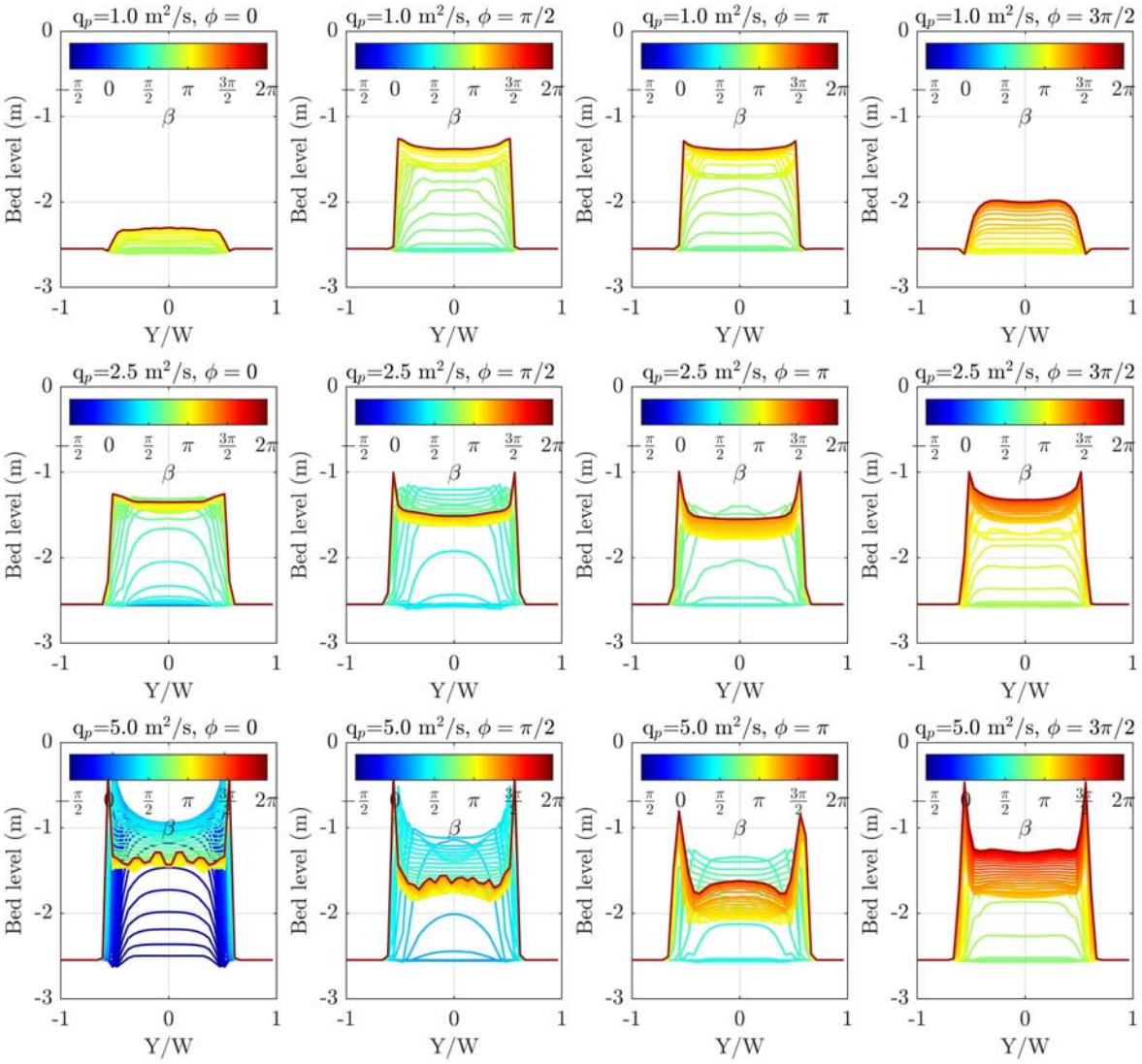


Figure 5.6.6: Time evolution of the longshore profile of the bathymetry at $X/W \simeq 0.1$. Colors indicate non-dimensional time $\beta$.

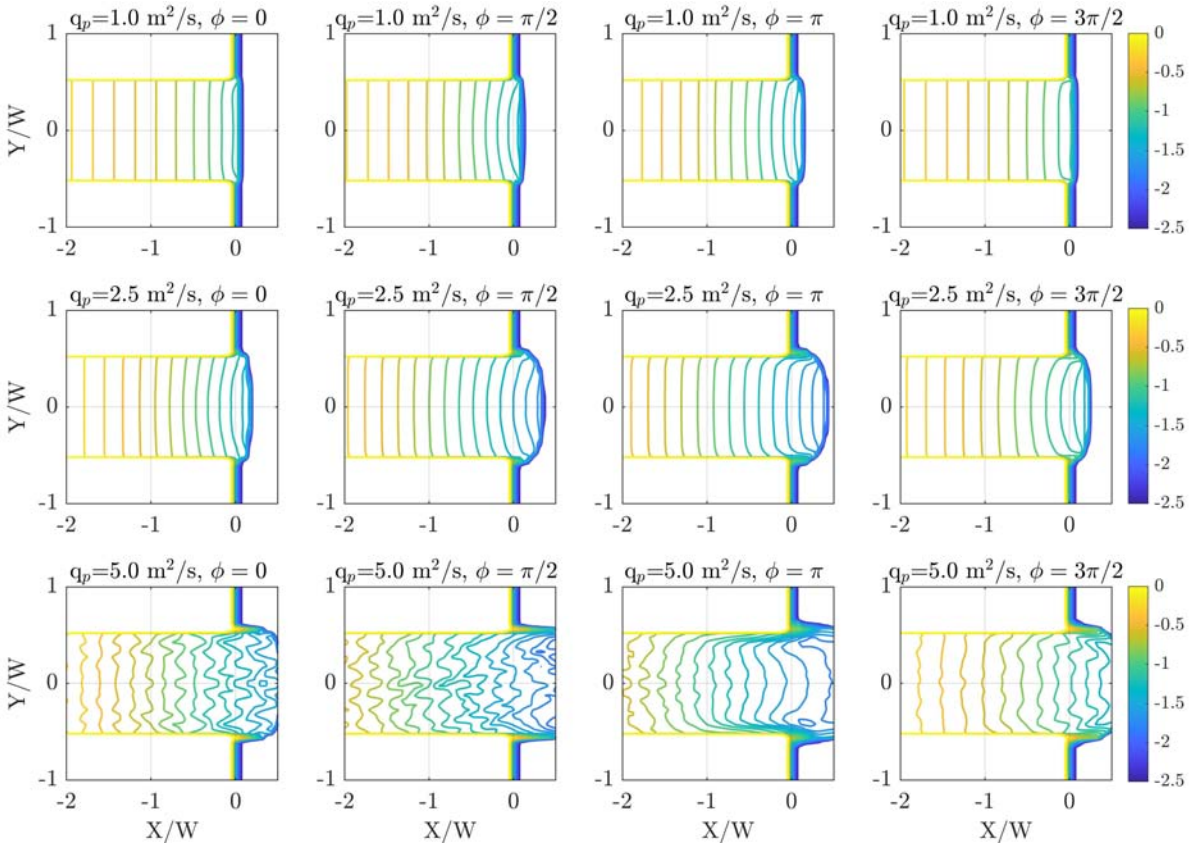


Figure 5.6.7: Bathymetric contour maps of the downstream stretch of the river area modeled with Delft3D. Colors indicate the bed level (m) at the end of the simulations. First, second and third rows correspond to $q_p$ = 1.0, 2.5, and 5 m$^2$/s, respectively, whereas first, second, third and fourth columns correspond to $\phi = 0$, $\pi/2$, $\pi$ and $3\pi/2$, respectively.

CHAPTER 6

# FLOOD HAZARD MAPPING IN RIVER MOUTHS: THE EFFECT OF THE PHASE LAG BETWEEN TIDES AND RIVER DISCHARGES AND THE RIVER BAR FORMATION

The hazard assessment during flood episodes is more challenging at river mouths due to the complexity of the interactions between the fluvial and marine dynamics. The aim of this chapter is to assess the role of i) the peak flow, ii) the phase difference between peak river discharge and high tide and iii) the morphodynamic changes produced during short-term extreme events on the delimitation of flood hazard areas in river mouth environments.

For this purpose, the same theoretical model is used as in the previous chapters, so that the analysis will be divided into two groups of simulations: i) no morphodynamic changes during the simulations for different phase differences and peak flows; and (ii) the bed evolution during the simulations for a specific peak discharge and different phase differences. This chapter is based on Ruiz-Reina and López-Ruiz (2022).

## 6.1 Introduction

The delimitation of flood areas and associated hazard maps are of great interest for river and coastal The delimitation of flood areas and associated hazard maps are of great interest for river and coastal flood risk management. As discussed in the previous chapters, river mouths are transitional environments between rivers and oceans with complex behaviour due to the superposition of multiple processes induced by concomitant maritime, fluvial, and atmospheric agents ((Fagherazzi et al., 2015; Leonardi, Kolker, and Fagherazzi, 2015), where river discharges contribute to develop deltas and river mouth bars ((Jiménez-Robles, Ortega-Sánchez, and Losada, 2016)).

With regard to the effect of tides, they have been analysed and identified as a key factor in the control of river mouth dynamics, but there are still some aspects of the interaction between tidal hydrodynamics and river flow that require deeper knowledge and research. As a result,

previous chapters have focused on the study of the effect of the time lag between the tide and the maximum (peak) river discharge on the formation and evolution during an extreme event, using a methodology based on numerical modelling. However, this study lacked: i) the analysis of the hazard vulnerability conditions during the tidal cycle as a consequence of the time lag between the peak river flow and the high tide, ii) the completion of this analysis including the effect of the bar formation at the outlet and iii) the evaluation of the role of the peak flow in these processes and its influence on the hazard classification at the river mouth.

The identification of potential flood hazard areas for personal injury and property damage typically involves the analysis of two hydrodynamic variables: water depth and velocity. A third parameter, which is the product of the two, is also considered. This parameter is more representative of the hazardous conditions of a site as it combines both factors, making its analysis particularly relevant. This chapter analyses three main variables and their influence on the aforementioned hazard parameters (i.e. depth, velocity, $d \cdot v$): the unit peak discharge ($q_p$), the phase difference between this peak discharge and the high tide ($\phi$) and the presence of the river mouth bar. Theoretical simulations, similar to those in previous chapters, are carried out to analyse the effect of each variable independently.

## 6.2 Numerical simulations

The simulations performed are based on the same physical scenario, equations and numerical model as those used in the previous Chapter. The only modification made was to suppress the morphodynamic changes (no bathymetry update) in order to independently analyze the effect of the phase difference $\phi$. Table 6.2.1 shows a summary of the considered simulations.

## 6.3 Results

In order to facilitate the interpretation of the results for the hazard assessment, they are presented in such a way that the effect of the three variables considered can be appreciated: the river flow in terms of unit discharge ($q_p$), the phase difference between this peak discharge and the high tide ($\phi$) and the presence of the river mouth bar. The figures analysed in the following paragraphs have the following structure: i) each panel shows the results obtained for a specific $q_p$, ii) the results of the hydrodynamic simulations for the water depth along the river axis are shown in the first row, the velocity in the second row and the product of depth and velocity ($d \cdot v$) in the third row as a representative parameter of flood hazard, and iii) the fourth panel corresponds to the case with $q_p = 2.5 m^2/s$ and morphodynamic changes. The results are therefore presented in a similar way to Chapter 5. The x-axis represents time in terms of the tidal phase ($\beta$), while the y-axis represents the dimensionless distance along the river axis with the river mouth width $W$, with positive values corresponding to the nearshore area. For the time scheme, $\beta = \pi$ represents half of the tidal cycle starting at $\beta = 0$. The origin ($X/W = 0$) is at the mouth of the river. The columns in the figure represent different values of the lag ($\phi$). The last row represents the lag between the peak discharge (vertical red line) and the tidal cycle. Dashed white lines are shown as contours to better visualise the results.

The first set of plots (Fig. 6.3.1) corresponds to the case with the lowest river discharge ($q_p = 1.0 m^2/s$). The influence of the tide is clearly observed in the hydrodynamic variables along

| Simulation ID | $q_p$ ($m^2$/s) | $\phi$ (-) | Tidal level | Bed change |
|---|---|---|---|---|
| 01-hyd | 1.0 | 0 | HT | No |
| 02-hyd | 1.0 | $\pi/2$ | MLT | No |
| 03-hyd | 1.0 | $\pi$ | LT | No |
| 04-hyd | 1.0 | $3\pi/2$ | MHT | No |
| 05-hyd | 2.5 | 0 | HT | No |
| 06-hyd | 2.5 | $\pi/2$ | MLT | No |
| 07-hyd | 2.5 | $\pi$ | LT | No |
| 08-hyd | 2.5 | $3\pi/2$ | MHT | No |
| 09-hyd | 5.0 | 0 | HT | No |
| 10-hyd | 5.0 | $\pi/2$ | MLT | No |
| 11-hyd | 5.0 | $\pi$ | LT | No |
| 12-hyd | 5.0 | $3\pi/2$ | MHT | No |
| 05-mor | 2.5 | 0 | HT | Yes |
| 06-mor | 2.5 | $\pi/2$ | MLT | Yes |
| 07-mor | 2.5 | $\pi$ | LT | Yes |
| 08-mor | 2.5 | $3\pi/2$ | MHT | Yes |

Table 6.2.1: Cases defined. First three set of simulations are dedicated to hydrodynamic analysis of the influence of $q_p$ and $\phi$. The fourth set, limited to a unique $q_p$, is focused on the role of the presence of the mouth bar.

the axis. Specifically, for the four values considered for $\phi$, the maximum depth in each case coincides with the high tide conditions. This result is only slightly modified by the river discharge at other times of the tidal cycle. An abrupt increase in water depth is observed along the coastline, apparently similar for all scenarios, as no bed change is considered in this set of simulations.

On the other hand, for velocities, the maximum values are at the times of the tidal cycle corresponding to low tide. For $\phi = 0$ there is a limited influence of river discharge. However, when both variables are combined (third row), the maximum values occur in the times corresponding to the peak of the river discharge, with the highest value occurring at the outlet during high tide and later ($\phi = \pi/2$, $\phi = 0$). This result again shows the complexity of the agent interactions that lead to the maximum values of the hydrodynamic variables at different times (depth at high tide, velocity coinciding with low tide). However, if the value that best represents the hazard is taken into account, it is in a range between high and low tide conditions.

Fig. (6.3.2) shows the results for $q_p = 2.5 m^2/s$, representative of a scenario where the hydrodynamics are the result of a balance between tide and river discharge. In this case, the water depths for the different lag scenarios are clearly influenced by the tide, with higher hydraulic depths at high tide than at low tide, and minor changes due to the river hydrograph associated with the peak discharge. More differences are observed for the along-channel flow, with the highest velocities associated with the low tide for all, even if the peak discharge occurs later ($\phi = 3\pi/2$). The velocity is clearly increased for $\phi = \pi$ because the peak discharge coincides with the low tide. Values of more than 4 m/s are observed at the mouth of the river.

However, for $d \cdot v$ the maximum values occur close to the instant of peak discharge, as in the

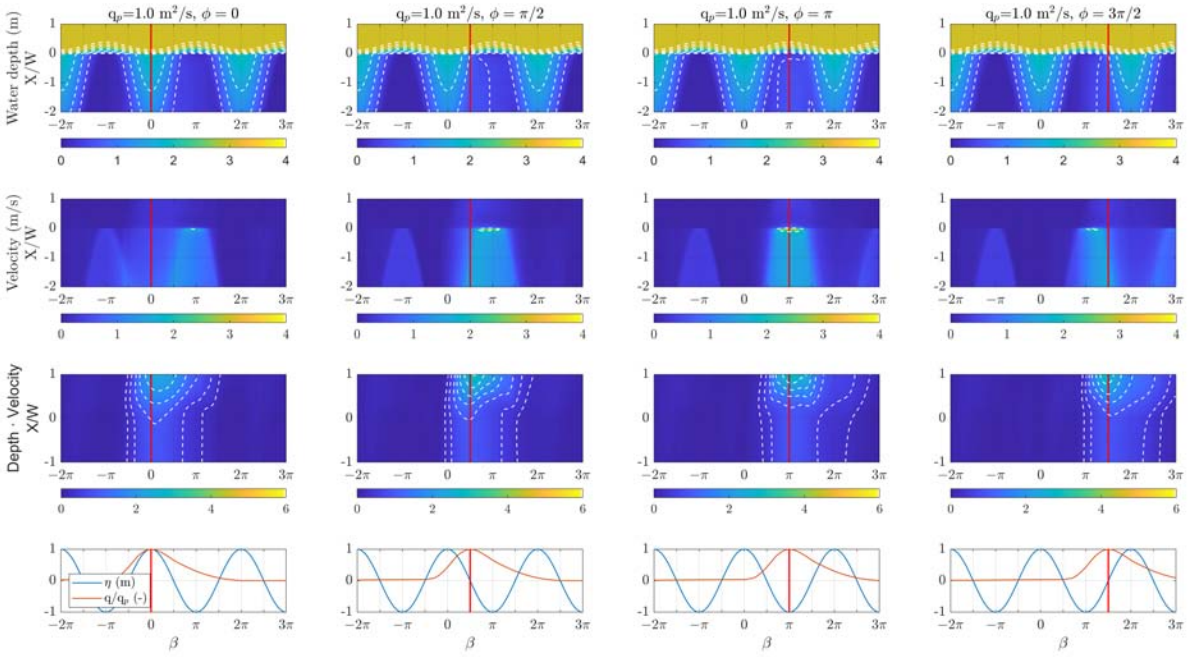


Figure 6.3.1: Results for simulations with $q_p = 1.0m^2/s$: time evolution of the water depth (first row), along-channel current (second row) and the product of them (third row) along the stream axis (Y=0) for hydrodynamic conditions, without morphodynamic evolution. The last row represents the offshore water level (blue) and the non-dimensional river discharge (orange). Vertical red lines indicate the instant for the peak river discharge.

case of $q_p = 1.0m^2/s$. For $\phi = 0$ and $\phi = \pi$, this coincidence is total, while for $\phi = \pi/2$ and $\phi = 3\pi/2$, this maximum is slightly ahead and delayed, respectively. On the other hand, for all lags, an abrupt increase of this parameter can be observed during the rising part of the hydrograph and a milder decrease during the falling part, as a copy of the hydrograph shape. In addition, the total period with values greater than 0.30 is around $2.5\pi$ for all.

The results presented in (Fig. 6.3.3) correspond to a fluvial influence with a unit discharge of $q_p = 5.0m^2/s$. In contrast to the previous results, the maximum depth values are no longer restricted to high tide, but are shifted in time depending on the peak discharge. The velocity analysis supports this trend, with maximum velocity values exceeding 4 m/s. The velocities are located at times associated with low tide, as in the previous simulations. However, they also extend over longer time intervals throughout the passage of the river discharge pulse. Therefore, the maximum values are influenced by both phenomena (low tide and peak flow) and the time interval with high velocities is extended. In addition, it can be observed that for $\phi = 3\pi/2$ the maximum velocity occurs before the peak of the hydrograph. The results of the combination of velocity and depth highlight the fluvial influence. The maximum values are associated with the peak flow and no relevant changes are observed due to the tidal cycle or the phase difference between the high tide and the river discharge. The time interval with high values for this parameter is prolonged mainly during the falling part of the hydrograph as a consequence of the higher discharge.

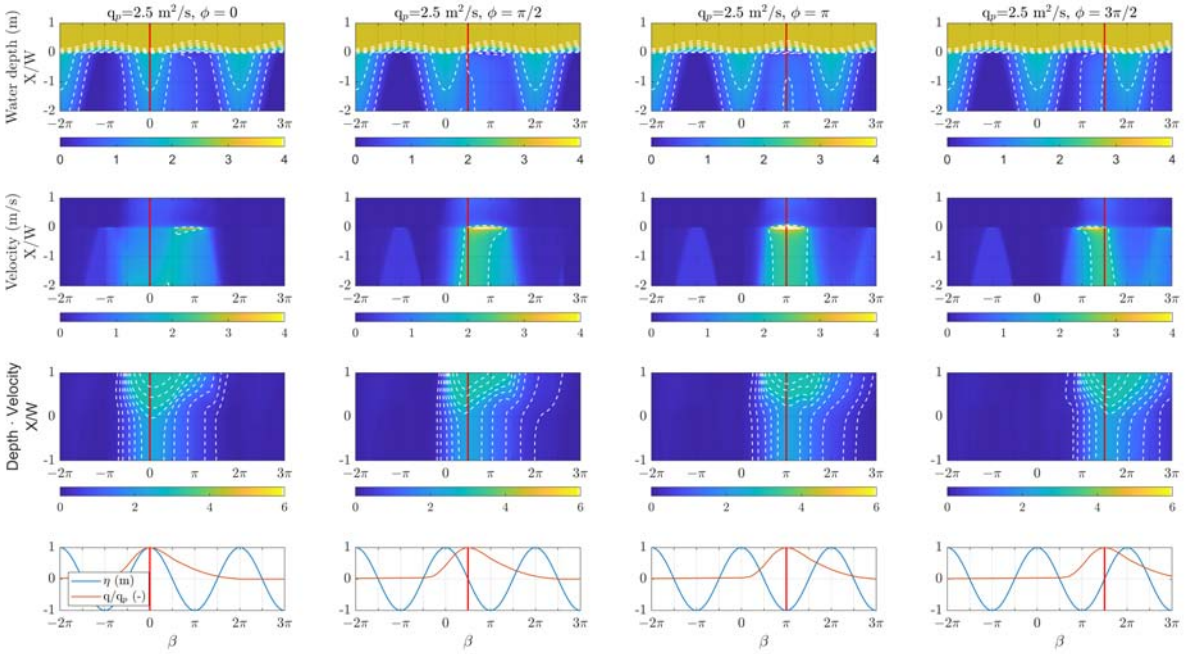


Figure 6.3.2: Results for simulations with $q_p = 2,5m^2/s$: time evolution of the water depth (first row), along-channel current (second row) and the product of them (third row) along the stream axis ($Y = 0$) for hydrodynamic conditions, without morphodynamic evolution. The last row represents the offshore water level (blue) and the non-dimensional river discharge (orange). Vertical red lines indicate the instant for the peak river discharge.

Therefore, the results show that the role of the tide is more significant in the results of the velocities, where it is clearly observed that the maximum values are located in the region of the low tide, especially for lower flows. On the other hand, the role of the peak discharge is clearly shown in the parameter $d \cdot v$, so that the maximum value of this variable is located around the moment of this peak.

Fig. (6.3.4) shows similar results for the set of simulations with morphodynamic changes at the bed level, focusing on the case with $q_p = 2.5m^2/s$. In this case the water depth shows significant variations for different lags ($\phi$). Specifically for $\phi = [\pi/2, \pi]$, the formation of the river mouth implies a decrease in water depth at the outlet and an advance in the location of the abrupt change in water depth in the nearshore area. Similarly to the previous set of scenarios, the maximum velocities are associated with low tide conditions. However, in these cases the development of the river bar leads to an increase in current at the outlet and maximum values of more than 3 m/s are found on the bar in the nearshore area for $\phi = \pi$.

With respect to the product of depth and velocity, the maximum value coincides with the peak discharge in all scenarios, except for $\phi = \pi$. In this case the maximum in the nearshore area is shifted to an instant between the high tide and the peak discharge. Furthermore, this product of depth and velocity shows an irregular behaviour in the nearshore area at a distance of $X/W = 0.5$, which coincides with the maximum distance reached by the bar evolution.

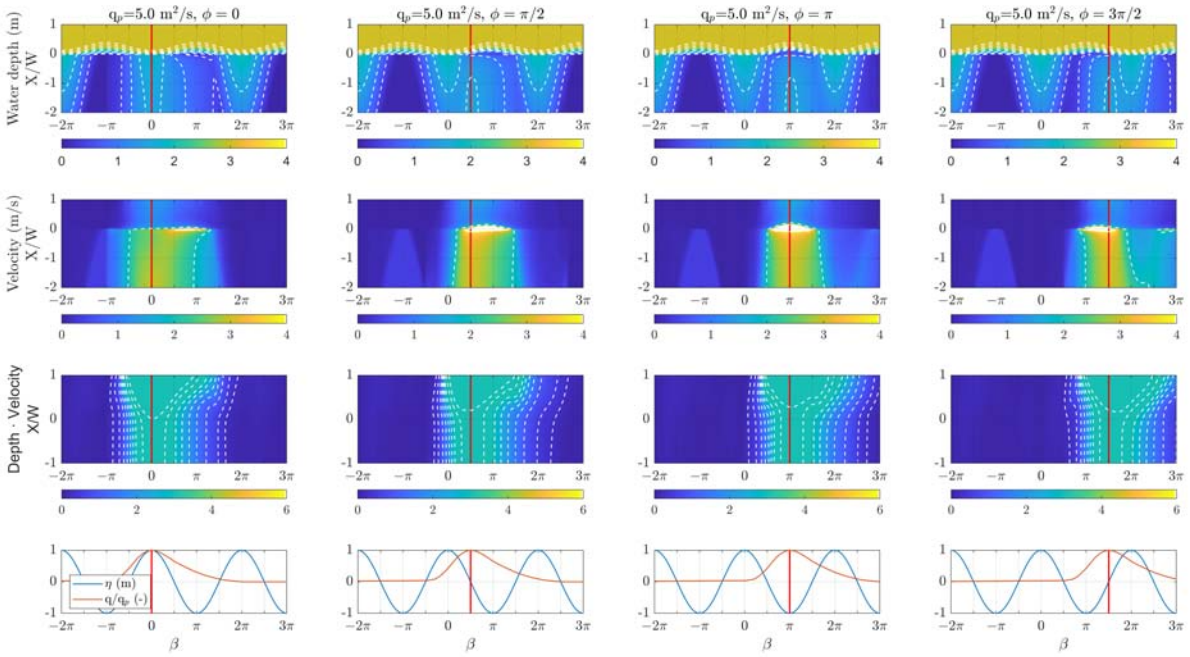


Figure 6.3.3: Results for simulations with $q_p = 5.0m^2/s$: time evolution of the water depth (first row), along-channel current (second row) and the product of them (third row) along the stream axis ($Y = 0$) for hydrodynamic conditions, without morphodynamic evolution. The last row represents the offshore water level (blue) and the non-dimensional river discharge (orange). Vertical red lines indicate the instant for the peak river discharge.

## 6.4 Discussion

The previous results for simulations with and without bathymetry update show that the different time lag between the peak discharge and the tide leads to significant changes in the hydrodynamic behaviour. These differences are more pronounced for the second set of simulations because of the formation of the river mouth bar, which implies a bed modification around the outlet that modifies the magnitude of velocity and water depth.

However, the flood hazard is typically analysed by the third parameter, the product of depth and velocity (Planning and Environment, 2023). Fast flowing shallow or deep water can sweep away people and vehicles, or even undermine structures or destroy elements of buildings and infrastructure. Accordingly, the previous results show a wide range of this parameter during the occurrence of the whole hydrograph along the river, with values from 0.25 to 2.5 in the river and up to 8.0 in the nearshore area within a dimensionless distance lower than $X/W = 0.5$ for $q_p = 5.0m^2/s$.

For a deeper analysis of these results, the relative vulnerability of people and built assets to flood hazards can be assessed using the depth and velocity thresholds defined by Planning and Environment (2023). Fig. (6.4.1) shows these thresholds, which relate to the stability of people and vehicles in floodwaters and to buildings affected by flooding. Using these categories, the following figures show the flood hazard classification for the numerical simulations performed.

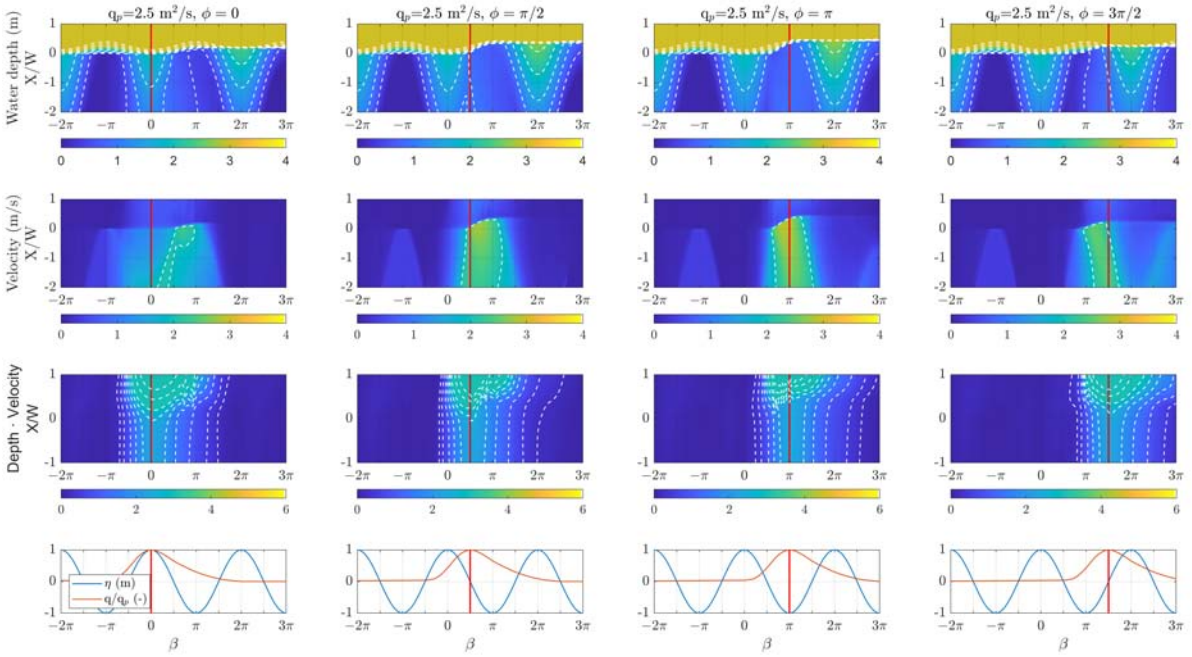


Figure 6.3.4: Results for simulations with $q_p = 2.5m^2/s$ considering bed level changes: time evolution of the water depth (first row), along-channel current (second row) and the product of them (third row) along the stream axis ($Y = 0$) for hydrodynamic conditions, without morphodynamic evolution. The last row represents the offshore water level (blue) and the non-dimensional river discharge (orange). Vertical red lines indicate the instant for the peak river discharge.

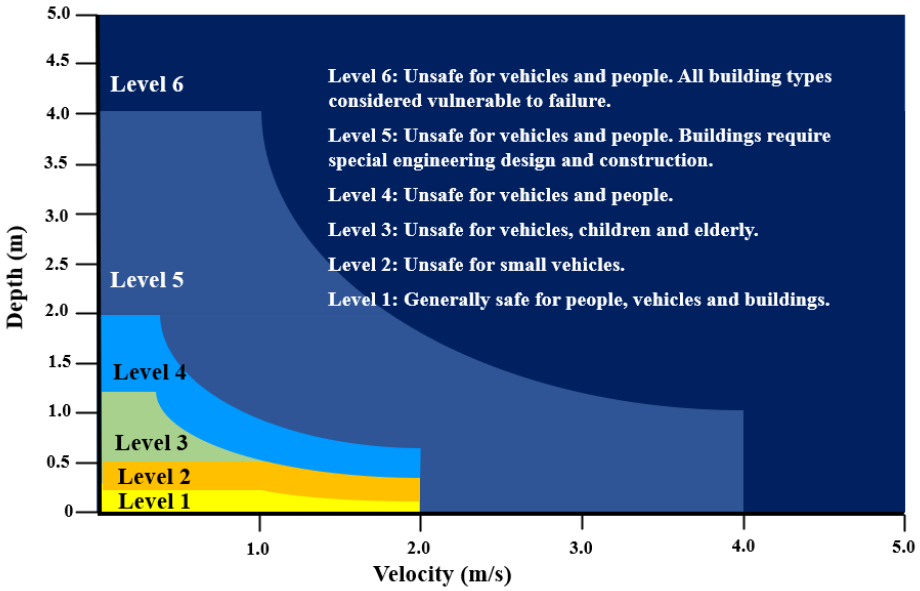


Figure 6.4.1: General flood hazard vulnerability curve (Department of Planning and Environment, State of New South Wales, Australia, 2013)

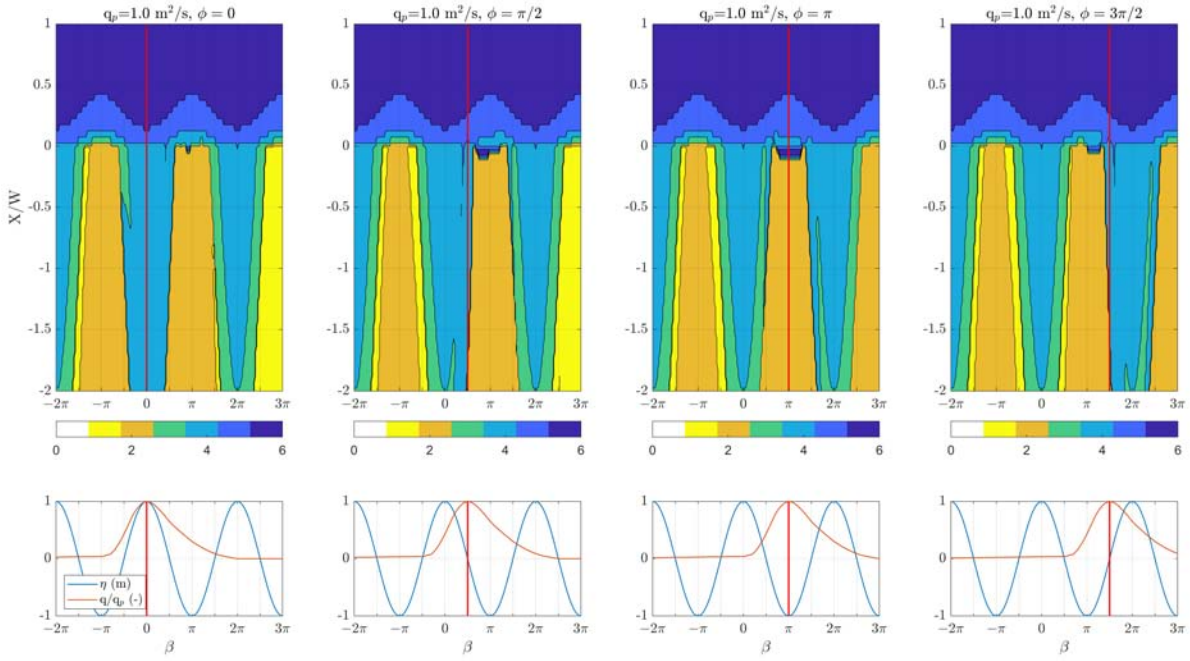


Figure 6.4.2: Flood hazard classification along the stream axis for $q_p = 1.0m^2/s$ and different phase differences.

The first set of plots (Fig. 6.4.2), corresponding to $q_p = 1.0m^2/s$, shows the hazard classification at each point of the river and at each time during the tidal cycle. The most dangerous category is restricted to the nearshore area with the highest hydraulic depths. If the analysis is restricted to the river channel, a significant influence of the tide can be observed. The highest hazard categories (level 4) occur at high tide, regardless of the time of peak flow. The lowest hazard categories (level 1) occur at low tide. In this classification, the effect of river discharge is negligible, except for the occasional increase in hazard at the mouth at low tide for $\phi = \pi/2$ and $\phi = 3\pi/2$.

In the case of $q_p = 2.5m^2/s$, the interaction of peak discharge and tidal conditions leads to a more complex classification of hazard levels. The peak discharge instant is associated with unsafe hazard categories (level 5) along the stream. Safer categories (level 2) are placed along the axis for those intervals during low tide that do not affect the river discharge. At high tide the water depth is greater and unsafe categories appear along the stream. For $\phi = [\pi/2, \pi, 3\pi/2]$, more dangerous categories are found during the time interval in coincidence with the influence of the river flow due to the superposition at low tide conditions, especially near the river mouth due to an increase in velocity (level 6).

An increase in discharge up to $q_p = 5.0m^2/s$ results in a decreasing influence of the tidal cycle (Fig. 6.4.4). The interval time of the hydrograph duration is clearly observed in connection with the more dangerous categories (levels 5 and 6), while the influence of the tide is reduced within this period. The small influence can be observed as an extension of the most dangerous category (level 6) around the mouth in coincidence with low tide conditions for each simulation. The peak flow is so high during the rising and falling parts of the hydrograph that, in combination with low tide, it leads to an increase in hazard.

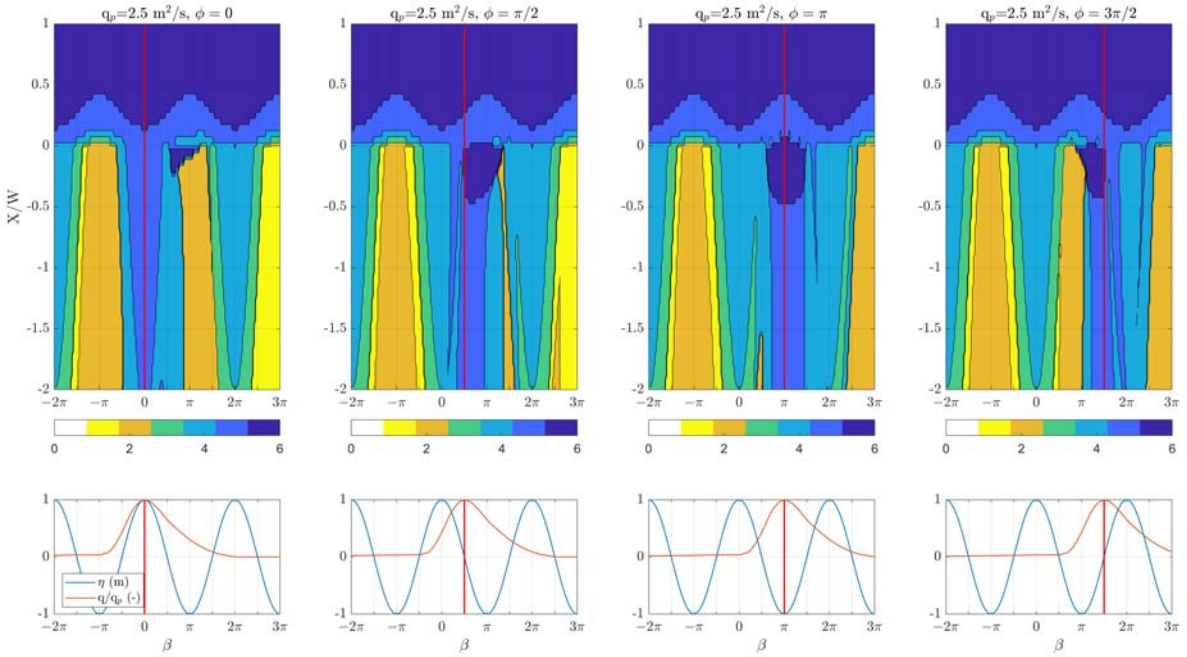


Figure 6.4.3: Flood hazard classification along the stream axis for $q_p = 2.5m^2/s$ and different phase differences.

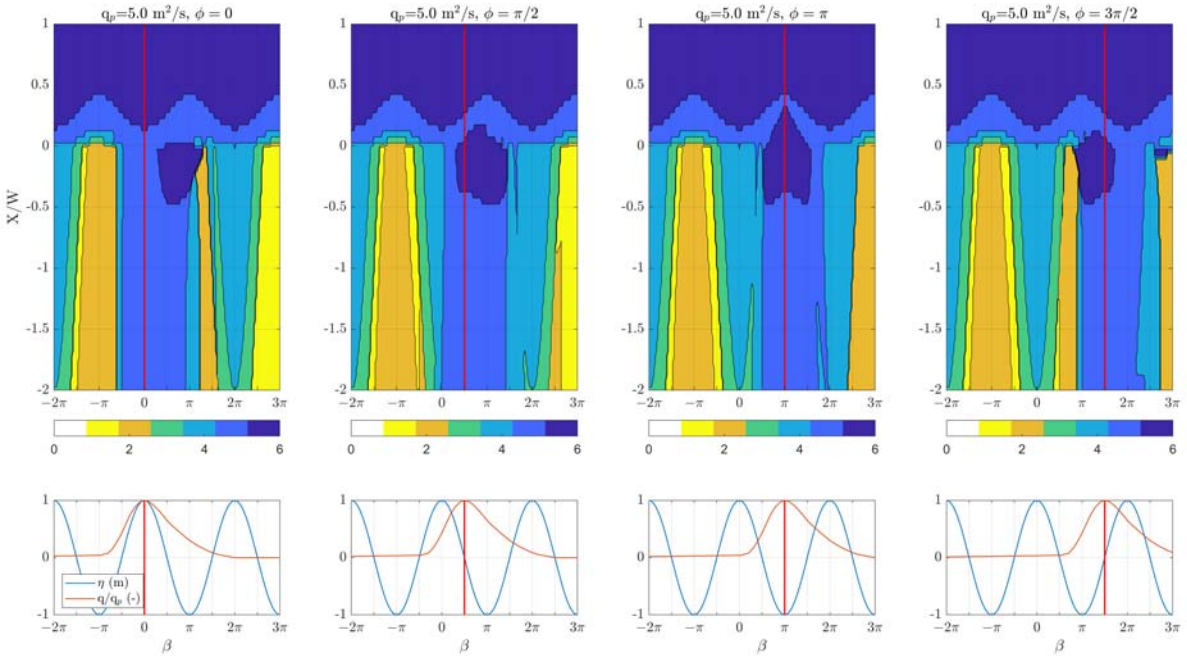


Figure 6.4.4: Flood hazard classification along the stream axis for $q_p = 5.0m^2/s$ and different phase differences.

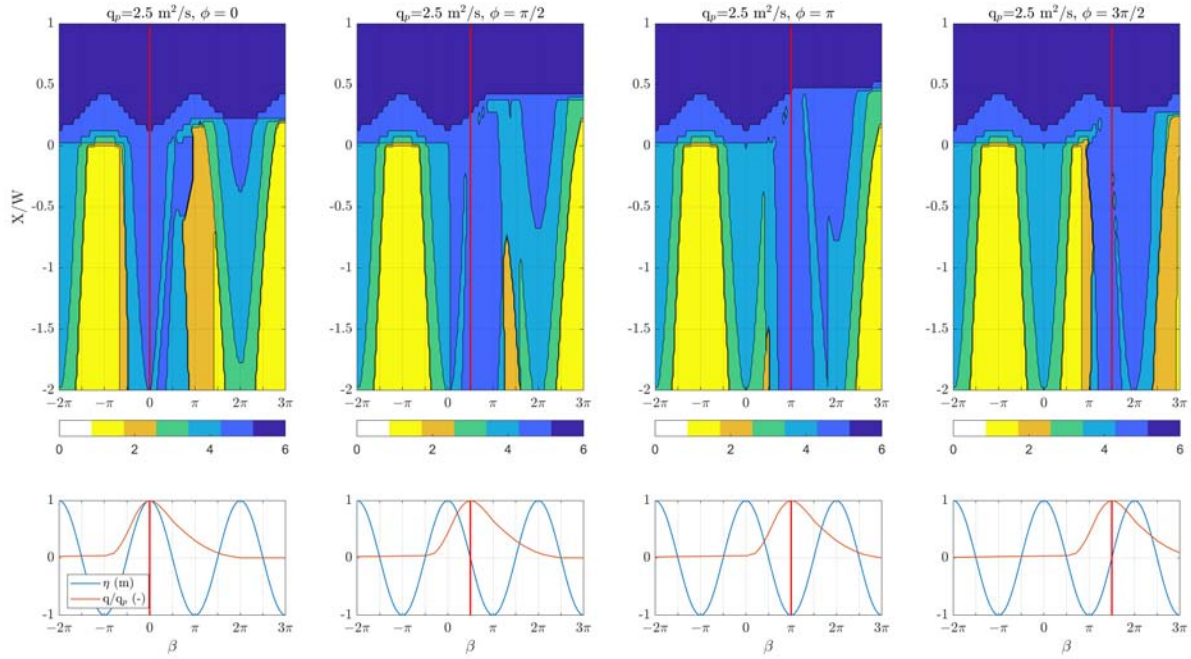


Figure 6.4.5: Flood hazard classification along the stream axis for $q_p = 2.5m^2/s$ and different phase differences, including morphodynamic bed changes.

Looking at the last set of simulations (6.4.5), similar conclusions can be drawn as in Fig. 6.4.3. The safest category is observed for low tide conditions when there is no coincident river discharge; the distribution of hazard categories is a function of the time lag between the peak river discharge and the tide; and for $\phi = \pi$, the river hydrograph interval leads to hazardous categories.

A final comparison of both sets of simulations with $q_p = 2.5m^2/s$ leads to the observation of significant differences around the river mouth. For $\phi = 0$, several different categories are observed in the falling part of the hydrograph due to the variations in velocity along the stream and the formation of river bars at the outlet. For $\phi = \pi/2$, again minor differences are observed during the falling part of the hydrograph along the axis, but they are more pronounced in the nearshore area at a distance $X/W < 0.5$ due to the bar formation. However, for or $\phi = 3\pi/2$ these differences are not observed. Finally, for $\phi = \pi$, an extension of the hazard classification areas in the nearshore can be observed as a consequence of the river mouth bar. And the maximum category reached is level 5, lower than that observed without the presence of the bar (level 6). This result is a consequence of the reduction of the velocity around the mouth due to the morphodynamic bed change.

**Final remarks**

This chapter aims to shed some light on flood hazard mapping in river mouths and the influence of key factors: i) the peak flow of the river discharge, ii) the phase difference between this peak flow and the high tide, and iii) the morphodynamic changes produced during short-term extreme events.

The main factor that dominates the delineation of risk zones is the peak flow. For low flows, the tidal influence increases and the hazard conditions are greater during periods of high tide. For intermediate flows, there is a combined influence of river discharge and tide, so that the most hazardous conditions occur when peak flow and low tide coincide. In the case of high flows, the hazard zones are determined by the river hydrograph and the influence of the tides is significantly reduced, being limited to increasing the hazard conditions in the area of the estuary during the coincidence of low tide and peak flow. The presence of a bar modifies the classification of the hazard zones around the estuary and slightly reduces the maximum category, especially for the coincidence of peak flow and low tide.

These results highlight the complexity of the processes that occur in a river mouth and the need to analyse the entire tidal cycle in order to accurately determine the hazard conditions in this environment during an extreme event.

CHAPTER 7

# CONCLUDING REMARKS

River mouths and deltas are areas of great ecological and socio-economic interest, containing some of the world's most valuable ecosystems and densely populated areas. This has led to the development of important industrial and agricultural areas, which often require inland waterways along the river courses that feed these mouths. The processes of transport and mixing of nutrients, salinity and sediments in these environments are very important for the biogeochemical evolution of many riverine and marine ecosystems, as well as for the formation of morphologies such as bars and deltas. The development of these features generally follows sediment deposition, which can occur through natural levee growth and channel elongation, or through deposition and vertical aggradation of estuarine bars. In addition, both river mouths and deltas are subject to extreme flooding events caused by river discharge, storm surge or a combination of both. The management of these extreme events is becoming increasingly challenging due to changes in their frequency and intensity caused by climate change. Improving knowledge of the dynamics of river mouths is therefore fundamental to their fate, both from an environmental and socio-economic perspective.

In this context, the main aim this dissertation is to analyse the hydrodynamics and morphodynamics of river mouths during extreme river discharge events in order to characterise the role played by: (1) the geometry of the channel, outlet and nearshore; (2) the temporal variation of the river discharge conditions; and (3) the temporal variation of the sea level due to the tidal effect. The analysis is carried out using a process-based numerical model (Delft3D) on idealised outlets whose geometric and physical parameters are based on those of the Andalusian Mediterranean coast, where management problems have been identified during flood events. The results obtained represent an important step forward in the knowledge of the hydro-morphodynamics of river mouths and deltas and are directly applicable to coastal managers and policy makers involved in coastal flood management.

The most important conclusions of the Thesis are summarised below in response to the specific objectives set out in Chapter 1:

1. To precisely define the area in which both fluvial and marine agents determine the hydrodynamics of outlets, and therefore the area in which it is necessary to analyse their joint effect for flood management.

   The location of the fluvial/marine frontier is closely related to river slope, river roughness and tidal conditions. A non-dimensional curve for the position of the frontier within a tidal cycle was constructed based on the determination of two representative parameters, and two experimental expressions are proposed for their practical calculation. According to the analysis, the river gradient emerges as the most important factor in determining the extent of the marine influence, with the bed roughness (i.e. vegetation, river conservation conditions) and the discharge/tidal conditions being particularly relevant for low values of the river gradient.

2. To study, by means of numerical modelling, how the outlet and nearshore geometries may determine the hydrodynamics of the river mouths and, in particular, the jet structure.

   The outlet geometry determines the jet structure, with the shallower and wider outlets having two velocity peaks on the sides of the jet instead of a single maximum in the centre. For outlets where the nearshore profile is horizontal, the extent of the ZOFE region increases significantly and the jet expands after leaving the outlet geometry, whereas for non-horizontal geometries the jet initially contracts. In addition, the hydrodynamics at the mouth are clearly friction dominated for this horizontal nearshore geometry. However, for sloping and elliptical profiles, inertial and barotropic accelerations significantly increase their role in the vicinity of the outlet.

3. Extend the previous analysis to analyse the role of extreme river discharge events and the tide in the hydrodynamics, especially for basins where the discharge hydrograph has a time scale of the same order as the tidal period.

   Transient conditions trigger significant changes in the river mouth hydrodynamics. For simulations with tides and constant river discharge the changes in velocity during the tidal cycle are up to 100%, while when transient river discharges are also included, the variability of the jet structure during the tidal cycle is very important, limiting the applicability of the analyses carried out for stationary conditions in tidal environments or with a variable hydrological regime. This variability causes the position of the boundary between the ZOFE and ZOEF regions to vary greatly (up to 100%) depending on the time lag between the peak of the hydrograph and the tidal conditions.

   Furthermore, this phase and the time along the tidal cycle also determine the geometry of the transverse velocity profile. During low tide conditions, the extent of the ZOFE region increases and the velocity profile tends towards a profile with two lateral velocity peaks. During high tide conditions, a shorter extension of the ZOFE region and a velocity profile with a single maximum on the axis is observed. This is consistent with the literature analysing bar formation in equivalent estuaries. The results obtained in this work, which improve the understanding of the jet structure in river mouths, allow to gain insight into the complexity of the river-ocean interaction during extreme events and its effects on the morphodynamic evolution of river mouth bars and deltas.

4. To analyse the morphodynamic evolution of river mouths during extreme events such as those described in the previous section, for which the time lag between the peak of the hydrograph and the tidal level can potentially play a very important role.

The physical scenarios and numerical model implementation used, validated after a sensitivity analysis for grid scale effects, constitute an adequate tool to analyze the proposed problem. The analysis of the results obtained with this framework has demonstrated that the time lag between the maximum river discharge rate and the high tide plays a major role on the river mouth bar development and have to be considered in any short term river mouth hydro-morphodynamic analysis.

In particular, although the peak discharge rate $q_p$ is the major parameter controlling both the hydrodynamics and the morphodynamics of extreme discharge events, the time lag between this maximum rate and the high tide $\phi$ plays also a very important role on the water levels, currents, shear stresses, sediment transport and finally river mouth bar development. This role is more important as $q_p$ decreases.

Furthermore, despite of the value of the maximum flow velocities at the mouth is dominated by the maximum river discharge, the tidal conditions stand out as the key parameter controlling the instant when the maximum velocities are observed: as $q_p$ decreases, the maximum velocity of the mouth is advanced or retarded towards low tide causing a deformation of the velocity profile. This complex behavior of hydrodynamics, which may seem intuitive, is essential in the morphodynamic evolution of the mouth bar, determining the duration of its development and its final characteristics, doubling their final extension and quadrupling the final bar volume for the same river discharge conditions and different phase lag.

The results highlight the complex interaction between fluvial and coastal hydrodynamics, where the dominance of the latter leads to significant changes in current velocities and mouth evolution. The boundary for which tidal processes dominate is very diffuse. In the simulations performed, the influence of the tide at the instant when the highest velocities are obtained is clearly observed for $q_p \leq 2.5$ m$^2$/s but much less important for $q_p = 5.0$ m$^2$/s.

5. Following on from the previous points, which present a more theoretical approach, transfer the knowledge acquired to assess the impact of identified key parameters on flood hazard mapping and associated categories.

   The main factor that dominates the delineation of risk zones is peak flow. At low flows, the influence of the tide increases and the hazard conditions are greater during periods of high tide. For intermediate flows, there is a combined influence of river discharge and tide, so that the most hazardous conditions occur when peak flow and low tide coincide. In the case of high flows, the hazard zones are determined by the river hydrograph and the influence of the tides is significantly reduced, being limited to increasing the hazard conditions in the area of the mouth during the coincidence of low tide and peak flow. The presence of an estuary bar modifies the classification of the hazard zones around the mouth and slightly reduces the maximum category, especially for the coincidence of peak flow and low tide.

   These results highlight the complexity of the processes that occur in a river mouth and the need to analyse the entire tidal cycle in order to accurately determine the hazard conditions in this environment during an extreme event.

# BIBLIOGRAPHY


Abramovich, G. and Schindel, L. (1963). *The theory of turbulent jets*. MIT-Press. ISBN: 9780262310703.

Amores, A., Marcos, M., Carrió, D. S., and Gomez-Pujol, L. (2020). "Coastal impacts of Storm Gloria (January 2020) over the north-western Mediterranean". In: *Natural Hazards and Earth System Sciences* 20.7, pp. 1955–1968. ISSN: 16849981. DOI: 10.5194/nhess-20-1955-2020.

Anthony, E. J. (2015). "Wave influence in the construction, shaping and destruction of river deltas: A review". In: *Marine Geology* 361, pp. 53–78. ISSN: 00253227. DOI: 10.1016/j.margeo.2014.12.004.

Anthony, E. J., Marriner, N., and Morhange, C. (2014). "Human influence and the changing geomorphology of Mediterranean deltas and coasts over the last 6000 years: From progradation to destruction phase?" In: *Earth-Science Reviews* 139, pp. 336–361. ISSN: 00128252. DOI: 10.1016/j.earscirev.2014.10.003.

Besset, M., Anthony, E. J., and Bouchette, F. (2019). "Multi-decadal variations in delta shorelines and their relationship to river sediment supply: An assessment and review". In: *Earth-Science Reviews* 193.March, pp. 199–219. ISSN: 00128252. DOI: 10.1016/j.earscirev.2019.04.018.

Boudet, L., Sabatier, F., and Radakovitch, O. (2017). "Modelling of sediment transport pattern in the mouth of the Rhone delta: Role of storm and flood events". In: *Estuarine, Coastal and Shelf Science* 198, pp. 568–582. ISSN: 02727714. DOI: 10.1016/j.ecss.2016.10.004.

Bristow, C. and Best, J. (Jan. 1993). "Braided rivers: Perspectives and problems". In: *Geological Society, London, Special Publications* 75, pp. 1–11. DOI: 10.1144/GSL.SP.1993.075.01.01.

Brocchini, M. et al. (2017). "Comparison between the wintertime and summertime dynamics of the Misa River estuary". In: *Marine Geology* 385, pp. 27–40. ISSN: 00253227. DOI: 10.1016/j.margeo.2016.12.005. URL: http://dx.doi.org/10.1016/j.margeo.2016.12.005.

Canestrelli, A., Nardin, W., Edmonds, D., Fagherazzi, S., and Slingerland, R. (2014). "Importance of frictional effects and jet instability on the morphodynamics of river mouth bars and levees". In: *Journal of Geophysical Research: Oceans* 119.1, pp. 509–522. ISSN: 21699291.

Cao, Y., Zhang, W., Zhu, Y., Ji, X., Xu, Y., Wu, Y., and Hoitink, A. J. (2020). "Impact of trends in river discharge and ocean tides on water level dynamics in the Pearl River Delta". In: *Coastal Engineering* 157.January 2019, p. 103634. ISSN: 03783839. DOI: 10.1016/j.coastaleng.2020.103634.

Chatanantavet, P and Lamb, M. (2014). "Sediment transport and topographic evolution of a coupled river and river-plume system: An experimental and numerical study". In: *Journal of Geophysical Research: Earth Surface* 119.Figure 1, pp. 1263–1282. ISSN: 21699003.

Chow, V. T., Maidment, D., and Mays, L. (1988). *Applied Hydrology*. McGraw-Hill international editions. McGraw-Hill. ISBN: 9780070108103.

D'Alpaos, A., Lanzoni, S., Marani, M., and Rinaldo, A. (2010). "On the tidal prism–channel area relations". In: *Journal of Geophysical Research* 115.F1, F01003. ISSN: 0148-0227. DOI: 10.1029/2008JF001243.

Dalrymple, R. W. and Choi, K. (2007). "Morphologic and facies trends through the fluvial-marine transition in tide-dominated depositional systems: A schematic framework for environmental and sequence-stratigraphic interpretation". In: *Earth-Science Reviews* 81.3-4, pp. 135–174. ISSN: 00128252. DOI: 10.1016/j.earscirev.2006.10.002.

Dayan, U., Nissen, K., and Ulbrich, U. (2015). "Review Article: Atmospheric conditions inducing extreme precipitation over the eastern and western Mediterranean". In: *Natural Hazards and Earth System Sciences* 15.11, pp. 2525–2544. ISSN: 16849981. DOI: 10.5194/nhess-15-2525-2015.

Dean, R. and Dalrymple, R. (2004). *Coastal Processes with Engineering Applications*. Cambridge University Press. ISBN: 0-521-49535-0.

Del-Rosal-Salido, J., Folgueras, P., Bermúdez, M., Ortega-Sánchez, M., and Losada, M. A. (2021). "Flood management challenges in transitional environments: assessing the effects of sea-level rise on compound flooding in the 21st century". In: *Coastal Engineering*, p. 103872. ISSN: 0378-3839. DOI: https://doi.org/10.1016/j.coastaleng.2021.103872. URL: https://www.sciencedirect.com/science/article/pii/S0378383921000326.

Del-Rosal-Salido, J., Folgueras, P., Ortega-Sánchez, M., and Losada, M. A. (2019). "Beyond flood probability assessment: An integrated approach for characterizing extreme water levels along transitional environments". In: *Coastal Engineering* 152, p. 103512. ISSN: 0378-3839. DOI: https://doi.org/10.1016/j.coastaleng.2019.103512. URL: https://www.sciencedirect.com/science/article/pii/S037838391830454X.

Edmonds, D. A. and Slingerland, R. L. (2007). "Mechanics of river mouth bar formation: Implications for the morphodynamics of delta distributary networks". In: *Journal of Geophysical Research* 112.F2, F02034. ISSN: 0148-0227. DOI: 10.1029/2006JF000574.

Ericson, J. P., Vörösmarty, C. J., Dingman, S. L., Ward, L. G., and Meybeck, M. (2006). "Effective sea-level rise and deltas: Causes of change and human dimension implications". In: *Global and Planetary Change* 50.1-2, pp. 63–82. ISSN: 09218181. DOI: 10.1016/j.gloplacha.2005.07.004.

Esposito, C. R., Georgiou, I. Y., and Kolker, A. S. (2013). "Hydrodynamic and geomorphic controls on mouth bar evolution". In: *Geophysical Research Letters* 40.8, pp. 1540–1545. ISSN: 00948276. DOI: 10.1002/grl.50333.

Fagherazzi, S. et al. (2015). "Dynamics of river mouth deposits". In: *Reviews of Geophysics* 53 (3), pp. 642–672. ISSN: 19449208. DOI: 10.1002/2014RG000451.

Fan, H., Huang, H., Zeng, T. Q., and Wang, K. (2006). "River mouth bar formation, riverbed aggradation and channel migration in the modern Huanghe (Yellow) River delta, China". In: *Geomorphology* 74.1, pp. 124–136. ISSN: 0169-555X. DOI: https://doi.org/10.1016/j.geomorph.2005.08.015. URL: https://www.sciencedirect.com/science/article/pii/S0169555X0500293X.

Fernandino, G., Elliff, C. I., and Silva, I. R. (2018). "Ecosystem-based management of coastal zones in face of climate change impacts: Challenges and inequalities". In: *Journal of Environmental Management* 215, pp. 32–39. ISSN: 10958630. DOI: 10.1016/j.jenvman.2018.03.034. URL: https://doi.org/10.1016/j.jenvman.2018.03.034.

Gao, W., Shao, D., Wang, Z. B., Nardin, W., Rajput, P., Yang, W., Sun, T., and Cui, B. (2019). "Long-term Cumulative Effects of Intra-annual Variability of Unsteady River Discharge on the Progradation of Delta Lobes: A Modeling Perspective". In: *Journal of Geophysical Research: Earth Surface*, pp. 1–14. ISSN: 21699003. DOI: 10.1029/2017JF004584.

Gao, W., Shao, D., Wang, Z. B., Nardin, W., Yang, W., Sun, T., and Cui, B. (2018). "Combined Effects of Unsteady River Discharges and Wave Conditions on River Mouth Bar Morphodynamics".

In: *Geophysical Research Letters* 45.23, pp. 12,903–12,911. ISSN: 19448007. DOI: 10.1029/2018GL080447.

Giosan, L., Donnelly, J. P., Vespremeanu, E., Bhattacharya, J. P., Olariu, C., and Buonaiuto, F. S. (2005). "River delta morphodynamics: examples from the Danube Delta". In: *SEPM Special Publication* 83, pp. 393–412. DOI: 10.2110/pec.05.83.0393.

Herdman, L., Erikson, L., and Barnard, P. (2018). "Storm Surge Propagation and Flooding in Small Tidal Rivers during Events of Mixed Coastal and Fluvial Influence". In: *Journal of Marine Science and Engineering* 6.4. ISSN: 2077-1312. DOI: 10.3390/jmse6040158. URL: https://www.mdpi.com/2077-1312/6/4/158.

Jiménez-Robles, A. M., Ortega-Sánchez, M., and Losada, M. A. (2016). "Effects of basin bottom slope on jet hydrodynamics and river mouth bar formation". In: *Journal of Geophysical Research: Earth Surface* 121.6, pp. 1110–1133. ISSN: 21699011. DOI: 10.1002/2016JF003871.

Jiménez-Robles, A. M. and Ortega-Sánchez, M. (2018). "Implications of River Discharge Angle and Basin Slope on Mouth Bar Morphology and Discharge Dynamics of Stable Jets". In: *Journal of Hydraulic Engineering* 144.9, pp. 1–9. ISSN: 19437900. DOI: 10.1061/(ASCE)HY.1943-7900.0001506.

Jirka, G. H. and Giger, M. (1992). "Plane turbulent jets in a bounded fluid layer". In: *Journal of Fluid Mechanics* 241 (28), pp. 587–614. ISSN: 14697645. DOI: 10.1017/S0022112092002167.

Lageweg, W. I. van de and Feldman, H. (2018). "Process-based modelling of morphodynamics and bar architecture in confined basins with fluvial and tidal currents". In: *Marine Geology* 398.December 2016, pp. 35–47. ISSN: 00253227. DOI: 10.1016/j.margeo.2018.01.002.

Lamb, M. P., Nittrouer, J. A., Mohrig, D., and Shaw, J. (2012). "Backwater and river plume controls on scour upstream of river mouths: Implications for fluvio-deltaic morphodynamics". In: *Journal of Geophysical Research: Earth Surface* 117.1, pp. 1–16. ISSN: 21699011.

Lee, C., Hwang, S., Do, K., and Son, S. (2019). "Increasing flood risk due to river runoff in the estuarine area during a storm landfall". In: *Estuarine, Coastal and Shelf Science* 221, pp. 104–118. ISSN: 0272-7714. DOI: https://doi.org/10.1016/j.ecss.2019.03.021. URL: https://www.sciencedirect.com/science/article/pii/S0272771418308618.

Leijnse, T., van Ormondt, M., Nederhoff, K., and van Dongeren, A. (2021). "Modeling compound flooding in coastal systems using a computationally efficient reduced-physics solver: Including fluvial, pluvial, tidal, wind- and wave-driven processes". In: *Coastal Engineering* 163, p. 103796. ISSN: 0378-3839. DOI: https://doi.org/10.1016/j.coastaleng.2020.103796. URL: https://www.sciencedirect.com/science/article/pii/S0378383920304828.

Leonardi, N., Canestrelli, A., Sun, T., and Fagherazzi, S. (2013). "Effect of tides on mouth bar morphology and hydrodynamics". In: *Journal of Geophysical Research: Oceans* 118 (9), pp. 4169–4183. ISSN: 21699291. DOI: 10.1002/jgrc.20302.

Leonardi, N., Kolker, A. S., and Fagherazzi, S. (2015). "Interplay between river discharge and tides in a delta distributary". In: *Advances in Water Resources* 80, pp. 69–78. ISSN: 03091708. DOI: 10.1016/j.advwatres.2015.03.005.

Lera, S., Nardin, W., Sanford, L., Palinkas, C., and Guercio, R. (2019). "The impact of submersed aquatic vegetation on the development of river mouth bars". In: *Earth Surface Processes and Landforms* 1506.February, pp. 1494–1506. ISSN: 10969837. DOI: 10.1002/esp.4585.

Lesser, G., Roelvink, J., Van Kester, J., and Stelling, G. (Oct. 2004). "Development and validation of a three-dimensional morphological model". In: *Coastal Engineering* 51.8-9, pp. 883–915.

Li, L., Storms, J., and Walstra, D. (2018). "On the upscaling of process-based models in deltaic applications". In: *Geomorphology* 304, pp. 201–213. ISSN: 0169-555X. DOI: https://doi.org/

10.1016/j.geomorph.2017.10.015. URL: https://www.sciencedirect.com/science/article/pii/S0169555X16311850.

Lichter, M., Vafeidis, A. T., Nicholls, R. J., and Kaiser, G. (2011). "Exploring Data-Related Uncertainties in Analyses of Land Area and Population in the "Low-Elevation Coastal Zone" (LECZ)". In: *Journal of Coastal Research* 27.4, pp. 757 –768. DOI: 10.2112/JCOASTRES-D-10-00072.1. URL: https://doi.org/10.2112/JCOASTRES-D-10-00072.1.

Liquete, C., Arnau, P., Canals, M., and Colas, S. (2005). "Mediterranean river systems of Andalusia, southern Spain, and associated deltas: A source to sink approach". In: *Marine Geology* 222-223.1-4, pp. 471–495. ISSN: 00253227. DOI: 10.1016/j.margeo.2005.06.033.

Liste, M., Grifoll, M., and Monbaliu, J. (2014). "River plume dispersion in response to flash flood events. Application to the Catalan shelf". In: *Continental Shelf Research* 87, pp. 96–108. ISSN: 02784343. DOI: 10.1016/j.csr.2014.06.007.

Llasat, M. C. et al. (2010). "High-impact floods and flash floods in Mediterranean countries: The FLASH preliminary database". In: *Advances in Geosciences* 23, pp. 47–55. ISSN: 16807359. DOI: 10.5194/adgeo-23-47-2010.

López-Ruiz, A., Garel, E., and Ferreira, O. (2020). "The Effects of High River Discharges on the Morphodynamics of the Guadiana ebb-tidal delta". In: *Journal of Coastal Research* 95.sp1, pp. 558 –562. DOI: 10.2112/SI95-109.1.

Maillet, G. M., Vella, C., Berné, S., Friend, P. L., Amos, C. L., Fleury, T. J., and Normand, A. (2006). "Morphological changes and sedimentary processes induced by the December 2003 flood event at the present mouth of the Grand Rhône River (southern France)". In: *Marine Geology* 234.1-4, pp. 159–177. ISSN: 00253227. DOI: 10.1016/j.margeo.2006.09.025.

Martín-Vide, J. P., Niñerola, D., Bateman, A., Navarro, A., and Velasco, E. (1999). "Runoff and sediment transport in a torrential ephemeral stream of the Mediterranean coast". In: *Journal of Hydrology* 225.3-4, pp. 118–129. ISSN: 00221694. DOI: 10.1016/S0022-1694(99)00134-1.

Massuanganhe, E. A., Westerberg, L.-O., and Risberg, J. (2018). "Morphodynamics of deltaic wetlands and implications for coastal ecosystems – A case study of Save River Delta, Mozambique". In: *Geomorphology* 322, pp. 107–116. ISSN: 0169-555X. DOI: https://doi.org/10.1016/j.geomorph.2018.08.037. URL: https://www.sciencedirect.com/science/article/pii/S0169555X1730020X.

Melito, L., Postacchini, M., Sheremet, A., Calantoni, J., Zitti, G., Darvini, G., Penna, P., and Brocchini, M. (2020). "Hydrodynamics at a microtidal inlet: Analysis of propagation of the main wave components". In: *Estuarine, Coastal and Shelf Science* 235.November 2019, p. 106603. ISSN: 02727714. DOI: 10.1016/j.ecss.2020.106603. URL: https://doi.org/10.1016/j.ecss.2020.106603.

Nardin, W., Edmonds, D. A., and Fagherazzi, S. (2016). "Influence of vegetation on spatial patterns of sediment deposition in deltaic islands during flood". In: *Advances in Water Resources* 93, pp. 236–248. ISSN: 03091708. DOI: 10.1016/j.advwatres.2016.01.001.

Nardin, W., Mariotti, G., Edmonds, D. A., Guercio, R., and Fagherazzi, S. (2013). "Growth of river mouth bars in sheltered bays in the presence of frontal waves". In: *Journal of Geophysical Research: Earth Surface* 118.2, pp. 872–886. ISSN: 21699003.

Nardin, W. and Fagherazzi, S. (2012). "The effect of wind waves on the development of river mouth bars". In: *Geophysical Research Letters* 39.12, pp. 1–6. ISSN: 00948276.

Nienhuis, J. H., Ashton, A. D., Nardin, W., Fagherazzi, S., and Giosan, L. (2016). "Alongshore sediment bypassing as a control on river mouth morphodynamics". In: *Journal of Geophical Research: Earth Surface* 121, pp. 664–683.

Ortega-Sánchez, M., Losada, M. A. A, and Baquerizo, A. (2008). "A global model of a tidal jet including the effects of friction and bottom slope A global model of a tidal jet including the effects of friction and bottom slope Un modèle global de ruissellement de marée comprenant les effets du frottement et de la pente". In: *Journal of Hydraulic Research2* 46 (April 20), pp. 80–86.

Özsoy, E. and Ünlüata, Ü. (1982). "Ebb-tidal flow characteristics near inlets". In: *Estuarine, Coastal and Shelf Science* 14.3. ISSN: 02727714. DOI: 10.1016/S0302-3524(82)80015-7.

Planning, D. of and Environment State of NSW, A. (2023). *Flood hazard*.

Preoteasa, L., Vespremeanu-Stroe, A., Tătui, F., Zăinescu, F., Timar-Gabor, A., and Cîrdan, I. (2016). "The evolution of an asymmetric deltaic lobe (Sf. Gheorghe, Danube) in association with cyclic development of the river-mouth bar: Long-term pattern and present adaptations to human-induced sediment depletion". In: *Geomorphology* 253, pp. 59–73. ISSN: 0169-555X. DOI: https://doi.org/10.1016/j.geomorph.2015.09.023. URL: https://www.sciencedirect.com/science/article/pii/S0169555X15301598.

Rijn, L. C. van (1984a). "Sediment Transport, Part I: Bed Load Transport". In: *Journal of Hydraulic Engineering* 110.10, pp. 1431–1456. DOI: 10.1061/(ASCE)0733-9429(1984)110:10(1431).

— (1984b). "Sediment Transport, Part II: Suspended Load Transport". In: *Journal of Hydraulic Engineering* 110.11, pp. 1613–1641. DOI: 10.1061/(ASCE)0733-9429(1984)110:11(1613).

— (1993). *Principles of Sediment Transport in Rivers, Estuaries and Coastal Seas*. The Netherlands: Aqua Publications. ISBN: 90-800356-2-9.

Roelvink, D. and Walstra, D.-J. (2004). "Keeping It Simple By Using Complex Models". In: *Advances in Hydro-Science and Engineering* VI.August, pp. 1–11.

Rowland, J. C., Dietrich, W. E., and Stacey, M. T. (2010). "Morphodynamics of subaqueous levee formation: Insights into river mouth morphologies arising from experiments". In: *Journal of Geophysical Research: Earth Surface* 115.4, pp. 1–20. ISSN: 21699011. DOI: 10.1029/2010JF001684.

Rozalis, S., Morin, E., Yair, Y., and Price, C. (2010). "Flash flood prediction using an uncalibrated hydrological model and radar rainfall data in a Mediterranean watershed under changing hydrological conditions". In: *Journal of Hydrology* 394.1-2, pp. 245–255. ISSN: 00221694. DOI: 10.1016/j.jhydrol.2010.03.021.

Ruiz-Reina, A. (2021). *River mouth data from major streams in southern Spain*. Online resource. Version 01. DOI: 10.5281/zenodo.4541878. URL: https://doi.org/10.5281/zenodo.4541878.

Ruiz-Reina, A. and López-Ruiz, A. (2021). "Short-term river mouth bar development during extreme river discharge events: The role of the phase difference between the peak discharge and the tidal level". In: *Coastal Engineering* 170.August, p. 103982. ISSN: 03783839. DOI: 10.1016/j.coastaleng.2021.103982. URL: https://doi.org/10.1016/j.coastaleng.2021.103982.

— (2024). "River mouth hydrodynamics: the role of the outlet geometry and transient tidal and river discharge conditions on the jet structure". In: *Journal of Geophysical Research: Oceans (To be submitted)*. ISSN: 21699291.

Ruiz-Reina, A., Zarzuelo, C., López-Herrera, J. M., and López-Ruiz, A. (2020). "The Marine-fluvial Frontier at River Mouths during Extreme Events: A Hydrodynamic Approach". In: *Journal of Coastal Research* 95.sp1, pp. 1525 –1530. DOI: 10.2112/SI95-294.1.

*Flood hazard mapping in river mouths: the effect of river bar formation and the phase lag between tides and river discharge* (2022).

Savenije, H. (2012). *Salinity and tides in alluvial estuaries (2nd Edition)*, p. 163. ISBN: 9780444521071.

Syvitski, J. P. and Saito, Y. (2007). "Morphodynamics of deltas under the influence of humans". In: *Global and Planetary Change* 57.3-4, pp. 261–282. ISSN: 09218181. DOI: 10.1016/j.gloplacha.2006.12.001.

Wright, L. D. (1977). "Sediment transport and deposition at river mouths : A synthesis Sediment transport and deposition at river mouths : A synthesis". In: *Geological Society of America Bulletin* 88 (6), pp. 857–868. ISSN: 00167606. DOI: 10.1130/0016-7606(1977)88<857.